UNIVERSIDAD TECNICA
FEDERICO SANTA MARIA

Departamento de Obras Civiles

Light-Absorbing Particles and their contribution to the snow melt in the Central Andes

Memoria de Título presentada por

Diego Sebastián Pacheco Ferrada

como requisito parcial para optar al título de

Magister en Ciencies de la Ingeniería Civil

Profesor Guía
Lina Castro Heredia

Profesor Co-Guía
Magin Lapuerta Amigo

November, 2023

UNIVERSIDAD TECNICA
FEDERICO SANTA MARIA

TÍTULO DE LA TESIS:

Light-Absorbing Particles and their contribution to the snowmelt in the Central Andes

AUTOR:

Diego Sebastián Pacheco Ferrada

TRABAJO DE TESIS, presentado como requisito parcial para optar al título de MAGISTER EN CIENCIAS DE LA INGENIERIA CIVIL de la Universidad Técnica Federico Santa María.

	Nombre	Firma
Profesora Guia:	Lina Castro Heredia	.....
Miembro Comisión 1:	Magin Lapuerta Amigo	.....
Miembro Comisión 2:	Mauricio Osses Alvarado	.....
Miembro Comisión 3:	Raul Flores Audibert	.....
Miembro Comisión 4:	Sofía Gonzalez Correa	.....
Miembro Comisión 5:	Tomas Bolaño Ortiz	.....

Valparaíso, Chile, 30 de Octubre de 2023

Light-Absobing Particles and their contribution to the snowmelt in the Central Andes

Diego Pacheco Ferrada[1], Lina Castro Heredia[1], Magín Lapuerta Amigo[2]

[1] Universidad Técnica Federico Santa María
[2] Universidad Castilla-La Mancha

Abstract

This research aims to comprehensively assess the effects of Light Absorbing Particles (LAPs) on the optical properties of snow surfaces and the impacts on snow hydrology, focusing on the Central Andes. Initially, an experimental study was conducted in Sierra Nevada, Spain, to analyze the optical effects of different LAPs, like sand, ash, haze, and soot on snow covers. Findings revealed a reduction in snow albedo across the entire spectrum, with soot agglomerates showing the highest potential to reduce snow albedo. Then, investigations centered on the Central Andes near the El Yeso dam, where snow was artificially contaminated using preconditioned soil samples to simulate mineral dust (MD) deposition. Contaminated surface albedo shows reductions significant in the UV and visible range, and simulated values, from the OptiPar radiative transfer model, mostly agree with field measurements regarding some discrepancies, attributed primarily to variation in MD mineralogical composition. Finally, the Utha Energy Balance snow model was coupled with the OptiPar radiative transfer model, considering particles previously characterized, to simulate snowpack accumulation and melting from 2014-2019 at Portillo weather station located in the Juncal River Basin, Chile. Black carbon (BC) and MD were found to accelerate the snowpack depletion, inducing an early meltout of up to 3 days. BC had the most significant impact on the snowpack, due to its higher absorption capacity. This extensive research shows that LAPs play a significant role in snow albedo variations and consequently in the snowpack duration, impacts that are crucial for hydrology in regions like the Central Andes.

Palabras claves: Black Carbon, Mineral Dust, Albedo.

"Te abrazo donde estés
Y yo no sé, no sé como llegar
Y solo se, tan solo se cantar
Y agradecer que pude disfrutar
de tus mimos..."

Acknowledgements

First and foremost, I'd like to thank my partner, friend, and lover, Vanessa. Part of this achievement is yours. Thanks for your love and companionship, and daily support; without you, this couldn't have become real. With Nuez, you both have accompanied me every time stay the night, in every meltdown, and in every laugh. Thank you.

To Luz, my mother, Pedro, my father, Nati, my sister, Nano y Adriana, my grandparents, and to all my birth family. Thanks for your unconditional support and kindness. You all are my example, the voice that guides me in times of doubt.

To my friends, the ones that I've made during this process, and the ones that have stood by my side since years ago.

Lastly, I'd like to thank my advisors, Lina Castro and Magin Lapuerta, for continuously giving me the chance and confidence to pursue my ideas and curiosity throughout this graduate degree. You've given me opportunities that I haven't imagined a couple of years ago.

This work was carried out within the framework of the ANID projects: **Proyecto ANID Anillo ACONCAGUA ACT210021** *"Interactions between environmental compartments and their impact on the Andean ecohydrosphere under conditions of climate change (ACONCAGUA)"*; and **Fondecyt Iniciación 11220482** *"Changes in snowmelt as a decisive issue for available water resources in Andean basins in central Chile"*

Contents

List of Figures

List of Tables

Introduction

Light-absorbing particles, known as LAPs, are recognized as contributors to climate change (Myhre et al., 2013). They can be originated from both, natural and anthropogenic sources, and be deposited onto the snow surface altering the snowpack energy budget (Skiles et al., 2018). These include LAP such as Black Carbon (BC, from incomplete combustion) (Cereceda-Balic et al., 2018; Zhong et al., 2019), Brown Carbon (BrC, from biomass combustion) (Beres et al., 2020), Volcanic Ash (Constantin et al., 2020), and Mineral Dust (MD, from deserts, disturbed soil, and industrial activities) (Dumont et al., 2020; Skiles & Painter, 2017), among others. When LAPs deposit onto the snow, they darken the surface and decrease the surface albedo, inducing a radiative forcing input and leading to an earlier melt-out(Painter et al., 2010). These effects can have significant impacts on the water storage of the basin, particularly if the catchment depends on seasonal snow accumulation for water supply. This is the case of the Central Andes, a region that provides important ecosystem services for humans, such as water supply and economic activities development (Webb et al., 2020), which have been under climatic stress during the last decades due to climate change (Garreaud et al., 2017). Precipitation deficits over 25% and temperature increasing trends (Garreaud et al., 2017; Garreaud et al., 2020), have resulted in a decreasing snow cover extent, diminish of snow water equivalent (Malmros et al., 2018), and an accelerated ablation of glacier mass.(Dussaillant et al., 2019). The loss of the Andean cryosphere could be accentuated towards the end of the century, due to the expected temperature increases in this area as a result of climate change (Migliavacca et al., 2015). If the present and future effects of climate change put in risk the Andean cryosphere, a critical understanding of the factors that drive these changes is crucial, and of course, atmospheric pollution and how can affect the snowmelt process in the Andes.

Albedo is known as the physical property that indicates how much energy is reflected by a surface, and it is usually analyzed in a spectral (*Spectral Albedo*) or as an average in a specific wavelength range in the solar spectrum (*Broadband Albedo*) (Cogley et al., 2011). Snow is a highly reflective medium, and probably a surface with one of the highest natural albedo on the earth. At UV and visible (VIS) wavelength range albedo reaches up to values close to the unit, but at longer wavelengths, it rapidly drops and becomes *"dark"*. This surface reflection capacity of the snowpack varies across the wavelength range and is highly dependent on the snow surface properties, such as grain size (Dang et al., 2016), liquid water content (Dozier et al., 2004) or snow depth (Chen et al., 2014; Zhou et al., 2003). LAPs deposition reduces the snow reflection capacity, due to their relatively high absorbance in the visible wavelength range compared to ice crystals (Warren et al., 1980), and therefore less solar irradiance is reflected. This also prone a positive feedback on snow metamorphism, which means that not only LAPs radiative perturbation is amplified in snowpacks with larger ice crystals, but it also affects further, by enhancing grain coarsening (Hadley et al., 2012; Skiles et al., 2019). However, depending on the LAPs composition and morphology, the effect over snow surface albedo varies.

Black Carbon (BC), has gathered attention in the scientific community due to its radiative effect and abundance. Black Carbon is a product of incomplete combustion of carbonaceous fuels, such as fossil fuels, biofuels, and biomass, and it can be emitted from natural (wildfires and volcanic eruptions) or anthropogenic sources (industries, vehicles, residential heating emissions) (Cereceda-Balic et al., 2019). According to the IPCC, BC aerosols are one of the most contributing particles to climate change due to their high absorbance capacity (Myhre et al., 2013). The impact of BC onto snow surface reflection has been observed around the world. Special attention has focused on the Himalayas and the Central Asia Region, due to the importance of the mountains for water supply and their proximity to urban centers (Ginot et al., 2014; Jacobi et al., 2015; Li et al., 2020; Schmale et al., 2017; Zhong et al., 2019). But also in the eastern Sierra Nevada of California (USA) (Sterle et al., 2013), the Alps (Dumont et al., 2017), the Arctic (Clarke et al., 1985), and the Antarctic Peninsula (Cereceda-Balic et al., 2020; Cordero, Sepúlveda, Feron, Damiani, et al., 2022). On the other hand, mineral dust (MD) is one of the primary constituents of atmospheric aerosols (Li et al., 2020) and mainly originated in naked or disturbed soils and deserts (Skiles & Painter, 2017). In the atmosphere, MD particles can travel long paths, during which aerosols can vary their size or composition due to collisions between particles and by mixing with other compounds, and therefore present high variability in their absorption characteristics (González-Correa, Lapuerta, et al., 2022). After Saharan outbreaks, MD deposition onto snow has been observed from the southern Iberian Peninsula (González-Correa, Lapuerta, et al., 2022), the Alps (Dumont et al., 2020), to the Russian Caucasus Mountains (Dumont et al., 2020). Also, human activities like urban expansion in the Rocky Mountains at the Colorado River basin have contributed to a soil disturbance, leading to an average snow season shortening of three weeks because of MD deposition onto the snowpack, compared to the preindustrial era (Painter et al., 2010).

In the case of the Andes, the study of LAPs and their consequences on snowpack melting is still uncertain. However, since this region has been under climatic stress for the last decade, more surveys and studies have been developed in other to understand their effects (Cereceda-Balic et al., 2022; Constantin et al., 2020; Rowe et al., 2019). Extensive surveys across the Chilean Andes have concluded that BC concentration onto snow decreases southward from Putre (18^{o}S) to La Serena (30^{o}S) (Rowe et al., 2019), Around the Central region of Chile, where more populated urban centers are located, the BC concentration onto snow increases, and then again, it decreases southward until the Lakes District (42^{o}S) and Patagonia. Meanwhile, a considerable effect of MD particles has been found, particularly around metropolitan areas and industrial operation sites, and the importance of MD in light absorption has been found to decrease from the Dry Andes (18^{o}S) until the Lakes District (Cordero, Sepúlveda, Feron, Wang, et al., 2022; Rowe et al., 2019). Highly polluted areas in the Central Andes have been mainly attributed to anthropogenic (such as mining operations, vehicular traffic, and urban emissions), over natural sources. In the Central Andes, mining operations have gathered attention on the effects that they can induce over nearby glaciers. Cereceda-Balic et al. (2022) compared Olivares Alpha Glacier (OAG) with Bello Glacier (BG), geomorphically similar glaciers, but BG is located farther from any mining exploration. BC and MD mass concentration onto snow at OAG was 61 and 67 times more than at BG, and trace elements analysis also showed higher content of As and Pb, well known as Cu mining operation and anthropogenic tracers. They conclude that 82% of the retreat OAG retreat between 2004 and 2014, has been caused by the LAPs accumulated at the glacier surface. Simultaneously, Barandun et al. (2022) measured traces of pyrite, typically found in hydrothermal alteration zones, and jarosite, over the Olivares catchment glaciers, minerals that can be found in mine tailings. Similar studies have been conducted in

different areas around the Central Andes. In the Juncal River Basin (32.9ºS), high concentrations of BC onto snow have been reported, and mainly attributed to vehicular emissions (Cereceda-Balic et al., 2019; Cereceda-Balic et al., 2018), where soot agglomerates are the main component (Lapuerta et al., 2009). Additionally, trace element (Cereceda-Balic et al., 2012) and BC atmospheric concentrations (Gramsch et al., 2020) have been measured in the mountains near Santiago, suggesting that urban pollution could eventually travel to the high mountains and deposit onto snow surface.

Because of these findings is possible to hypothesize that BC and MD deposition over the Andes, particularly in the Central Andes next to the major cities, is affecting the snow albedo and consequently inducing an acceleration in melting rates. Currently, only point samples have been collected to measure the deposited concentration of LAPs onto snow, which limits the possibility of understanding their impact on a timescale basis. Furthermore, specific characteristics of the particles have not been taken into account, which is particularly important in the case of MD which varies its optical properties depending on the mineralogical composition and, therefore, global characteristics are not reliable in a regional scale (Skiles et al., 2018).

To address the effects of onto snow surface a wide scope of research approach is necessary. Particularly, the main objective of this study is to assess the optical effect of Light Absorbing Particles concentration onto snow surface and their consequences on snow melting over the Central Andes. More specifically this thesis reaches for two objectives. The first aims to analyze the influence of LAPs over the snow surface albedo using an experimental approach and contrasting it to radiative transfer model results. The second aims to model the snow melt as a result of albedo variations due to LAPs deposition, by coupling a Snow Energy Balance physical-based model and a Radiative Transfer model.

For a better understanding, a brief explanation of the document is given. Chapters 1 and 2, are dedicated to the first goal and delve into understanding the optical effects of LAPs using an experimental approach. Finally, Chapter 3 is entirely dedicated to the second goal, and it explains the results obtained from a snow model (Utha Energy Balance) and a radiative transfer model (OptiPar) coupled to simulate the effects of LAPs on the snowpack.

Chapter 1 addresses the reductions in snow albedo related to different LAPs onto snow. For this, an experimental approach was designed to artifitially contaminate using Haze, soot, sand, and ash particles, and measure the albedo decrease using a hyperspectral spectroradiometric system covering a wavelength from 300 to 2500 nm. Each one of these LAPs was separately characterized to determine their optical properties, and incorporate them into OptiPar's code to simulate the albedo decay. This chapter is a version of the journal article published in October 2022 in the peer-reviewed journal Atmosphere as "González-Correa, S., Lapuerta, M., Ballesteros, R., **Pacheco-Ferrada, D.**, Castro, L., & Cereceda-Balic, F. (2022). Impacts of Soot, Ash, Sand, and Haze on Snow Albedo in Sierra. *Atmosphere* **2022**, 13, 1–15. https://doi.org/https:// doi.org/10.3390/atmos13111903".

Chapter 2 addresses the reductions in snow albedo related to Mineral Dust concentrations onto snow. For this, Andean soil samples carefully collected in the Central Andes were selected and preconditioned to artificially simulate snow contamination by Mineral Dust. Samples were characterized for the determination of optical properties of the specific Mineral Dust, and incorporated into OptiPar's code to simulate the albedo decay. This chapter is been prepared for submission to a peer-reviewed journal, as " **Pacheco-Ferrada, D**., González-Correa, S., Lapuerta, M., Castro,

L., Ruggeri M-F., & Cereceda-Balic, F. Optical effect of Andean Mineral Dust onto snow surface spectral albedo.

Chapter 3 addresses the impacts of LAPs (BC and MD) on the snowpack on a timescale basis. reductions snow albedo related to Mineral Dust concentrations onto snow. With this in mind, the physical-based snow model named Utha Energy Balance was coupled with OptiPar's radiative transfer model have been coupled through an empirical approach to simulate the accumulation and depletion of snowpack, and quantify the effect of LAPs deposition on snow albedo and melting on a time basis scale (2015-2019) in the Juncal River Basin, Chile This chapter is an extended version of a poster presentation submitted for the annual American Geoscience Union (AGU) Fall Meeting 2003, as " **Pacheco-Ferrada, D**., Pettersen D., Castro, L., & Cereceda-Balic, F., Snow energy balance and radiative transfer model coupling for quantifying BC and dust impact on Juncal River Basin hydrology".

A final segment has been incorporated in order to summarize the document and explore unresolved issues and potential advancements in the field. It is crucial to comprehend not only the present state of LAPs on the andean cryosphere, but also anticipate future trends and address climate change mitigation opportunities.

Chapter 1

Impacts of Soot, Ash, Sand, and Haze on Snow Albedo in Sierra Nevada, Spain

1.1 Abstract

Snow covers are greatly affected by particles deposited on their surface. In this work, an experimental campaign was carried out in the Sierra Nevada (Granada, Spain). The optical effect of different contaminating particles on the snow covers was measured using a field spectroradiometric system composed of three upwelling spectroradiometers and three downwelling ones. Sand collected from a Mediterranean beach (Spain), ash collected from the La Palma volcano eruption, haze collected from an event that occurred in Spain, and soot collected from a diesel vehicle were employed for contaminating the snow. Soot, ash, and sand were analyzed with X-ray diffraction to obtain their mineralogical composition or their structural characteristics, whereas haze's mineralogical composition was obtained from the literature. From this information, the refractive index of each material was weigh-averaged, considering the refractive indices of their components. After measurements, snow samples were filtered and weighted to evaluate the particle concentrations in the snow. Previous contamination with soot was observed due to the existence of a nearby road. Snow albedo was calculated with the OptiPar model. The experimental and modeled results show that contaminating with sand decreases the snow albedo in the visible range whereas it increases the albedo in the infrared range. However, the rest of the materials lead to a decrease in the albedo in the whole spectrum,

1.2 Introduction

Particles can be generated from combustion processes such as those vehicles, aircrafts, and boilers or from forest burning (Bond et al., 2013). In these processes, the most common particles generated is soot. In addition, due to strong haze events and gusts of wind, sand and haze particles from soils can be moved and suspended in the atmosphere (Kok et al., 2012). Furthermore, volcanoes constitute a natural source of ash which can also remain suspended in the atmosphere (Smithsonian, 2022). The residence time of particles in the atmosphere depends on their size. Very small and very large particles have low residence times since they are controlled by sedimentation processes and diffusive losses, respectively (Jaenicke, 1980; Mohnen et al., 1983). Some strong haze events took place last spring (2022) in Spain, where haze particles were blown from the Saharan dessert, as can be seen from satellite images of Aerosol Optical Depth and haze transportation in Figure 1-1a (WMO Barcelona Dust Regional Center, 2022), as well as ash cloud transportation from La Palma eruption which started on September 2021 Figure 1-1b (Copernicus Atmosphere Monitoring Service, 2022).

These particles from anthropogenic (soot) and natural (ash, haze, and sand) sources have an environmental effect on global heating (Rémy et al., 2019), as well as on polluting surfaces as far as their suspension residence time is large enough (Moosmüller et al., 2009; Valsaraj et al., 2018). An example of a house facade contaminated through a spring haze event in the area of Almería, Spain, is shown in Figure 1-2a, where the first floor remains colored, and the ground floor has already been cleaned up. However, the surfaces that are mostly affected by particles deposited on their surface are snow covers (Flanner et al., 2021), due to their high reflectance, and are the ones that contribute most to cryological climate change (Kokhanovsky et al., 2004). Additionally, an example of the soiling of the snow surface with haze in the south of the Iberian Peninsula (Sierra Nevada, Granada) is shown in Figure 1-2b.

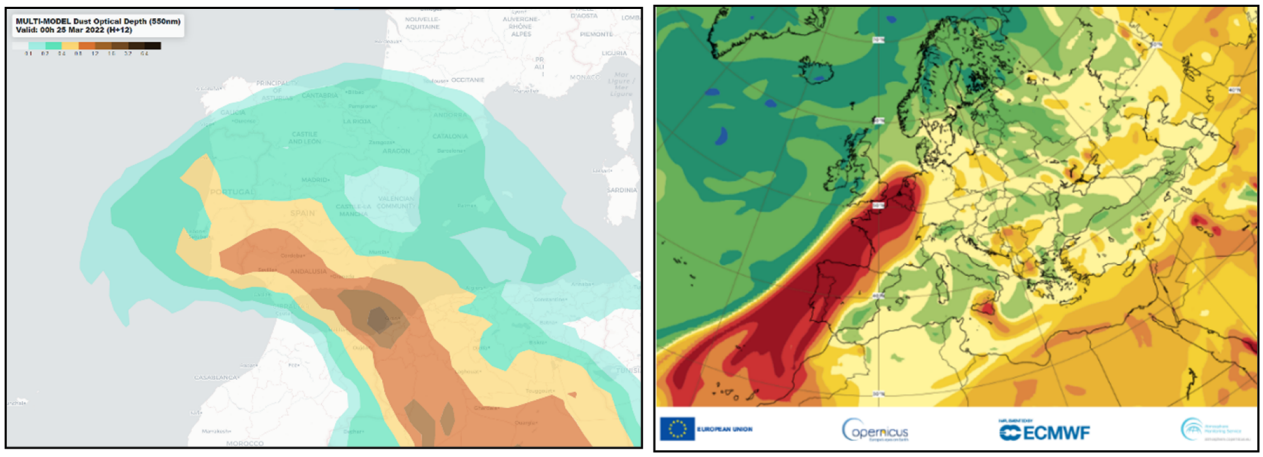

Figure 1-1: (a) Aerosol Optical Depth of 25 March 2022 (WMO Barcelona Dust Regional Center, 2022) by MULTI-MODEL (Basart et al., 2019) illustrating the haze episode over the Iberian Peninsula. Dust image was provided by the WMO Barcelona Dust Regional Center and the partners of the Sand and Dust Storm Warning Advisory and Assessment System (SDS-WAS) for Northern Africa, the Middle East and Europe. (b) CAMS (Rémy et al., 2019) forecast of the total column of sulphur dioxide initiated at 00 UTC on 19 October (Copernicus Atmosphere Monitoring Service, 2022), indicative of ash flowing from La Palma eruption.

Figure 1-2: Haze deposited in a house façade (partially cleaned), after haze events in Almería, Spain (a) and effects of haze event in Sierra Nevada, Granada, on 8 April 2022 (b) (photographs from authors).

Considering the environmental vulnerability of this region, experimental measurements have been carried out in the Sierra Nevada, employing different particles (soot, ash, haze, and sand) for snow artificial contamination to evaluate the effect of the surface albedo modifications. The reasons why these materials are selected are the following: soot is the main component of particles emitted from vehicles which often circulate close to ski resorts. Ash can be transported from eruptions located thousands of kilometers away. Sand can be lifted from bare soils and moved through strong winds or storms. Saharian haze is a fine mineral dust that often blows toward south-Europe regions. All these materials can be deposited in Sierra Nevada snow areas affecting the radiative balance and thus the hydrological cycles.

Some experimental campaigns and simulations about the effect of aerosols deposited onto snow surfaces all over the world have been reported in the literature. Cereceda-Balic et al. (2018) measured the reduction in broadband snow albedo due to local emissions of soot from high vehicular traffic in the surroundings of a road in the Chilean Andes. Further studies about the effect of soot deposition from vehicles have shown that this reduction is different depending on the spectral range, such as those by González-Correa, Gómez-Doménech, et al. (2022) in Sierra Nevada, and Lapuerta et al. (2022) in Cotos Port, Madrid (both in Spain). Skiles and Painter (2017) measured daily black carbon and dust, and snow optical parameters in the Rocky Mountains, Colorado, where reductions of snow albedo down to 0.3 were observed as a consequence of dust deposition. They also observed different reductions depending on the spectral range. Niu et al. (2017) observed reductions in the broadband albedo of aged snow in Mount Yulong from 2% to 10% derived from the deposition of black/organic carbon and dust. Dang et al. (2015) computed the reduction of snow spectral albedo by black carbon and mineral dust using a radiative transfer model. Simulations with Snow, Ice, and Aerosol Radiative (SNICAR) for different Saharan dust sizes and with ash from the Eyjafjallajökull volcano were presented by Flanner et al. (2021). Painter, Bryant, et al. (2012) used remote sensing, and processed results with the MODIS Dust Radiative Forcing in Snow (MODDRFS) model, retrieving surface radiative forcing by dust and carbonaceous particles in snow and observing snow spectral albedo reductions mainly in the visible range in Upper Colorado River Basin and Hindu Kush-Himalaya. Constantin et al. (2020) measured and simulated with SNICAR a large impact on snow albedo in the Argentinian Andes as a consequence of ash deposition from volcanic eruptions. In most of these studies, the effects on albedo depended not only on the spectral range, but also on the composition, size, shape, and crystalline structure of the deposited particles (Formenti et al., 2011).

Different materials lead to different spectral effects on snow albedo and thus to different radiative forcings. However, they have not been compared under similar conditions. The main novelty of this work lies in the comparison of the effect of various contaminating materials (to which the Iberian Peninsula is frequently exposed) on the snow albedo, for which in-field measurements were made at the same site. The compositional characterization of these materials, together with the modeling of these effects has been revealed as helpful to interpret such effects

1.3 Methods

Experimental testing was carried out in different stages, as shown in Figure 1-3. First, the materials for snow surface contamination were selected (light brown box in Figure 1-3). These materials were obtained from different sources: (1) soot was collected from experimental tests from an automotive diesel engine in the University of Castilla-La Mancha (UCLM) installations (Lapuerta et al., 2012); (2) ash was collected on 26 September 2021 by members of Geomorphology, Territory, and Landscape in Volcanic Regions (GEOVOL) research group at UCLM from Tenecuita centre, 14 km away from the eruption of the volcano Cumbre Vieja in La Palma island, in Canary Islands, Spain, occurred on 19 September 2021 (Smithsonian, 2022); (3) sand was collected from a Mediterranean beach and d) haze particles arising from haze events held in Spain in March 2022 was collected on 15 March 2022 from depositions in the area of UCLM campus in Ciudad Real (La Tribuna de Ciudad Real, 2022).

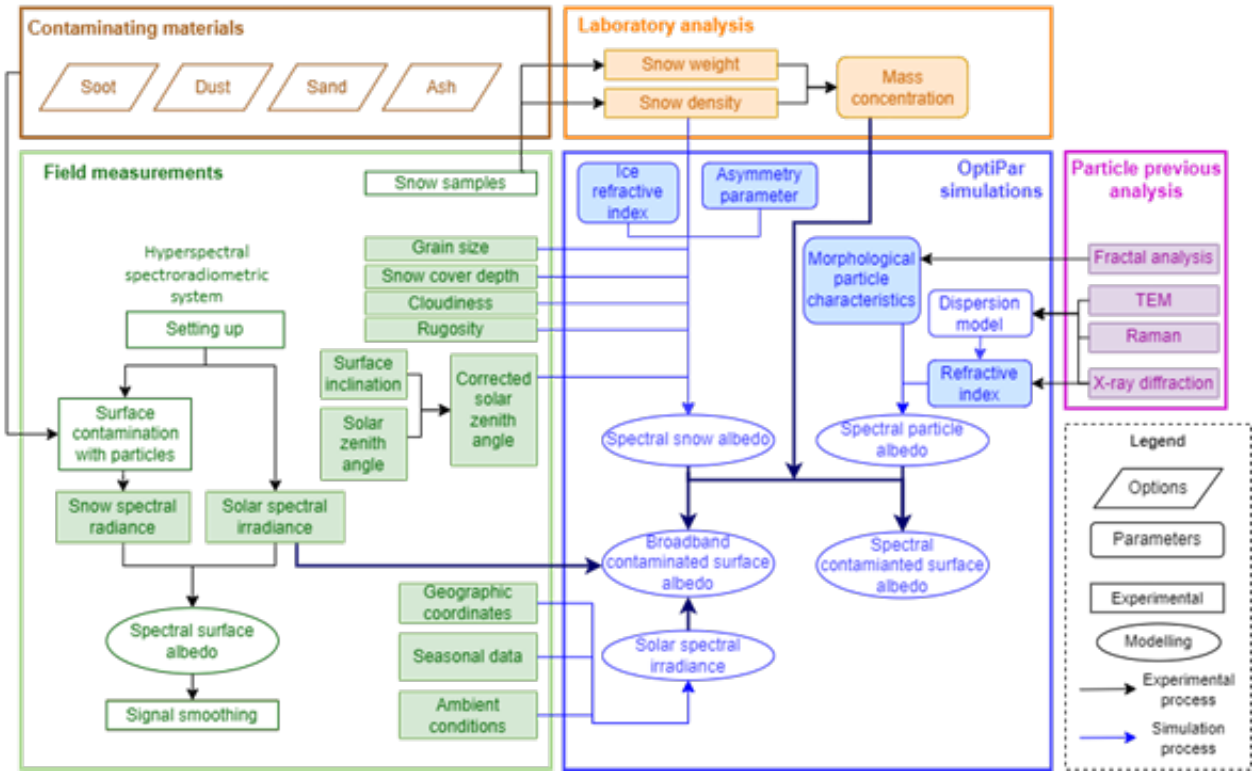

Figure 1-3: Scheme of the procedure and methodology followed connecting field measurements (green square) with simulations (blue), with previous laboratory analysis of particles (purple), and later snow analysis of snow (orange).

Materials collected were analyzed (purple box in Figure 1-3). For soot, Transmission Electron Microscopy (TEM) analysis was made to obtain their morphology and fractal parameters (Lapuerta et al., 2006; Pawlyta et al., 2016; Saffaripour et al., 2017). For the rest of the materials, X-ray diffraction was performed to characterize their mineralogical components (Gupta et al., 2009). Afterward, field measurements were carried out (green box in Figure 1-3).

A field-hyperspectral spectroradiometer system designed by Antares Instrumentation S.L. employing Avantes instruments was used to perform spectral radiance of natural and contaminated snow surface and solar spectral irradiance measurements. The equipment is composed of two groups of three spectroradiometers for each wavelength range: UV-VIS (300–1100 nm), NIR (900–1700 nm), and IR (1700–2500 nm). These spectroradiometers are connected to two optical fibers supported by an extended tripod with two cosine-corrector optical detectors placed in an upwelling and downwelling direction for irradiance and radiance measurements, respectively. More details of this equipment and setting up can be found in Lapuerta et al. (2022) and González-Correa, Gómez-Doménech, et al. (2022).

The experimental campaign took place on two different dates: 16 December 2021 and 8 April 2022, in the proximities of Sierra Nevada ski resort, Granada, Spain. Measurements were carried out at two different sites. The first one was carried out close to a ski slope (37.09◦ N, 3.39◦ W, 2500 m.a.s.l.) and the second one on a helicopter landing pad (37.05◦ N, 3.23◦ W, 2500 m.a.s.l.) (see

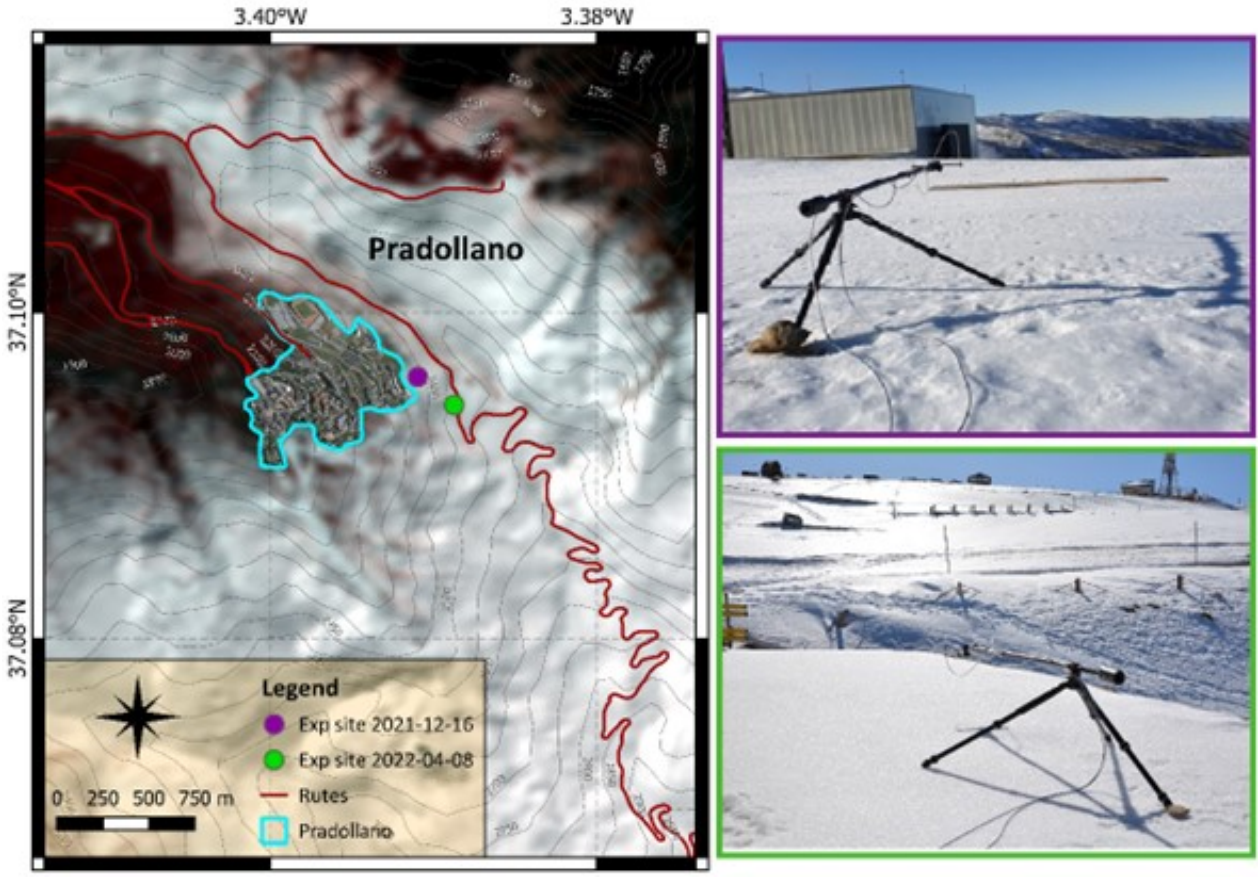

Figure 1-4: Location of the experimental sites (a) and views from the sites (b,c) for 16 December 2021 (b) and 8 April 2022 (c).

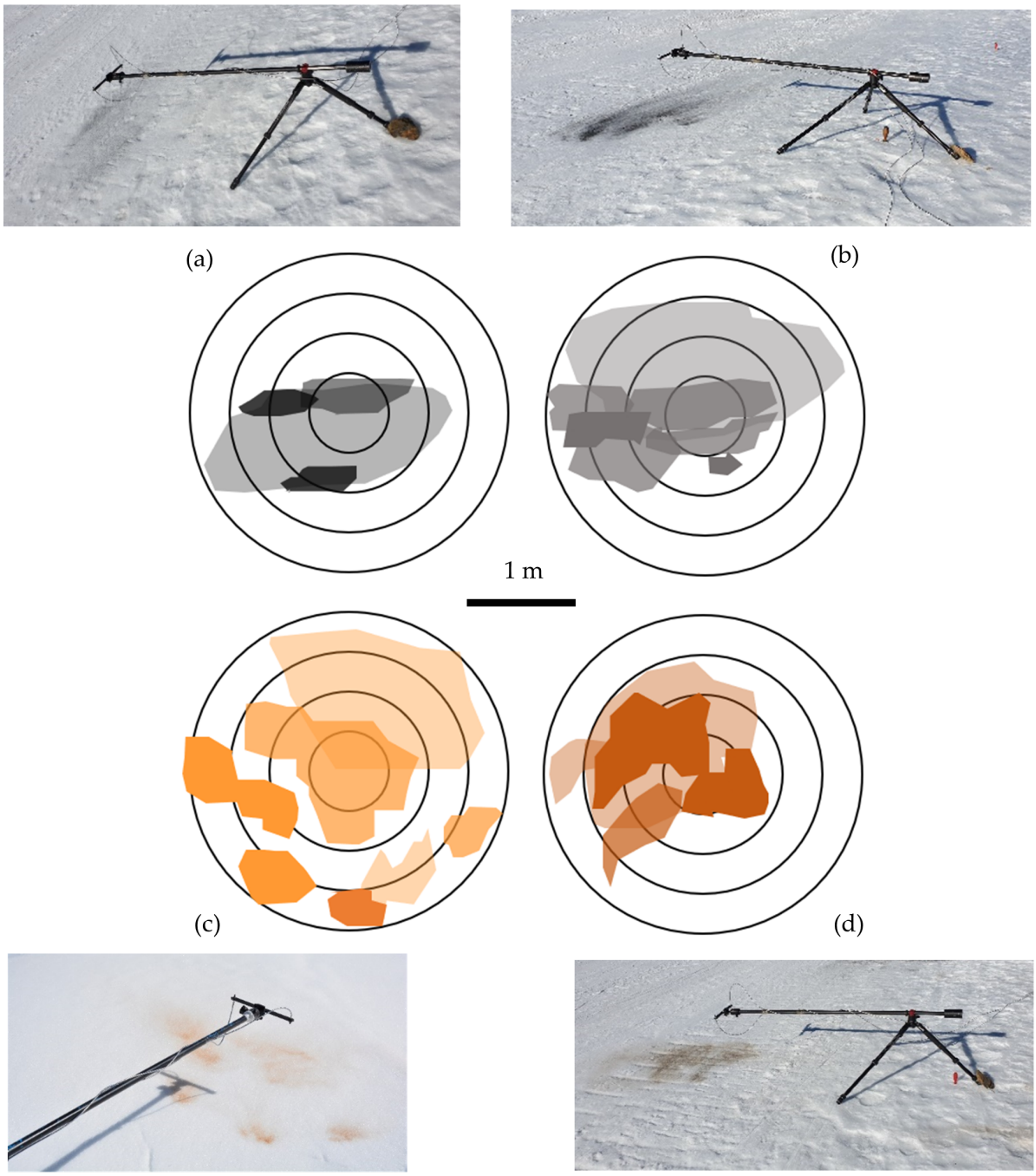

Figure 1-5: Weighing method and example for (a) soot, (b) ash, (c) haze, and (d) sand. Concentric circles represent radially weighted areas. Three levels of darkness are also shown for each material, considering different concentrations.

Figure 1-4)

Measurements were made on "clean" and artificially contaminated snow. "Clean" contamination refers to surfaces exposed to continuous contamination with soot particles from a nearby road from the last snowfall that occurred on 9 December 2021 and on 6 April 2022 (Meteoblue, 2022) and also with haze from haze events that happened on 25 March 2022 (WMO Barcelona Dust Regional Center, 2022) and artificially contaminated refers to the manual deposition with a sieve of collected particles on the analyzed area.

Although homogeneity was searched during artificial contamination, wind gusts, the size distribution of the materials, and other additional external factors generated non-homogeneous surface contamination. This issue has been addressed in a few experiments on artificially contaminated snow (Conway et al., 1996), arising new concerns on the representativity of the deposition process onto the natural snowpack, such as perturbance of the snowpack physical properties, scavenging of small particles into deeper layers due to an airflow input for deposition, or melting acceleration caused by a temperature increase when a chamber for deposition is used, among others (Beres et al., 2018; Beres et al., 2020). For this reason, the mass concentration obtained from laboratory analysis was corrected and weighted considering the contamination observed in the photographs (see Figure 1-5). The vision area from the downwelling cosine receptor is a circle of radius 1.5 m, which comprises a vision factor of 95% considering that the upwelling detector height was 35 cm with respect to the snow surface. In Figure 1-5, contaminated areas with three different darkness levels in the analyzed zone are shown, to exemplify the different concentrations of materials artificially deposited on snow surfaces. Each concentric circle corresponds to a visual area, and the average mass concentration is calculated by radially weighting the darkened areas.

Field measurements of snow grain size, cover depth, cloudiness, rugosity, surface inclination, and solar zenith angle were taken (see Table 1.1). Photographs of the snow size were made on a calibrated card for a size distribution characterization with ImageJ (National Institutes of Health, Bethesda, MD, USA.) (Schneider et al., 2012) (see Figure 1-6). No cloudiness was appreciated on the dates of the campaign (as observed in Figure 1-4) and rugosity of the snow surfaces and humidity were considered neglectable. The solar zenith angle was corrected using the surface inclination. In addition,

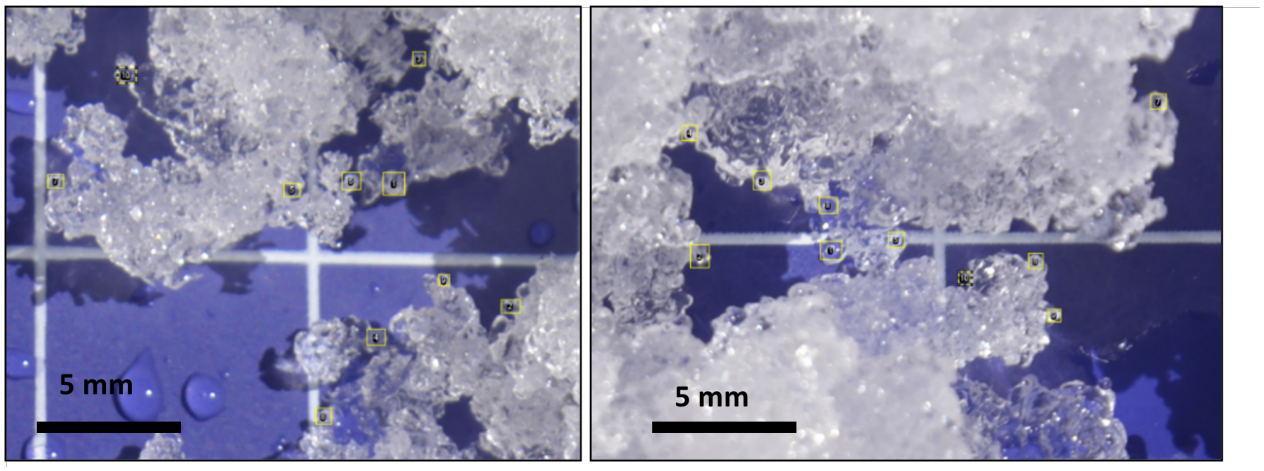

Figure 1-6: Example of snow particle size analysis for the 16 December 2021 (a) and the 8 April 2022 (b). Ice particles are surrounded by yellow rectangles since particles are not completely spherical. Particle diameters were calculated as the mean height and width of the rectangles.

Table 1.1: Parameters for snow contamination characterization (previously contaminated refers to "clean" snow)

Date	Snow surface previously contaminated with	Snow surface artificially contaminated with	Corrected zenith Angle^o	Concentration $mg \cdot kg^{-1}$	Snow density $kg \cdot m^{-3}$	Snow grain radius μm	Snow depth radius cm
16 th Dec 2021	Soot	-	70.3	0.9	250	309.8 ± 53.4	Semi-infinite
	-	Soot		0.8			
	Soot	-	61.0	0.5			
	-	Ash		90			
	Soot	-	65.0	0.53			
	-	Sand		100			
8 th Apr 2022	Soot + Haze	-	48.6	0.2 Soot + 25 Haze	404.78	270.3 ± 40.6	11.46
	-	Haze		25			

snow samples are used in laboratory analysis for snow density and mass concentration ($mg \cdot kg^{-1}$) determination. The procedure to obtain the particle mass concentration is explained in González-Correa, Gómez-Doménech, et al. (2022). With all these experimental parameters, simulations were made with OptiPar (Lapuerta et al., 2022) (blue box in Figure 1-3), which contains a radiative transfer model for the determination of optical properties of some materials and ice particles, as well as snow surfaces contaminated with deposited light-absorbing particles (LAPs). Among the various options available in OptiPar, the following methods and parameters were selected. Snow albedo of a finite (considering the underground albedo of the soil) or semi-infinite cover was determined through the model from Wiscombe et al. (1980) and with the refractive index of Warren et al. (2008). For snow albedo characterization, snow density, depth, grain, and the corrected zenith angle were taken for the simulations. Particles of the different polluting materials were simulated with the Mie theory or the Rayleigh-Debye-Gans approximation (using the correction for multiple scattering proposed by Mountain et al. (1988)) depending on the size of the deposited particles were used. After the materials and the snow were optically characterized separately, the snow surface contamination was simulated using both the concentration of previously deposited soot (and eventually haze) and the artificial contamination with soot, ash, sand, and haze concentrations.

1.4 Particles Characteristics

Snow and materials characteristics were summarized in Tables 1.1 and 1.2, respectively. From the observed particle size distributions, the following average particle radius was obtained for each material: 300 nm for ash, 10 μm for sand, 1.5 μm for haze deposited in Sierra Nevada, and 400 nm for haze deposited in Ciudad Real.

Soot fractal parameters were considered to simulate the morphology of soot particles. In both cases, "clean" and artificial contamination for all the simulations, agglomerates composed of 80 primary particles of 12.5 primary particle radius (nm) each and with a fractal dimension of 1.85 was used. These were the reference conditions in a previous study with a diesel engine (Lapuerta et al., 2009). From these parameters, the average radius of gyration was obtained for soot agglomerates, using the power law relationship (Lapuerta et al., 2006), resulting in 97 nm. Densities of contam-

Table 1.2: Materials average grain radius and densities (previously deposited refers to "clean" snow).

Material		Average grain radius (nm)	Density ($kg \cdot m^{-3}$)
	Soot	97	1850
	Ash	450	2600
	Sand	10000	1500
Haze	Previously deposited	1500	2500
	Artificially deposited	400	

inating materials were taken from the literature. For haze, a density value of 2500 $kg \cdot m^{-3}$ was used as proposed by Dang et al. (2015). For sand, a value of 1500 $kg \cdot m^{-3}$ was used, which is within the range proposed by Ajalloeian et al. (1996). For ash, a value of 2600 $kg \cdot m^{-3}$ proposed by Flanner et al. (2021), was used. For soot, 1850 $kg \cdot m^{-3}$ inherent density was used based on the model proposed by Belenkov (2001). For the determination of the particle mass for each material, a spherical shape was assumed except in the case of soot agglomerates, for which it was obtained as the product of a number of primary particles and the mass of the mean primary particle.

Sokolik et al. (1999) showed that the mineral composition of the materials must be incorporated into the radiative models to estimate their optical properties. For this reason, an effective medium model (Belenkov, 2001) was employed for the determination of the dielectric constant ($\epsilon_{particle}$). From the dielectric constant of all the minerals of the material (ϵ_i), their volumetric fraction (fv_i), and the dielectric constant of the medium (ϵ_{medium}), the material dielectric constant was determined as follows:

$$\frac{\epsilon_{particle} - \epsilon_{medium}}{\epsilon_{particle} + 2\epsilon_{medium}} = \sum_{i=1}^{N} fv_i \frac{\epsilon_i - \epsilon_{medium}}{\epsilon_i + 2\epsilon_{medium}} \tag{1.1}$$

This general equation is particularized assuming the hypothesis that the medium is a vacuum as proposed by Lorentz-Lorenz (Sihvola, 2000), and, therefore, the dielectric constant of the medium is unity.

$$\frac{\epsilon_{particle} - 1}{\epsilon_{particle} + 2} = \sum_{i=1}^{N} fv_i \frac{\epsilon_i - 1}{\epsilon_i + 2} \tag{1.2}$$

Therefore, ash, sand, and haze were analyzed with X-ray diffraction to obtain their mineralogical composition by volume (see Figure 1-7). With this information, the dielectric constants of the particles were determined and, hence, their refractive index for optical properties calculations was obtained (see Figure 1-8). In the case of sand, 7.4% content of acetoguanamine was detected with X-Ray diffraction. However, this mineral was not used for sand refractive index determination because no absorption coefficient was found for this material. Dielectric constants of each mineral were obtained from a database (Polyanskiy, 2022) and from the references shown in Table 1.3. Soot refractive index was characterized by the correlation proposed by Chang et al. (1990) based on experimental data obtained at 300 K.

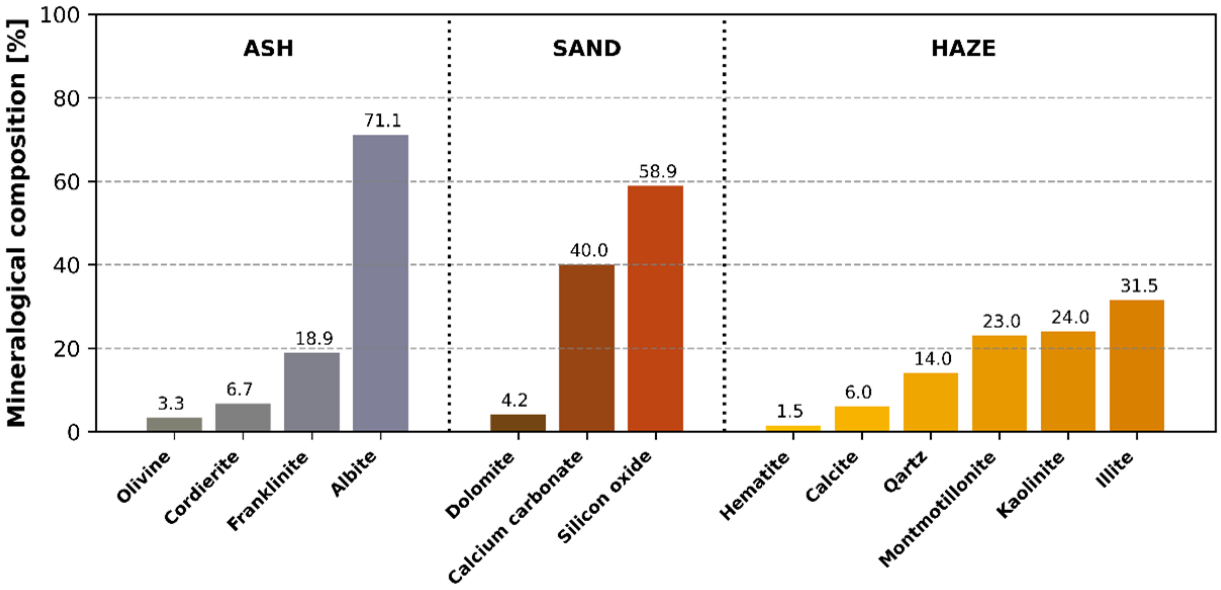

Figure 1-7: Mineralogical composition obtained from XRD analysis (% volume) for ash, sand, and haze particles (acetoguanamine not included)

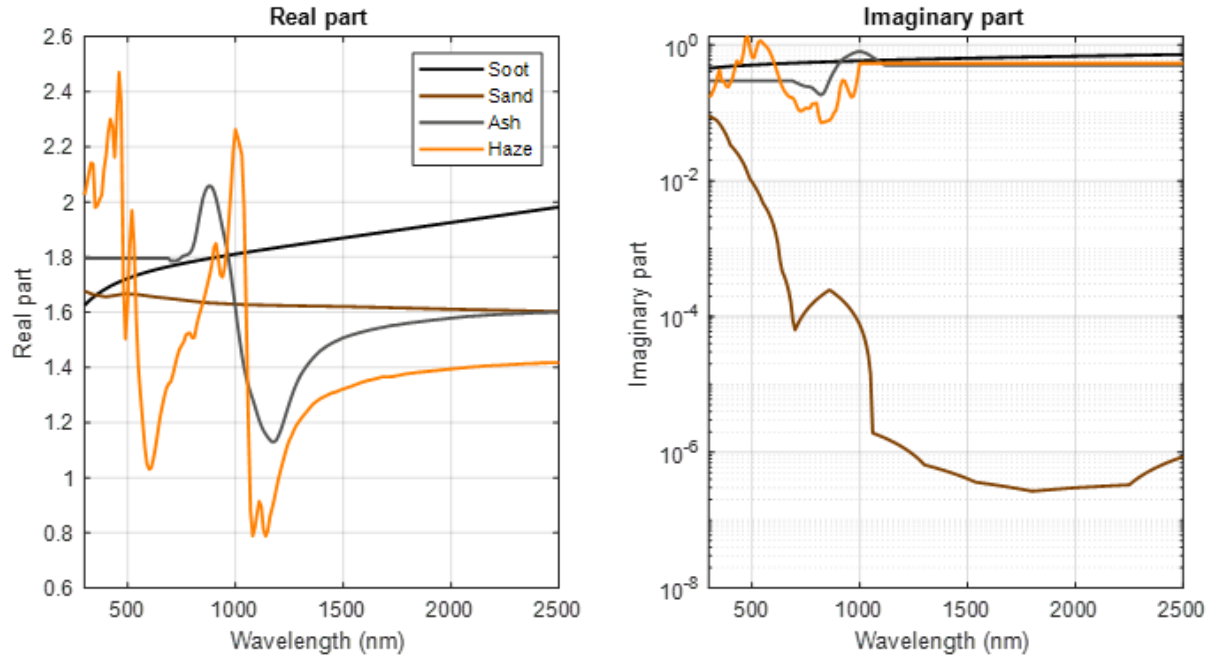

Figure 1-8: Real part and imaginary part of soot, sand, ash, and haze refractive index, obtained with as follows. Soot: correlation proposed by Chang et al. (1990); haze: effective medium model; ash: data from Deguine et al. (2020), and sand: data from Longtin et al. (1988)

Table 1.3: Source for the mineral's dielectric constants.

Aerosol	Mineral	Reference
Ash	Olivine	Fabian et al. (2001)
	Cordierite Franklinite Albite	"Classic Gems" (2022)
Sand	Dolomite	Querry (1987)
	Calcium carbonate	Posch et al. (2007)
	Silicon oxide	Marcos et al. (2016)
Haze	Hematite	Triaud (2005)
	Calcite	Posch et al. (2007)
	Quartz	Calingaert et al. (1936)
	Montmorillonite Kaolinite Illite	Querry (1987)

Refractive indices obtained by the Effective Medium were mostly in good agreement with the literature. The real and imaginary parts of the sand refractive index are of the magnitude of order as the values of Koepke et al. (1997), around 1.5 and 0.001, respectively. For ash, the real part of the refractive index obtained was about 1.6 in accordance with Ball et al. (2015) and Reed et al. (2018) from Etna and Eyjafjallajökull volcanos data, respectively. For the imaginary part, also the data for Ball et al. (2015) agrees with the Effective Medium results. For haze, the value of refractive index agrees with the Patterson et al. (1977) of pure Saharan haze and Volz (1972) values of rainout haze aerosol collected in Germany. In addition, (Balkanski et al., 2007) determined that mineral haze absorbed in short wavelengths spectra is based mainly on an iron oxide formed as Hematite, underlying the necessity of considering this mineral component in a haze.

However, ash, sand, and haze refractive indices were corrected since (1) the dielectric constants of the minerals that contain the materials were not obtained from the exact conditions, (2) absorption coefficients were often missing and therefore they were roughly estimated, and (3) the observed characteristics with the experimental snow contamination (see Results and Discussion section) showed different behavior as the predicted with the refractive indices weigh-averaged. Considering this, for sand, the refractive index proposed by Longtin et al. (1988) was employed, with a higher real part (around 1.65) and more differences in the spectral range for the imaginary part from the results obtained from the Effective Medium. For ash, values from Deguine et al. (2020) considered for the Etan volcano were selected. Before 600 nm a constant value from the initial refractive at this wavelength was established since no data beneath this wavelength was available. In addition, a correction of the imaginary part from 1120 nm was made to a value of 0.5, because differences were seen in this range. This was also based on the low imaginary part of the minerals contained in the ash obtained with the weigh-averaging. For haze, the imaginary part of the refractive index was raised up and established at 0.53 from 1000 nm because the weight averaging decreased too much for the imaginary part. The real part was not modified.

1.5 Results and discussion

With the conditions and parameters specified above, the optical properties of soot, ash, sand, and haze aerosols were determined. The MAC (Mass Absorption Cross Section), MSC (Mass Scattering Cross Section), and SSA (Single Scattering Albedo) are represented in Figure 1-9. As expected, the three optical results depend mainly on the refractive index, and the scattering efficiency is the dominant effect on characterizing the albedo of the particles. Particularly, for each material, different effects are observed. Soot SSA is in agreement with values obtained by Liu et al. (2016) and MAC values agree with those simulated by Kelesidis et al. (2021). Ash SSA also is consistent with values obtained from Piontek et al. (2021) if their results are extrapolated to lower wavelengths. Sand SSA has a similar behavior as the values obtained by Takemura et al. (2002) for soil dust, consisting of

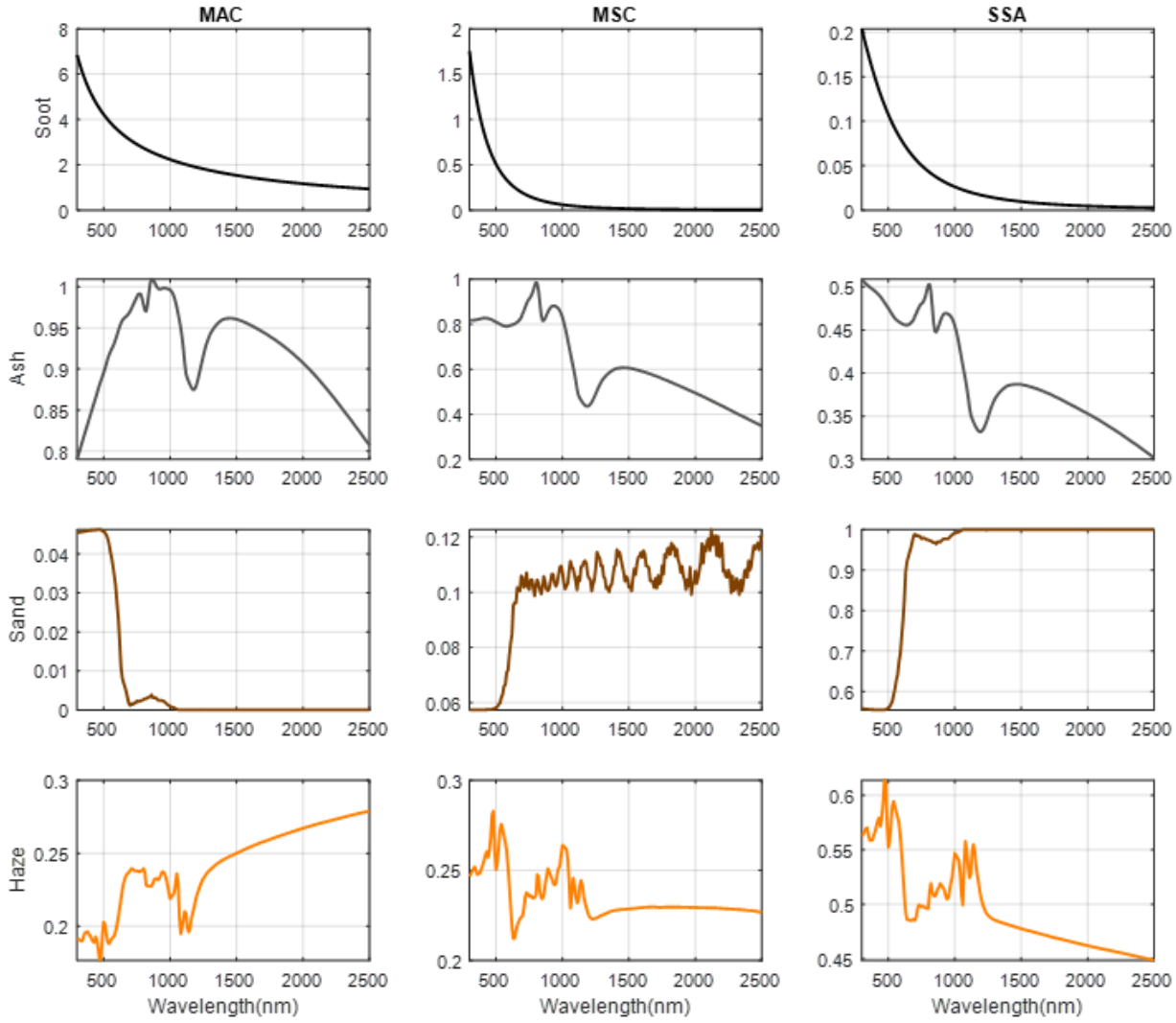

Figure 1-9: Modeled results of MAC (Mass Absorption Cross Section), MSC (Mass Scattering Cross Section), and SSA (Single Scattering Albedo) with the conditions and morphology of soot, ash, sand, and haze.

an increase of albedo as the wavelength increases. However, SSA for haze is lower than most of the values found in the literature. This can be explained by the high variability of the types of haze evaluated.

From the optical properties of the particles used for artificial contamination, albedo results modeled with OptiPar were compared to the experimental data (see Figure 1-10). "Clean" albedo is represented with blue lines in all cases as a reference before contamination. Artificial contamination is represented with different colors depending on the contaminating material (black for soot, grey for ash, orange for haze, and brown for sand). Differences observed in the "clean" albedos are due to different zenith angles, previous deposition of soot, and hour of the day. Modeled results approximately fit the experimental data observed spectrally. However, values below 400 nm are not reliable since the correlation proposed by Chang et al. (1990) slightly underestimates the soot refractive index. Discrepancies can also be observed in the range 1700–2500 nm, where both solar irradiation and snow radiation are very weak (close to zero), and the ratio between them becomes very noisy and erratic, with any minor disturbance (e.g., any minor deviation of the detectors from

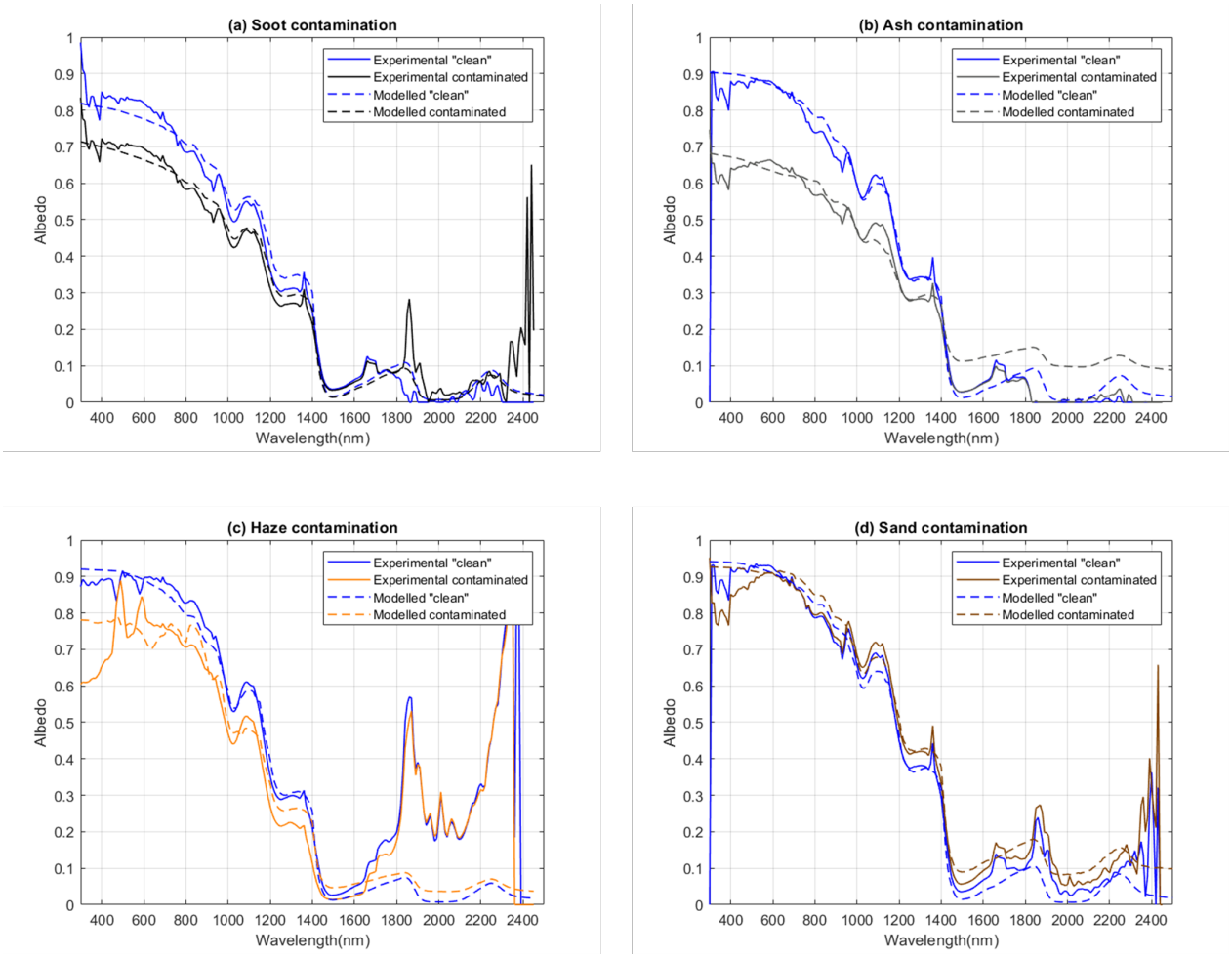

Figure 1-10: Experimental results of snow albedo contaminated with soot (a), ash (b), haze (c), and sand (d). Straight lines correspond to experimental snow albedo and dashed lines to modeled albedo. Blue lines correspond to "clean" snow albedo.

parallelism) being highly magnified. However, the contribution of this discrepancy to the broadband albedo is minor because this is obtained as the integral of spectral irradiation divided by the integral of snow radiation (Lapuerta et al., 2022), and both are very low from 1700 nm onwards.

Figure 1-11 shows albedo reductions from "clean" to a contaminated snow surface. It can be observed that there is a higher albedo reduction in the visible range rather than in the NIR range, as expected. Considering individually each material contamination, soot is by far the one that reduces the most snow albedo, due to its high absorbing light capacity: only 0.7 ppm concentration reduces the albedo in the same order as in the rest cases with much higher concentrations (see Table 1). In absolute values, ash leads to high albedo reductions due to the high concentration of deposited material. The albedo reduction, in this case, reaches 25% in the UV-VIS range (300–800 nm), 13% in the near-infrared (NIR: 800–1400 nm) and it is insensitive in the middle infrared (MIR: 1400–2500 nm). Ash refractive index obtained for this last range has high uncertainty which explains that modeled results do not fit the experimental ones. Artificial soot contamination decreases the albedo by around 14% in the UV-VIS range, whereas in the NIR the decrease is only 7% and it becomes insensitive in the MIR range. Haze has a similar behavior as soot and ash, but the decrease in the albedo remains more uniform. Reductions on the UV-VIS are reduced from 27 to 12% (as wavelength increases), but in the NIR range, a 9% reduction remains uniform and again becomes insensitive in the MIR range. As in the case of ash, modeled results are affected by the uncertainty of the imaginary part. On the contrary, sand albedo reductions are only observed in the visible range (from 10 to 0%), while from 800 nm upwards the tendency changes and the albedo starts to increase (up to 3%) due to the high reflectivity of sand (as observed in the sand SSA in Figure 1-9).

Figure 1-12 shows the broadband snow albedo, calculated as described in Lapuerta et al. (2022), of the "clean" and artificially contaminated snow surfaces, obtained from both the experimental and modeled results. Modeled results fit well the experimental results of both "clean" and contaminated snow broadband albedo. These results show that sand has the opposite behavior to the other materials, where the spectral albedo moves from reductions (UV-VIS) to increases (NIR and MIR). This

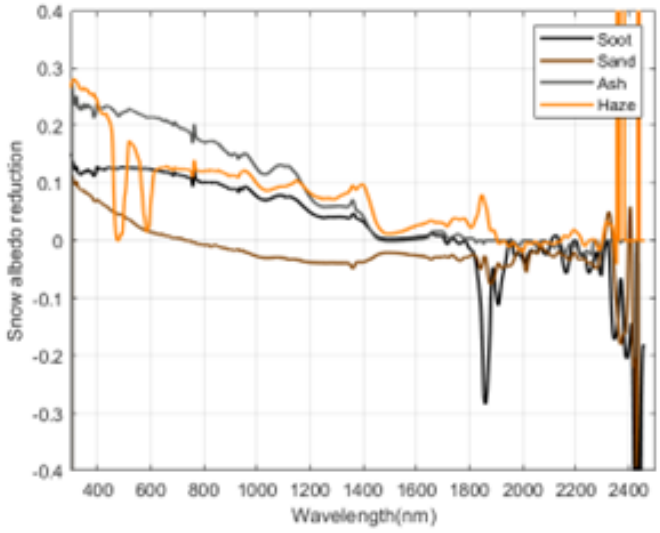

Figure 1-11: Snow albedo reduction from "clean" to contaminated with soot, sand, ash, and haze, obtained from the experimental results. Negative values correspond to snow albedo increases, as in the case of sand.

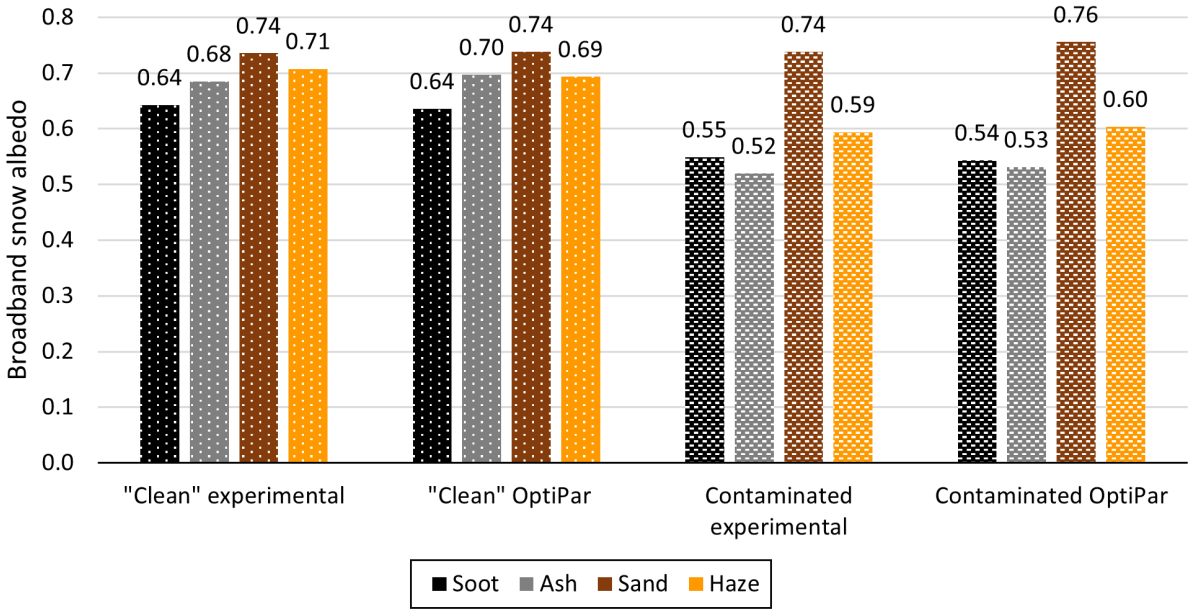

Figure 1-12: Broadband snow albedo of the experimental and modeled with OptiPar of "clean" and artificially contaminated snow surfaces with soot (black bar), ash (grey bar), sand (brown bar), and haze (orange bar).

behavior is self-compensated, leading to similar values of broadband albedo. For all other materials, snow albedo reductions remain (with variable intensity along the range) leading to significant broadband albedo reductions in all cases.

1.6 Conclusions

Particles deposited in snow surfaces decrease the snow albedo differently depending on their composition and concentration. Soot has the highest potential to reduce snow albedo for a given concentration of deposited particles. It decreases substantially the snow albedo in the UV-VIS range (300–800 nm), but such reduction drops down in near-infrared (NIR: 800–1400 nm) becoming insensitive in the middle infrared range (MIR: 1400–2500 nm). Ash has lower albedo reduction potential than soot, although similar distributed along the wavelength range. However, in this case, the uncertainty of the imaginary part of the refractive index makes these results unreliable. Haze has a similar qualitative effect as soot: they both show gradual albedo reduction in the UV-VIS, although soot leads to a sharper reduction in the NIR range. The opposite of this effect can be observed with sand since the observed reduction in the UV-VIS range turns into an increase in the snow albedo in the NIR and MIR range because of the high single scattering albedo of this material. However, this behaviors for sand is self-compensated leading to invariable values of broadband albedo. Modeling reproduces qualitatively spectral tendencies, but they are affected by the hour, site, day of the year, and snow metamorphism. However, despite spectral inaccuracies, broadband albedo simulations agree with experimental results. In general, the refractive index of the materials (soot, ash, sand, and haze) was proved to be the most important parameter for simulations of the optical effects of different contaminating materials. Therefore, a precise determination of the refractive index has been revealed as essential for an accurate simulation.

Chapter 2

Optical effect of Andean Mineral Dust onto snow surface spectral albedo

2.1 Abstract

Light absorbing particles (LAPs) present high absorbance and contribute to reducing the snow albedo when deposited on snow surfaces. This deposition can be caused by aerosols transported from natural or anthropogenic, either distant or nearby, sources. In this study, snow was artificially contaminated with soil samples collected in the Central Andes (near El Yeso dam) to simulate the most common nearby source of Mineral Dust (MD) deposition onto snow surface. Andean soil samples previously conditioned were characterized through Single Particle Optical Sizing (SPOS), X-Ray Diffraction (XRD) analysis, and Scanning Electron Microscope (SEM) for the determination of optical properties of the MD samples. Spectral snow albedo was measured with a spectrorradiometric system. To evaluate the heterogeneity of the particle distribution over the snow surface, aerial photographs were taken with a drone to apply a visual color segmentation of the surface and to determine the equivalent MD concentration. Experimental snow albedo was compared with theoretical values obtained with the OptiPar radiative transfer model. Inputs for the model were: the MD refractive index (calculated from the mineralogical composition and morphology of MD), cloudiness, snow density, surface roughness, snow, and MD grain size, and LAPs concentration (obtained from the snow samples collected during the experiments and analyzed in the laboratory). Small black carbon concentrations were found in natural snow and considered in the simulations. Spectral albedo measurements showed high albedo reductions in the UV and VIS range (300 - 800 nm), being less significant in the NIR range (800 - 1700 nm). A nonlinear behavior was observed in broadband albedo when increasing MD concentration. For lower values of MD concentration (lower than 1500 $mgkg^{-1}$), a significant reduction rate of 0.1 units per 1000 $mgkg^{-1}$ was found , while at higher concentrations (> 3500 $mgkg^{-1}$), such reduction tends to the minimum. Simulated values with OptiPar are in agreement with measured albedo, but some differences are observed, probably due to the refractive index considered, the snow surface roughness, and the non-uniform MD concentration in snow.

2.2 Introduction

Light absorbing particles (LAPs) deposition onto snow, such as mineral dust (MD) or Black Carbon (BC), decreases the surface albedo, due to their relatively high absorbance in the visible wavelength range compared to ice crystals (Warren et al., 1980). This darkening effect has positive feedback on snow metamorphism, not only LAPs radiative perturbation is amplified in snowpacks with larger ice crystals, but it affects further, by enhancing grain coarsening (Hadley et al., 2012; Skiles et al., 2019). Therefore, particle deposition will reduce snow accumulation and will lead to earlier melt-out (Skiles et al., 2019; Tuzet et al., 2017). Previous research has focused on the presence and impact of BC agglomerates in high mountains (Cereceda-Balic et al., 2022; Cereceda-Balic et al., 2018; Gramsch et al., 2020; Li et al., 2020; Santra et al., 2019). However, even considering that MD particles are much less absorptive than BC agglomerates per mass unit (Flanner et al., 2021; González-Correa, Lapuerta, et al., 2022), MD mass concentration onto the snow surface can increase to several magnitude orders, enough to significantly reduce the snowpack albedo (Dumont et al., 2020; Painter, Skiles, et al., 2012; Skiles & Painter, 2017).

It has been well established that the optical properties of MD particles can not be described on a global scale. The mineralogical composition presents high variability between soils, and thus, significant differences in the complex refraction index (González-Correa, Lapuerta, et al., 2022) can be found. In the atmosphere, MD particles can travel long paths, during which aerosols can vary their size or composition due to collisions between particles and by mixing with other compounds. The single scattering albedo of MD particles increases for increasing wavelengths throughout the solar spectrum, and smaller particles exhibit a higher absorption capacity than larger ones, this difference being more important in the UV-VIS wavelength range (Linke et al., 2006; Skiles, Painter, et al., 2017). Therefore, regional characteristics should be taken into account to evaluate the reduction in snow albedo (Flanner et al., 2021).

MD particles can be transported from natural or anthropogenic sources to the snowpacks or glaciers. After Saharan outbreaks, MD deposition onto snow has been observed from the southern Iberian Peninsula (González-Correa, Lapuerta, et al., 2022), and the Alps (Dumont et al., 2020), to the Russian Caucasus Mountains (Dumont et al., 2020). Also, MD particles may be suspended from disturbed soil areas eroded as a consequence of human activities, like in the Rocky Mountains at the Colorado River basin, where resource exploration and settlement expansion, among other activities, have contributed to soil disturbance, and led to an average snow season shortening of three weeks because of MD deposition onto the snowpack, compared to the preindustrial era (Painter et al., 2010).

The Central Andes have been under climatic stress during the last decade. Since 2010, a so-called mega-drought is affecting this region, showing precipitation deficits over 25% and maximum temperatures with increasing trends and wider diurnal range (Garreaud et al., 2017; Garreaud et al., 2020) . These climatic anomalies have favored glacier mass loss (Dussaillant et al., 2019), reduced the snow cover extent area, decayed snow albedo (Malmros et al., 2018), and consequently, decreased runoff magnitudes (Ayala et al., 2020; Migliavacca et al., 2015). According to Garreaud et al. (2017), the precipitation deficit and snowpack reduction have resulted in streamflow anomalies of up to 70% across central Chile. Nonetheless, an increase in melting rates can be expected if particle deposition is taken into account. Surveys around the Central Andes show a considerable effect of non-BC particles, particularly around metropolitan areas and industrial operation sites (Cordero, Sepúlveda, Feron, Wang, et al., 2022). In the Southern Andes, snow sample analyses indicate that the importance of MD in light absorption decreases from the Dry Andes (18^{o}S) until the Lakes District (42^{o}S) (Cordero, Sepúlveda, Feron, Wang, et al., 2022; Rowe et al., 2019). In

Patagonia and Antarctica, the LAPs mass concentration is extremely low to induce any significant effect on snow surface albedo (Cordero, Sepúlveda, Feron, Damiani, et al., 2022; Cordero, Sepúlveda, Feron, Wang, et al., 2022). Cereceda-Balic et al. (2022) compared Olivares Alpha glacier (OAG) with Bello glacier (BG), geomorphically similar glaciers, but BG is located farther from any mining exploration. BC and MD mass concentration onto snow at OAG was 61 and 67 times more than at BG, and trace elements analysis also showed higher content of As and Pb, well known as Cu mining operation indicators and anthropogenic tracers (Cereceda-Balic et al., 2022). Moreover, Barandun et al. (2022) measured traces of pyrite, typically found in hydrothermal alteration zones, and jarosite, which can be found in mine tailings. Consequently, MD deposition onto snow in the Central Andes can significantly alter the surface albedo and melting rates, and therefore, the hydrological cycle of the basin.

Using an experimental approach, this study delves into the characterization of Andean MD particles collected near el Yeso dam. and their optical effect over the snow surface spectral albedo. With this purpose, delimited snow sites were artificially contaminated by the deposition of preconditioned soil collected at El Yeso dam to simulate nearby deposition of MD particles, and perform spectral albedo measurements in natural and contaminated snow. Snow samples were collected for BC and MD concentration quantification, and selected to capture the heterogeneous LAPs distribution. Here, a methodology is proposed to interpret the LAPs concentration surface heterogeneity for modeling spectral albedo, based on RGB vertical photographs. The refractive index of the MD samples was estimated based on their mineralogical composition obtained from X-Ray Diffraction analysis (XRD), and their optical properties were estimated assuming Mie scatterers with a particle size distribution determined via Single Particle Optical Sizing (SPOS). Finally, the particle characterization was used as an input in OptiPar radiative transfer model (Lapuerta et al., 2022), for validation against albedo measurements.

2.3 Methodology

2.3.1 Experimental procedure

2.3.1.1 Description

The experimental campaign took place on August 2022 in El Yeso dam (33.67ºS, 70.09ºW, 2500 m.a.s.l.), Chile. From May to September, nearby routes remain closed to prevent accidents, therefore, the inflow of tourists is minimum and no mining activity is developed nearby. Consequently, it is expected to find a cleaner snowpack since anthropogenic emission sources are reduced. In order to analyze the effect of deposited Andean Mineral Dust (MD) onto snow, five different sites were artificially contaminated with MD preconditioned samples (Section 2.3.1.2), using a regular sieve of 2 mm size, and varying the amount of material deposited (see Table 2.1). Locations were selected nearby but separated far enough to ensure that no particles from any of the previous contamination procedures were deposited on the new site. At each site, albedo measurements were performed on the natural and artificially contaminated surface using a spectrorradiometric system described in Section 2.3.1.3. They were carried out around the solar noon (around 14:00 GMT-4) when albedo reaches the lowest value, to minimize the influence of the solar position on the light scattering pattern of the snowpack. After that, vertical photographs of the surface were taken with a drone to capture the heterogeneity of the particle distribution over the snow surface of the experimental sites (shown in Figure A-4). Snow samples were collected in different places based on a visual color segmentation of the surface, to quantify BC and MD mass concentration using a melt and filtration

methodology (Section 2.3.1.4). For modeling purposes, samples and aerial images were used to estimate an equivalent MD concentration using the methodology proposed in Section 2.3.1.5.

2.3.1.2 MD samples

During the last spring (October 2021) soil samples were collected from the surroundings of El Yeso Dam. Following ISO 11464 standard, samples were dried in an oven at 40^{o}C for 72 hours and sifted with a 2 mm aperture size sieve, discarding the larger particle fraction ($>$ 2 mm). The smaller fraction was used to emulate MD particles during the experiment, according to particle size distributions observed by previous studies (Skiles & Painter, 2017). Hereinafter, the smaller fraction is referred to as MD sample.

To determine optical properties of the MD samples, mineralogical composition, and particle dimensions are required. Particles with sizes between 1.5 to 500 μm were quantified from a subset of the preconditioned samples, using a liquid particle counter based on a Single Particle Optical Sizing (SPOS) method (Accusizer A7000 SIS from Particle Sizing Systems). The liquid sample was prepared with a MD concentration of 6000 mg kg^{-1}, which is close to the mean MD concentration measured at the artificially contaminated snow sites. Finally, an X-ray diffraction (XRD) analysis was conducted to identify the mineral components of the sample and their respective volumetric fraction.

2.3.1.3 Spectrorradiometric system

A spectrorradiometric system manufactured by Avantes was used for surface albedo measurements. The equipment is composed of three pairs of high-spectral resolution field spectroradiometers in UV-VIS (AvaSpec ULS2048CL-EVO, 300-1100 nm), NIR (AvaSpec- NIR512 1.7-HSCEVO, 1000 - 1700 nm), and IR (AvaSpec-NIR512-2.5-HSC-EVO, 1600 - 2500 nm) wavelength ranges with 2.17, 7.0, and 5.7 nm resolution, respectively. Three-furcated optical fibers, with cosine-collector optical diffusers at their ends, allow simultaneous measurement of up-welling solar irradiance and down-welling solar radiance over a 300 to 2500 nm spectral range. Optical fibers were supported over a tripod with an extensible arm that secures a 3 m diameter area of undisturbed snow.

During the MD deposition process, cosine collectors were covered and the extensible arm of the tripod supporting the optical fibers was rotated to avoid pollution of the sensor, and then, it was carefully placed at the same place as the first measurement. Ten measurements were performed per site in no more than 2 minutes (acquisition time depends on the irradiance intensity). A smoothed signal for each measurement is obtained using a Gaussian moving average of $\pm$ 10 wavelength periods (Lapuerta et al., 2022).

2.3.1.4 Snow sampling and laboratory analysis

Snow samples were collected from natural and artificially contaminated snow in Whirl-Pak (Nasco) plastic bags, using plastic shovels and gloves dust-free to avoid external pollution of the samples. All implements used for sample collection were previously washed with Extran phosphate-free detergent, and rinsed with distilled water and with HPLC ultrapure water from a Milly-Q system. First, a sample of undisturbed natural snow of about 1.5 kg was collected before proceeding with the experiment. Once contaminated, samples were arbitrarily collected based on a visual color segmentation of the surface, appointing to cover a wide range of MD concentrations onto the snow. All samples were kept frozen a -20^{o}C until processing.

Following an analytical method (filter-based absorption), snow samples were processed (Cereceda-Balic et al., 2019; Clarke et al., 1985). Samples were completely melted and sonicated to ensure a particle homogeneous distribution. Then, subsamples were collected and mixed with isopropanol (20/80% v/v), to minimize particle adherence to surfaces. Nucleopore polycarbonate filters (Whatman, Darmstadt, Germany) (47-mm diameter, 0.4-μm pore size) were previously weighted and employed for filtration. Details of the filtration system can be found in Cereceda-Balic et al. (2019).

After fully drying at ambient conditions, a SootScan™, Model OT21, Optical Transmissometer (Magee Scientific; Berkeley, CA, USA) was used to estimate BC concentration through optical attenuation measurements at wavelength 880 nm. Attenuation measurements were converted to BC mass concentration as explained by Cereceda-Balic et al. (2022). As recommended by the manufacturer, an upper limit of 125 attenuation unit is adviced to maintain measurements within the transmissometer's linear range

Therefore, the filtered volume of the solution was adjusted to fit within the boundaries. Finally, MD concentration in the snow samples was quantified by weighing the already-dried filter.

2.3.1.5 Equivalent Mineral Dust concentration

LAPs distribution onto the snow surface is spatially and temporally heterogeneous, with overlapping deposition of different aerosols onto the surface. The same issue can be observed in experiments on artificially contaminated snow. These experiments focus on a particular material and time-lapse, most of them addressing BC (Conway et al., 1996; González-Correa, Gómez-Doménech, et al., 2022; González-Correa, Lapuerta, et al., 2022; Hadley et al., 2012; Lapuerta et al., 2022; Peltoniemi et al., 2015), but also Mineral Dust (MD) (Beres et al., 2018), Brown Carbon (BrC) (Beres et al., 2020), sand, and volcanic ash (Conway et al., 1996; González-Correa, Lapuerta, et al., 2022). In these types of studies, one of the main difficulties for a proper comparison between the observed optical effect and theoretical or modeled prediction is the quantification of the LAPs concentration. First, not all experiments have been capable to reproduce a homogeneous contaminated area, unless they are conducted under laboratory-controlled conditions (Hadley et al., 2012), or involve a previuos mixing of snow, which results in altered snow microstructure (Conway et al., 1996). Second, evenly contaminated surfaces with artificially deposited LAPs were achieved just in small areas, like Beres et al. (2018), that could cover a homogeneously distributed area of 65 cm diameter circumference of contamination. Third, large equipment that can hardly be transported on snow landscapes is usually required (Beres et al., 2018). To overcome the heterogeneity in LAPs distribution after artificially contaminate the snow surface a method to estimate a equivalent MD concentration is proposed.

As the cosine collector captures plane irradiance, the contribution of each point on the surface to the measured irradiance depends on the view angle from the sensor axis. Therefore, a method to calculate an equivalent particle mass concentration depending on the view angle and the sensor position is proposed, for application in radiative transfer snow models and for comparison with the measured spectral albedo. To quantify the area from which the sensor is capturing radiation, the view factor (VF) between two parallel plane disks can be calculated according to equation 2.1.

$$VF = \frac{1}{2}\left[S - \left(S^2 - 4\left(\frac{R}{r_0}\right)^2\right)^{0.5}\right]; S = 1 + \frac{1 + \left(\frac{R}{h}\right)^2}{\left(\frac{r_0}{h}\right)^2} \tag{2.1}$$

where, R is the observed radius on the snow surface, h corresponds to the sensor's height, and r_0 is the sensor's radius.

When R increases, VF tends to 1, meaning that the circular shape described by R encloses most of the radiance measured by the sensor (solid-line Figure 2-1). Consequently, the radial contribution to the measured radiance is proportional to the change in the view factor:

$$\frac{\Delta VF(R)}{\Delta R}(i) = \frac{VF(i+1) - VF(i)}{\Delta R} \tag{2.2}$$

This means that areas closer to the sensor's viewing axis have a higher contribution to the light collection than far-away areas. On the contrary, when R increases, the contribution of the additional area to the measured radiance decreases (dashed-line Figure 2-1).

Using equation (2), the mean LAPs concentration at each circular fraction can be obtained depending on the surface radius ($X_{med}(R)$). Then, the equivalent mean surface LAPs concentration (X_{eq}), to be used as input in radiative transfer modeling, can be estimated as:

$$X_{eq} = \frac{\sum_{i=1}^{n} \frac{\Delta VF(R)}{\Delta R}(i) X_{med}(R)}{\sum_{i=1}^{n} \frac{\Delta VF(R)}{\Delta R}(i)} \tag{2.3}$$

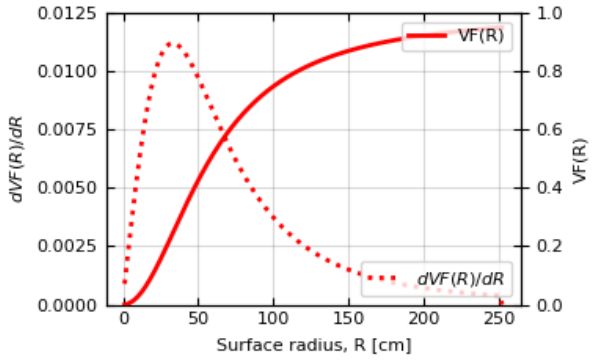

Figure 2-1: View factor (VF) estimated for site 1

To estimate the LAPs concentration in the whole contaminated area, vertical photographs of the contaminated surface were used to correlate the observed reflectance with the LAPs concentration measured in the punctual samples collected. Due to the spectral albedo sensitivity to snow properties or LAPs concentration variations (Dozier et al., 2004), RGB or NIR cameras, as well as hyperspectral measurements, have been used before to estimate grain dimensions, surface roughness or to extrapolate albedo, among others (Manninen et al., 2012; Matzl et al., 2006; Nolin et al., 2000). Such methods rely on particular characteristics of the reflectance spectra of snow to estimate their properties. In this case, the proposed method to extrapolate the LAP concentration over the surface takes advantage that: 1) snow reaches the maximum reflection efficiency in the visible range, and 2) reflectance captured by RGB cameras (VIS wavelength range) is proportional to the broadband snow albedo (Corripio, 2004).

A Mavic Mini 2 drone (lens: FOV 83º, f / 2.8, resolution 4000 × 3000 px) was used for the vertical photographs. Since the pictures only show the contaminated area, the first step is to preprocess the images and to eliminate all artifacts that could interfere. This includes the spectroradiometric system tripod, the optical fibers, as well as their shadows. Then, gaps left can be filled through an inpainting algorithm (Bertalmío et al., 2001). Finally, the aerial image is transformed to a gray-scale reflectance (GSR), and then correlated, pixel by pixel, to MD concentration on the snow surface.

Table 2.1: Snow properties, atmospheric condition, initial MD deposited mass, and sensor height for each measurement site.

Site	T_{snow} ºC	h_{snow} cm	θ' º	n %	β rad	h_{sensor} cm
1	-0.4	35	47	0	0.64	58
2	-0.3	35	46.7	3	0.53	53
3	-0.1	29	49.3	9	0.75	55
4	-0.1	32	52.8	3	0.78	56
5	-0.1	26	56	1	0.50	51

Where, T_{snow} is the snow surface temperature; h_{snow} is the snow depth; θ' is the topographically corrected solar zenith angle; n is the cloud cover; β is the slope angle for roughness microscale modeling; h_{sensor} is the radiance sensor height.

With this aim, areas where snow samples were collected were digitalized separately, calculating the mean GSR capture for each one of them. LAPs concentration of natural snow is related to the GSR of the uncontaminated area of the photograph, GSR_0. This value was estimated by selecting four small areas (0.25 m^2 total), outside the contaminated area. For GSR values below GSR_0 (assumed as the minimum reflectance of natural snow), a linear regression was applied to spatially extrapolate the MD concentration onto the whole snow surface. If the GSR of the pixel is higher than GSR_0, it is assumed to have the same LAPs concentration as the natural snow. Additionally, the GSR_0 value is used as a threshold to define a mask where the snow was artificially contaminated. This way, lower GSR values due to surface characteristics, such as snow roughness, are avoided. Noteworthy, snow roughness was separately calculated for further analysis.

2.3.1.6 Atmospheric conditions and snow properties

To describe snow accumulation and air temperature prior the experiment, data from Laguna Negra weather station (DGA) was used, located at approximately 2 km from the experimental site (-33.67ºS, 70.11ºW and 2780 m.a.s.l.). Before the experiment, a snowfall event took place between August 6th to 7th, resulting in 10 mm. w.e (snow water equivalent, SWE) of accumulation. Air temperature remained low until August 8th, with variations between -11.6ºC to 2.5ºC. From August 9th to 11th, experiment day, air temperature increased, with average daily values between 2.3ºC and 4.9ºC, and maximum values between 8.0ºC and 10.4ºC.

To analyze the results and to model snowpack albedo, snow properties such as grain size, snow density, depth, temperature, and roughness were measured. A summary of these observations is shown in Table 2.1. For the grain size (r_{gs}) measurement, a Canon EOS 80 D camera (Macro Photo Lens MP-E, 65 mm, f/1:2.8, 1-5x, with 010 UV-HAZE Filter MRC nano) was used to photograph snow particles over a 2 mm gridded crystal card. Ice crystals were digitalized and manually masked. Later, ImageJ, an open-source image processing program (Schneider et al., 2012), was used to fit ellipses to each particle and calculate their geometrical characteristics. For all purposes, r_{gs} of a crystal is defined as the radius of an equivalent circumference with the same projected area (Langlois et al., 2020). r_{gs} distribution is shown in Figure A-1 and examples of ice crystal photographs are shown in Figures A-2 and A-3.

To quantify the roughness of the snowpack surface, the methodology proposed by Manninen et

al. (2021) was used. A photograph of the snowpack interface was taken at each measurement point using a dark-gridded boar embedded on the surface, using a Nikkon D5200 camera with an AF-S DX NIKKOR 18-105mm f/3.5-5.6G ED lens. The interface was recognized by image binarization (Manninen et al., 2012), and the slope angle (β) was calculated. As result, β values ranging from 0.50 to 0.78 rad were determined depending on the site.

Snow density was measured at the snowpack top layer (10 cm), using a 12" tube sampler from Snowmetrics tools. The mean snow density on August 11^{th} was 417 ± 57 kgm^{-3}. Snow temperature was measured at the snow surface, using a Snowmetrics digital thermometer, and stayed at near-freezing temperature during the whole experiment. Finally, cloud cover (n) was estimated using hemispherical images of the sky taken while performing the albedo measurements of natural and artificially contaminated snow. Results showed very low cloudiness during the whole experiment, with a maximum of 9% of cloud cover.

2.3.2 Radiative Transfer Modeling

To simulate the spectral surface albedo of snow, OptiPar, a two-stream radiative transfer model with a one-layer scheme, was used (Lapuerta et al., 2022). The model allows to estimate the effects of light absorbing particles deposited onto snow surfaces. It includes the determination of the optical properties of soot agglomerates and ice particles, and new materials can be incorporate as long as their complex refractive index and morphological parameters are known. In this case, a complex refractive index for Andean MD was incorporated.

The snowpack was characterized using properties shown in Table 2.1. In the case of grain size, the median of the masked grains was selected as a representative value for later modeling. On August 11^{th}, the r_{gs} measured was 201 μm which can be classify as a fine grain (Fierz, 2009), and it is around the expected metamorphism after four days from the last snowfall, considering near freezing temperatures at the snowpack surface. According to Skiles and Painter (2017), during the melt season, a maximum mean daily grain size increase of 27 μm can be expected, therefore, no major variations are expected in the albedo due to grain size variations during the day. Because of the snowpack depth, it can be assumed as optically semi-infinite for radiative transfer modeling, meaning that the underlying surface does not significantly impact the snowpack surface albedo (Chen et al., 2014; Kokhanovsky, 2021; Warren et al., 1980). Finally, due to the variability in the slope angle for roughness microscale estimation (β) a mean value of 0.64 was used.

BC particles were assumed as soot agglomerates following González-Correa, Gómez-Doménech, et al. (2022). From previous morphological studies on vehicle-emitted soot (Lapuerta et al., 2009), the following average characteristics were assumed for all agglomerates, neglecting variability: the number of primary particles was assumed as 80, with a monomer radius of 12.5 nm, and a fractal dimension of 1.85. These morphological values were proven as typical for soot agglomerates from road transport (Lapuerta et al., 2009). The refractive index of Chang et al. (1990) was used for soot, and the Rayleigh-Debye-Gans approximation was used (therefore considering primary particles as independent Rayleigh scatteress) with further correction to account for multiple scattering.

To estimate the complex refractive index (or dielectric constant) of the MD used during the experiment, an effective medium model proposed by Bruggeman was used, assuming that the surrounding medium has the same properties than the effective medium (Bruggeman, 1937). The size of MD particles allows simulating their optical properties by applying Mie theory, which requires a spherical representation of the particles. A representative radius was obtained using a volume-weighted average of the particle size distribution estimated through Single Particle Optical Sizing (SPOS). MD particle density was calculated based on the mineralogical composition (Table 2.2).

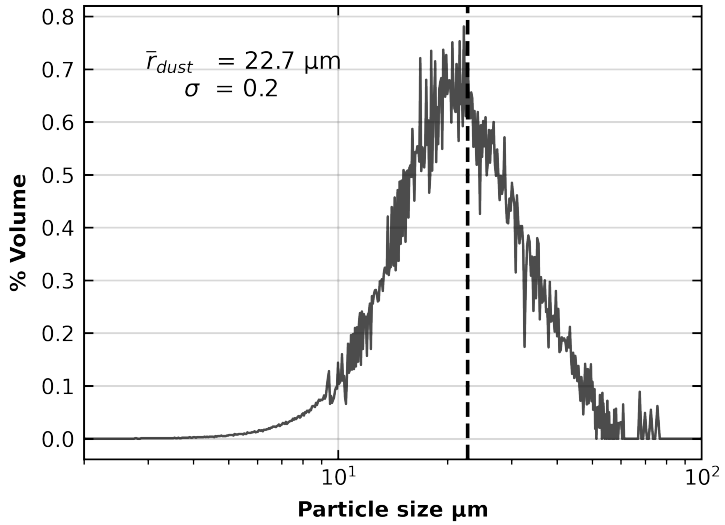

Figure 2-2: Particles radius distribution of MD samples collected nearby el Yeso dam using a Single Particle Optical Sizing (SPOS) method.

Since MD samples were collected in nearby areas that can be exposed during winter time, is possible to assume that MD particles deposited before the experiment have similar optical properties than the artificially deposited samples. Nevertheless, this hypothesis has not proved in the following study, and such assumption can induce uncertainties in the results because aerosols naturally deposited do not necessarily have the same composition nor size distribution.

2.4 Results and discussion

2.4.1 Mineral Dust characterization

To estimate the optical properties of the Mineral Dust (MD) samples, particle dimensions and mineralogical composition were measured. The particle size distribution of the MD artificially deposited is shown in Figure 2-2 in number of particles per mL of liquid sample. An average volume-weighted particle size of the sample was 22.7 μm, with a logarithmic standard deviation for particle radius ($\log(r_{dust})$) of 0.2 μm, and with a distribution shifted towards high values.

XRD analysis shows that the MD samples collected comprise 6 minerals, usually as a product of rock metamorphism in a volcanic ambient with epithermal veins. According to their mass fraction (%), plagioclase feldspars (0.328) are the most abundant mineral particles on the sample, followed by quartz and alkali feldspar (0.305 and 0.250, respectively), comprising approximately 90% of the sample. The remaining 10% is divided between illite, hematites, amphibole, and chlorites. Figure 2-3 displays an example of the SEM image where some of the mineral crystals identified by the XDR analysis can be distinguished based on their habit. Elemental analysis (Table A.1) shows that the sample is rich in silicates, and has a high content of Al, Fe, and K, in accordance with the mineral composition. Based on the feldspar/quartz content of the sample, and following the classification of extrusive or volcanic rocks proposed by Le Bas et al. (1991), the sample can be classified as rhyolites, in agreement with the official geological chart (Instituto de Investigaciones Geológicas, 1980). This suggests that the geological unit where the dam is located comprises a volcanic rock formation

Table 2.2: MD Mineralogical composition. X-Ray Diffraction analysis results

Mineral	Mass fraction	Particle density gcm^{-3}	Reference	Volume fraction	Refractive index
Feldspar (Plagioclase + Alkali)	0.578 (0.328 + 0.250)	2.56		0.611	Egan et al. (1979)
Quartz	0.305	2.66	Scanza et al. (2015)	0.310	Calingaert et al. (1936)
Illite	0.065	2.75		0.064	Egan et al. (1979)
Hematites	0.028	5.26		0.015	Scanza et al. (2015)
Amphibole	0.018	-	-	-	-
Chlorites	0.006	-	-	-	-

from the Cretaceous period, primarily consisting of "andesites and rhyolites, with some continental sedimentary rocks interspersed". In the Central Andes, plagioclases are abundant as a mixture of albite and anorthite, alkali feldspars are commonly found as orthoclase, and as for amphiboles, they are mostly embedded in andesites as hornblende crystals. Finally, chlorite is closely related to hydrothermal alteration, due to the hot water penetration towards deeper layers.

These findings allow assuming that the MD sample used in the experiment contains particles that can be potentially transported by wind gusts from nearby terrain to the surrounding snowpack. The size distribution of MD particles is in accordance with larger estimations of previous analysis performed from snow samples (Lawrence et al., 2010; Skiles, Painter, et al., 2017). Such difference can be explained because gravitational settling favored the loss of coarse particles of MD, meaning that quartz, feldspars, and calcium-rich species rapidly settle and the remaining aerosols in the atmosphere are mainly composed of fine clay particles (Di Biagio et al., 2014). Therefore, a coarse size distribution is more representative of a short-way aerosol transport, i.e. from nearby sources. Finally, no mining traces, such as jarosite or gypsum, were distinguished, despite they were previously found in the glaciers of the Olivares catchment (Barandun et al., 2022). This suggests that mining-derived particles follow restricted transport paths, and therefore, they are not likely to reach the

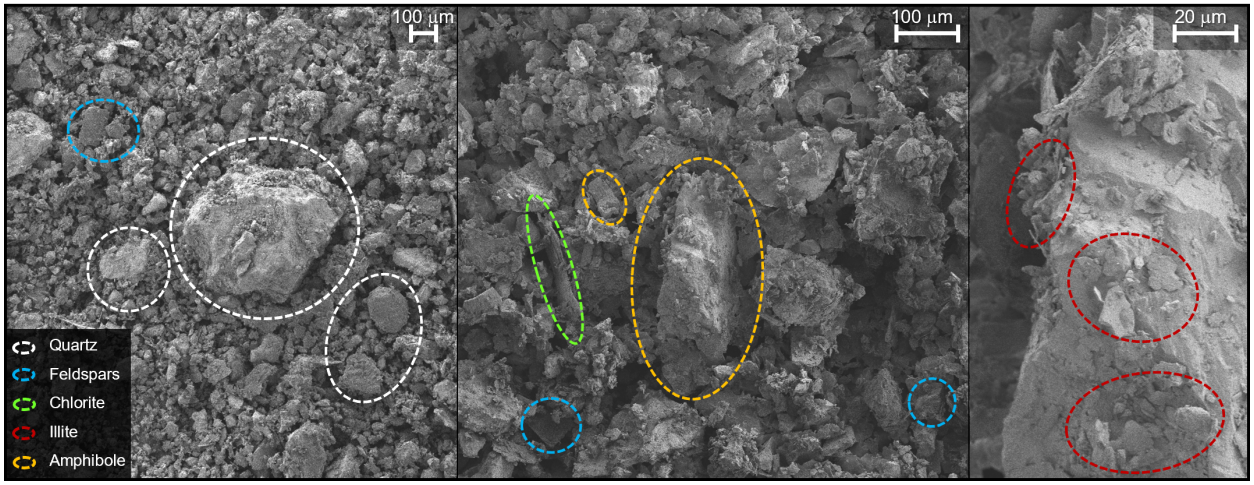

Figure 2-3: Scanning Electron Microscope (SEM) images of the MD sample. Principal minerals found were identified based on their habit.

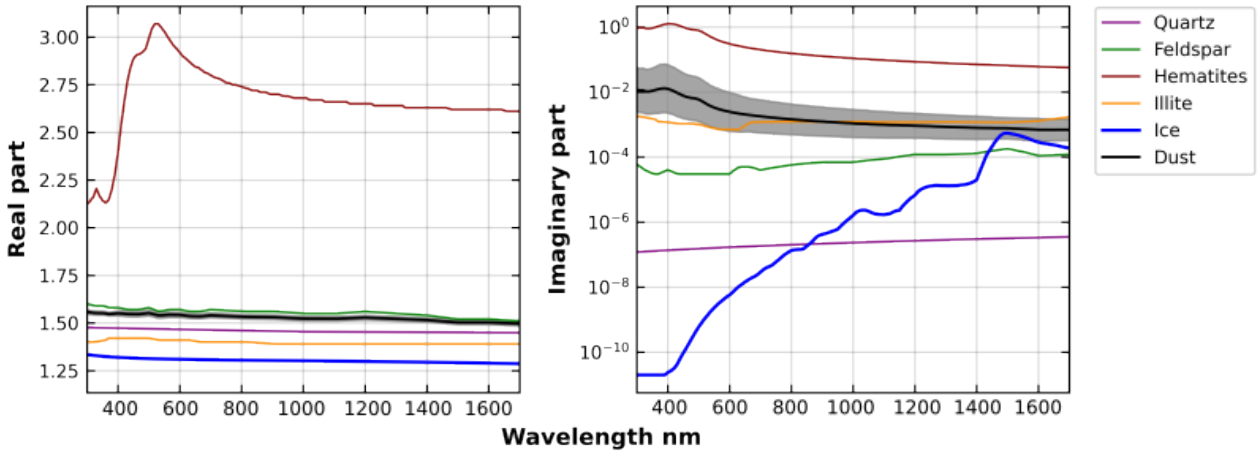

Figure 2-4: Real (left) and imaginary (right) parts of complex refractive index for individual minerals (according to Table 2.2), MD (estimated using Bruggeman effective medium model), and ice (Warren et al., 2008). Shadaed gray area represents one standard deviation variation in Bruggeman estimation in MD refractive index considering volumetric fractions from Table A.2.

dam area.

The effective medium model proposed by Bruggeman was employed to estimate the complex refractive index of MD (Figure 2-4). To apply the model, the volumetric fraction of each mineral was estimated based on the mass fraction and the particle density obtained from the literature (See Table 2.2). Optical constants and particle densities for individual minerals were extracted from the literature (Table 2.2). For the refractive index of quarz, values estimated by Calingaert et al. (1936) were selected among many sources. On the contrary, the complex refractive index of feldspars has been less studied, and consequently, alkali and plagioclase feldspars were considered as a single bulk mineral represented by the refractive index of bytownite (Egan et al., 1979). Bytownite chemical composition indicates the presence of K and Ca, and therefore, of alkali and plagioclase feldspars. Illite and hematite were modeled using the complex refractive index proposed by Egan et al. (1979) and Scanza et al. (2015), respectively. Optical constants for amphibole and chlorites could not be found, thus, the model was applied normalizing the volumetric fractions to the remaining minerals. Such approximation neglects the optical effect of less than 2.5% of the total sample. Finally, variation of the the complex refractive index of MD was estimated considering the mineral composition of all samples listed in Table Table A.2, also collected nearby. Gray shaded area in Figure 2-4 shows one standard deviation variation of the complex refractive index.

Over the analyzed wavelength range (300 - 1700 nm) the real part of the complex refractive (n_{dust}), varies between 1.48 and 1.56. The behavior of n_{dust} is determined by the pure mineral phases, for which n varies slightly across the solar spectrum (Egan et al., 1979; Scanza et al., 2015). On the contrary, the imaginary part (k_{dust}), related to the absorptivity of the MD, decreases across the solar spectrum, reaching lower values at NIR range. k_{dust} reaches a maximum of 0.013 at wavelengths lower than 400 nm and decreases across the visible range until a value of 0.0015 at 800 nm. Further on, minimum values of k_{dust} are found on the NIR range (0.0006), reaching values close to the imaginary part of the refractive index of ice. Additionally, in this case, the absorptivity of MD is highly influenced by iron minerals and clays contained in the samples, primarily hematite (Linke et al., 2006). As can be observed in Figure 2-4, the upper section of the refractive index variation area is representative of samples with higher hematite content, while the lower section indicates a

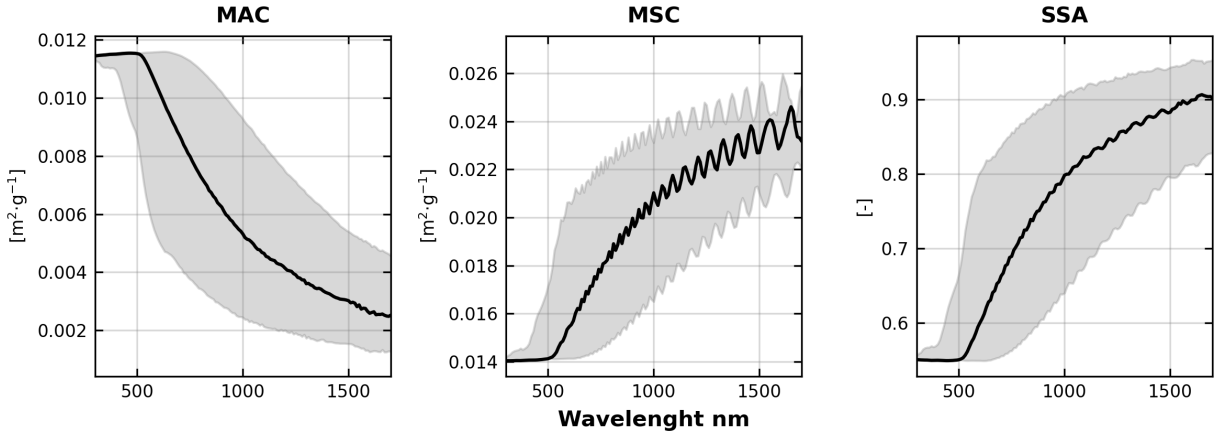

Figure 2-5: Simulated Mass-specific Absorption Cross-section (MAC), Mass-specific Scattering Cross-section (MSC), and Single Scattering Albedo (SSA) for MD samples. Gray shadaed area represents one standard deviation variation in Bruggeman estimation for MD refractive index considering volumetric fractions from Table A.2.

hematite content.

Previous studies also show a large variability of k_{dust}, mainly due to the difference in the mineral composition of MD. Using an inversion technique, which comprised an iterative process to match the Single Scattering Albedo measured of MD with the one modeled with a Radiative Transfer Model, Skiles and Painter (2017) found that k_{dust} of aerosols deposited onto snow and originated in the Colorado Plateau, varies between 0.0015 at 350 nm to 0.0005 at 1500 nm, which is lower than the values obtained here. On the contrary, MD originated from Saharan outbreaks tends to be richer in clays such as montmorillonite, illite and kaolinite (Di Biagio et al., 2014; González-Correa, Lapuerta, et al., 2022), and therefore k_{dust} values of Saharan MD collected in the Iberian peninsula ranged between 0.07 and 1.33 in a similar wavelength range (González-Correa, Lapuerta, et al., 2022), which are higher than the values obtained here. Since our study is focused on short-way aerosol transport, with MD samples rich in silicate minerals, this different absorptivity was expected.

Optical properties of MD particles estimated by Mie theory are shown in Figure 2-5. Low values of the Mass-specific Absorption Cross-section (MAC, Figure 2-5a) were estimated across the solar spectrum, with the highest absorption in the UV range (0.011 $m^2 \cdot g^{-1}$). In contrast, the Mass-specific Scattering Cross-section (MSC, Figure 2-5b) reaches its minimum value in the UV range (0.014 $m^2 \cdot g^{-1}$), increasing through the NIR wavelength range up to (0.024 $m^2 \cdot g^{-1}$). As a consequence, the single scattering albedo (SSA, Figure 2-5c), the probability of a photon to be scattered, increases over the UV-VIS range, and keeps increasing up to ∼0.9 in the NIR range. This behavior in optical properties is typically observed in optical particles of MD and sand (González-Correa, Lapuerta, et al., 2022; Linke et al., 2006), and is consistent with the large size of the MD particles used in this experiment.

Table 2.3: Snow sample laboratory analysis.

Site	c_{dust} $mg \cdot kg^{-1}$	$c_{dust,eq}$ $mg \cdot kg^{-1}$
Natural Snow	85.9 ± 12.8	
1-A	3122.3 ± 480.9	
1-B	2151.7 ± 1446.6	445.6
1-C	1538.5 ± 175.3	
2-A	7190.0 ± 535.4	
2-B	5631.6 ± 502.1	1433.4
2-C	3820.7 ± 74.2	
3-A	13134.8 ± 1388.8	
3-B	7868.8 ± 601.8	4362.4
3-C	2528.4 ± 109.6	
4-A	16244.0 ± 706.2	
4-B	5667.4 ± 430.1	3617.4
4-C	3459.7 ± 545.0	
5-A	5136.8 ± 1175.2	
5-B	3392.2 ± 434.2	513.2
5-C	701.0 ± 70.3	

Where, c_{dust} is the measured dust concentration onto snow surface (average ± standard deviation); $c_{dust,eq}$ equivalent dust concentration estimated according to Section 2.3.1.5.

2.4.2 LAPs concentration

Laboratory analysis of natural snow sample reveals an average BC and MD concentration onto snowpack surface (c_{BC} and c_{dust}) of three samples to be 262.5 ± 26.4 $\mu g \cdot kg^{-1}$ and 85.9 ± 12.8 $mg \cdot kg^{-1}$, respectively, with the values indicating mean ± one standard deviation. Our findings showed a higher c_{BC} compared to the measurements from Cordero, Sepúlveda, Feron, Wang, et al. (2022) and Rowe et al. (2019) at sites close to the metropolitan areas, Santiago, like La Parva or Valle Nevado, were c_{BC} ranged between 27 and 105 $\mu g \cdot kg^{-1}$. At El Yeso dam, Cordero, Sepúlveda, Feron, Wang, et al. (2022) found a c_{BC} on the snow surface of about 10 $\mu g \cdot kg^{-1}$ onto the snow. Such differences might be explained due to the different locations selected for snow sampling in our field camping. Since Cordero, Sepúlveda, Feron, Wang, et al. (2022) attempted to study the regional effect of LAPs on the snow, they collected snow samples in less exposed areas (3015 m.a.s.l.) In the case of c_{dust}, measurements are in agreement with measurements at Olivares Alpha Glacier (153.0 ± 48.5 $mg \cdot kg^{-1}$ at 4520 m.a.s.l), a glacier exposed to mining activities at high altitudes (Cereceda-Balic et al., 2022). Addittionally, a considerable contribution of MD to light absorption have been found in the area based on the absorption Ångström exponent calculated from snow samples (Cordero, Sepúlveda, Feron, Wang, et al., 2022).

Results of c_{dust} in artificially contaminated snow samples are shown in Table 2.3. As the samples were heavily loaded with LAPs, the filtered volume was kept small (< 25 mL) to remain between the attenuation limits of the method used to quantify c_{BC} (Section 2.3.1.4). But, MD mass obtained by the gravimetric method was up to 1.7% of the total filtered mass. Since MD affects the snowpack spectral albedo also at 880 nm, particularly with high MD concentration (see Figure 2-7), big uncertainties arise with the correlation between IR attenuation and BC concentration for the samples

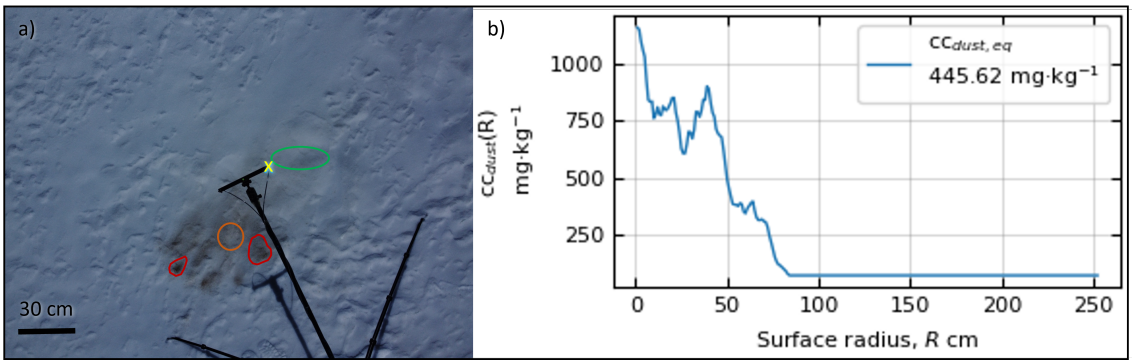

Figure 2-6: (a) Aerial photography of artificially contaminated site 1, captured with Marvin Mini 2 drone, as well as the snow sample areas (red: Sample A; orange: sample B; and green: sample C). "X" indicates the radiance sensor axis; and, (b) Equivalent concentration radial-weighted average.

of artificially contaminated snow. Consequently, c_{BC} in the artificially contaminated samples is not reported. Additionally, measured c_{dust} at samples of artificially contaminated snow are very high compared to natural snow. Therefore, c_{dust} could only be found after severe deposition events, as previously mentioned.

After the laboratory analysis, a MD equivalent concentration ($c_{dust,eq}$) was obtained per site (Table 2.3) to be used as an input in OptiPar Model, due to the heterogeneity in MD distribution onto snow surface after the contamination procedure. As an example, Figure 2-6a shows site 1, after the contamination procedure was completed. As explained in section 2.3.1.5, in the contaminated area of the site, $c_{dust,eq}$ on snow was obtained by correlating the gray scale reflectance, GSR, with the measured c_{dust} from snow samples. Details of the linear regression of sites 1 to 5 are shown in figures A-5 to A-9.

Results show that average radial c_{dust}, Figure 2-6b, decreases with increasing the radius from the sensor axis. This can be explained because most contaminated sections are close to the sensor's vertical axis. In the example of site 1, at approximately 40 cm from the sensor's axis, where high MD concentration areas match with the maximum of the weighting function. In general, calculated $c_{dust,eq}$ values are smaller than the c_{dust} determined through the laboratory analysis (Table 2.3), because the contaminated area comprised a fraction of the total view area of the spectroradiometer, thus, natural snow covers a larger area of the field of view of the instrument.

As already mentioned, MD deposition can lead to a noticeable variation of albedo at visible wavelength ranges. However, other LAPs such as BC, Brown Carbon (BrC), and volcanic ash, among others, can produce a similar effect, drastically reducing the snow albedo at similar wavelengths (Beres et al., 2020; Conway et al., 1996; González-Correa, Lapuerta, et al., 2022). Therefore, a limitation of the proposed method is that it can not differentiate between LAPs. Nonetheless, since MD particles are the predominant LAPs deposited onto the snow after the experiment, it can be concluded that the assumption of uniform distribution for c_{BC} does not impact significantly the results.

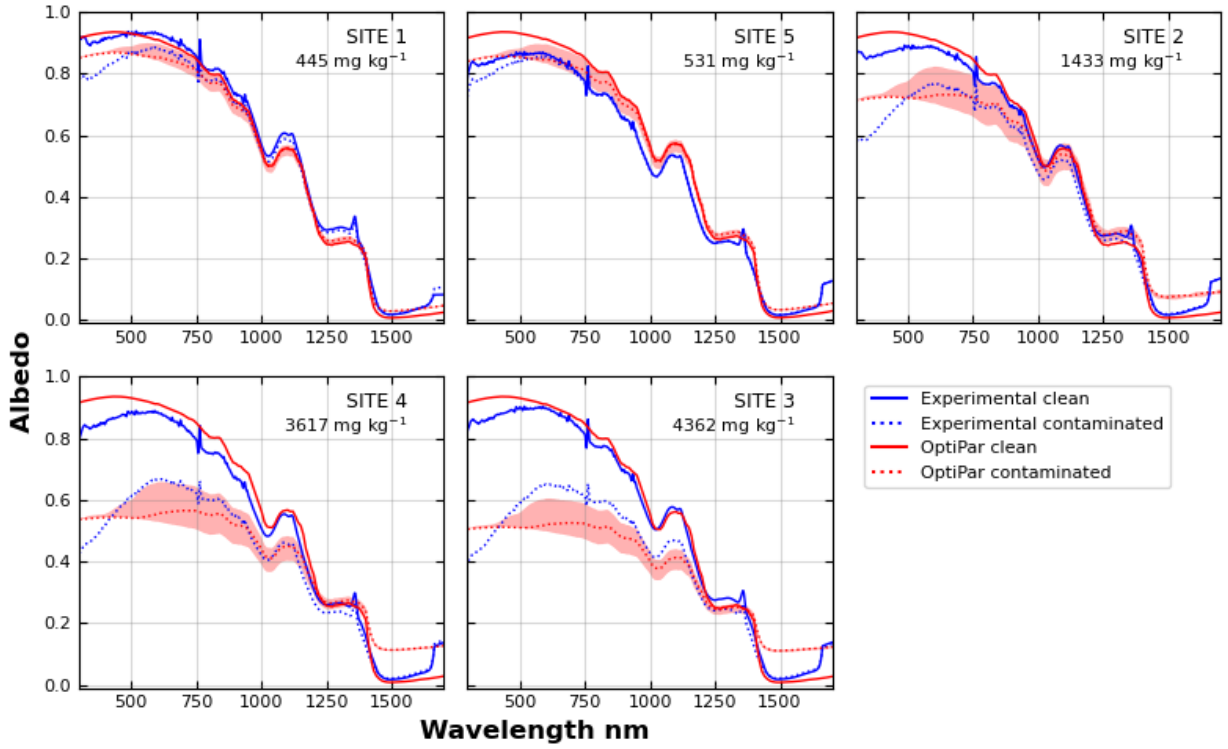

Figure 2-7: Comparison of measured albedo (blue) and OptiPar's modeled albedo (red) at each artificially contaminated site. Solid lines represent natural snow albedo, while dashed lines represent MD-contaminated albedo. Red shaded area indicates variation derived from one standard deviation of the complex refractive index obtained for the dust samples for the contaminated albedo.

2.4.3 Albedo reduction

Figure 2-7 shows the wavelength-wise mean of the ten spectral albedo measurements, for natural (blue solid lines) and artificially contaminated snow (blue dashed lines) at each of the sites. Spectral analysis is limited to the 300 - 1700 nm wavelength range due to the high noise and a poor noise-signal ratio in the region above 1700 nm (Beres et al., 2020; Skiles, Painter, et al., 2017). Results show that albedo reduction ($\Delta\alpha_{wl}$) is prominent in the UV wavelength range located between 300 and 310 nm, ranging between 7.5% at site 5, to 51.6% at site 3. Taking the complete UV-VIS range (300-800 nm), the same behavior is observed, and UV-VIS albedo reduction ($\overline{\Delta\alpha_{300-800\text{nm}}}$) varies between 2.1% and 32.0% for sites 5 and 3, respectively. Further on, it is remarkable that, in less contaminated sites (1 and 5), the reduction in the NIR range ($\overline{\Delta\alpha_{800-1700\text{nm}}}$) was not substantial at low concentrations (3.9 and 0.3% respectively). On the contrary, as MD concentration increases, the impact on snow albedo on NIR range became significant until 1400 nm, like in site 3 (most contaminated) were $\overline{\Delta\alpha_{800-1700\text{nm}}}$ rise up to 19.7%. It is also interesting to note that after 1400, a slight increase in the snow reflectance can be observed, which can be explained by the similar absorptivity (k) between MD and ice crystals in this range (see Figure 2-4). Similar findings were made by González-Correa, Lapuerta, et al. (2022), where a reflection enhancement was observed in the presence of sand deposited onto the snowpack. However, in such case, the reflection was enhanced from 800 nm onwards. The different behavior of sand with respect to MD can be explained by the

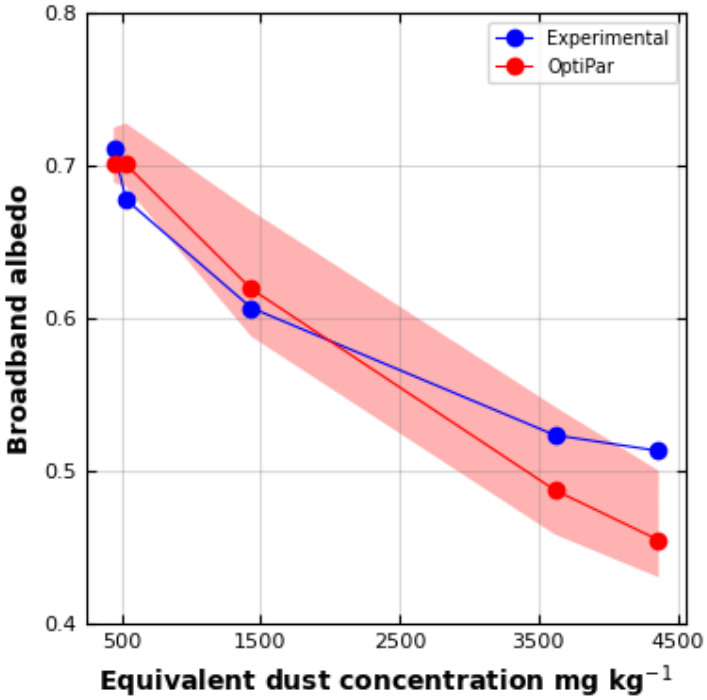

Figure 2-8: Broadband albedo (300 to 1700 nm) of natural and artificially contaminated snow albedo. The red shaded area indicates the variation derived from one standard deviation of the complex refractive index obtained for the dust samples.

differences in the mineralogical composition of the deposited MD.

OptiPar's simulations for natural and contaminated snow albedo (red solid and dashed lines, respectively, in Figure 2-7) agrees with the measurements performed at the experimental sites, and albedo measurements are mostly enclosed with in the range of variation. Across the analyzed spectrum (300 to 1700 nm), an average square difference between 0.0009 and 0.0037 [-] was observed comparing the experimental measurement and the simulated values for natural snow, while for the contaminated snow, the average square difference ranged from 0.0008 and 0.0052 [-], depending on the site analyzed.

In both, experimental and simulated results, a significant decrease can be observed in broadband albedo ($\overline{\alpha_{300-1700\text{nm}}}$) for lower values of $c_{dust,eq}$, showing a nonlinear behavior (Figure 2-8). Reduction rates of $\overline{\alpha_{300-1700\text{nm}}}$ for $c_{dust,eq}$ lower than 1500 mg $\cdot$ kg^{-1} are approximately 0.1 units per 1000 mg $\cdot$ kg^{-1}, for both cases, experimental and simulated. On the contrary, at higher concentrations ($c_{dust,eq} > 3500$ mg $\cdot$ kg^{-1}), such reduction tends to the minimum. Nonetheless, OptiPar's simulations tend to underestimate the $\overline{\alpha_{300-1700\text{nm}}}$, particularly for simulated cases with high concentrations ($c_{dust,eq} > 1500$ mg $\cdot$ kg^{-1}).

Differences observed between measured and simulated albedo can be attributed primarily to errors in estimating snowpack concentrations, the estimated complex refractive index, and the measured snow properties, particularly, surface roughness. First, heterogeneity in LAPs distribution over the snowpack directly affects $c_{dust,eq}$ estimation. For example, the initial deposited mass at site 3 was 50 g smaller than in site 4, but the $\overline{\Delta\alpha_{300-1700\text{nm}}}$ measured was higher (28.9% and 25.7%, respectively). This was captured by the $c_{dust,eq}$ calculated for site 3, because of the highly concen-

trated patches around the sensor axis (See Figures A-4, A-7, and A-8). On the contrary, there is a discrepancy between $c_{dust,eq}$ and $\overline{\Delta\alpha_{300-1700\text{nm}}}$ on sites 1 and 5, showing a more minor albedo reduction (1.7% and 5.9%, respectively) but a higher $c_{dust,eq}$ (445 and 531 $\text{mg} \cdot \text{kg}^{-1}$, respectively). The underestimation might be explained because snow reflection is dominated by forward scattering (Dang et al., 2016), and the directionality of light incidence and reflection was not considered in the methodology to estimate $c_{dust,eq}$.

Secondly, the mineralogical and chemical composition of MD varies depending on the location due to their different geological formation and evolution. However, the availability of information about complex refractive index data for pure minerals, such as feldspars, hematite, illite, amphibole, and chlorite is limited. Adittionally, small differences on the MD composition (volumetric fraction) can induce a wide variation of the results. Despite this, effective medium methods to retrieve the refractive index, with experimental validation, give flexibility for implementation regarding the heterogeneous nature of the deposited aerosols.

Finally, it is worth noting that roughness plays an important role in the albedo variation at the NIR wavelength range. According to the method used (Manninen et al., 2021) to estimate the roughness contribution in OptiPar model, β over 0.5 rad heavily decreases the albedo at NIR wavelengths. For example, considering site 1 in natural conditions, at 1000 nm a slope angle (β) of 0.5 rad (minimum measured) can decrease the snow albedo in 0.04 units. However, if β is increased to 0.78 rad (maximum measured), the reduction can reach 0.21 units.

2.5 Conclusions

Throughout experimental and theoretical methods, this study analyzed the optical effect of Andean Mineral Dust (MD) over the snow surface albedo and their characterizations. Albedo measurements showed albedo reductions higher in the UV and VIS range (300 - 800 nm), particularly between 300 and 310 nm, reaching a reduction of 51.6% in the most experimentally contaminated sites. On the contrary, albedo reductions were less significant for NIR range (800 - 1700 nm). A nonlinear behavior was observed in broadband albedo ($\overline{\alpha_{300-1700\text{nm}}}$) for lower values of $c_{dust,eq}$, with an average reduction rate of 0.1 units per 1000 mgkg^{-1} for $c_{dust,eq}$ lower than 1500 mgkg^{-1}, for both experimental and simulated cases. Simulated values with OptiPar are in agreement with measured albedo, but some differences are observed, which are probably related to the complex refractive index estimated, the high snow surface roughness, and the estimated MD concentration in snow.

MD deposition during the experimental procedure was heterogeneous, and therefore, the artificially contaminated sites presented significant differences in polluted areas. Most of the accumulated MD was located just beneath the cosine collector and the optic fiber of the spectroradiometric system, therefore covering a limited of the viewed area. Nonetheless, calculating an equivalent MD concentration considering visual color segmentation was useful to account for these differences.

XRD analysis and SEM images allowed classifying the compounds of the Andean MD into feldspar, quartz, illite, hematites, amphibole, and chlorites, in agreement with the geological formation at the dam location. Additionally, the particle size distribution measured was within the range of larger MD particles previously found in the snow, and also indicates that the soil surrounding the dam area presents physical characteristics that allow assuming that only short-way transport of MD particles is possible.

Chapter 3

Snow energy balance and radiative transfer model coupling for quantifying BC and dust impact on Juncal River Basin hydrology

3.1 Abstract

Light absorbing particles (LAPs) deposition onto snow surface increases the shortwave radiation absorption and accelerates melting. Aside from individual snow sampling to quantify the deposited LAPs, like Black Carbon (BC) and mineral dust (MD), their impact over time in Central Andean hydrology remains uncertain. In this study, Utha Energy Balance (UEB) snow model and OptiPar radiative transfer model have been coupled through an empirical approach to simulate the accumulation and depletion of snowpack and quantify the effect of LAPs deposition on snow albedo and melting on a time scale basis (2014-2019) at Portillo weather station located in the Juncal River Basin, Chile. Here, the snowpack was simulated using a layered scheme to reproduce snow metamorphism, while energy balance is focused on the snow surface. An initial grain size is assumed after each snowfall event, with subsequent evolution based on empirical grain growth rates considering snow temperature and depth. To account for LAPs, BC and MD, dry deposition rates onto snow were used as tuning parameters and constant for the period analyzed. LAPs mass accumulates in the upper layers, while also considering a fraction of BC agglomerates can scavenge based on melting magnitude. The model was calibrated at a specific location within the basin, corresponding to the Portillo weather station, considering Snow Water Equivalent data measured at the same place. Calibration was performed using the Shuffle Complex Evolution method (SCE-UA), and a leave-one-out cross validation approach. Albedo simulations from OptiPar were validated based on field measurements at Nunatak Laboratory, located in Portillo at 2800 m.a.s.l in the same catchment. Results here support that BC and MD emissions can alter the energy budget of the snowpack, reducing the maximum accumulation and inducing an early melt-out of the seasonal snowpack of up to 3 days, compared to a scenario with no contamination, depending on the year simulated. Additionally, the most significant impact is induced by BC particles due their higher absorption capacity compare to MD.

3.2 Introduction

Light-absorbing particles, known as LAPs, are recognized as contributors to Climate Change, originated from both, natural and anthropogenic sources (Myhre et al., 2013). When these particles, including Black Carbon (BC), Brown Carbon (BrC), Volcanic Ash, and/or Mineral Dust (MD), deposit onto snow or glaciers, they darken the surface and reduce the surface albedo (Beres et al., 2020; Constantin et al., 2020; Skiles & Painter, 2017; Zhong et al., 2019). It also triggers a process referred as feedback effect, where snow grain metamorphism is induced due to the additional energy available in the snowpack (Hadley et al., 2012; Skiles & Painter, 2017). As a result, LAPs directly influence the energy balance by enhancing the absorption of shortwave radiation, inducing snowmelt (Li et al., 2020; Painter et al., 2010). Consequently, it is essential to evaluate the significance of LAPs deposition impact on the snowpack, particularly in basins that rely on snow accumulation for water supply, such as the ones located in the Central Andes.

Given that the Central Andes has been affected by a mega-drought since 2010, with increasing temperature trends and annual precipitation deficit (Garreaud et al., 2017; Garreaud et al., 2020), glacier retreat (Dussaillant et al., 2019), and snow cover and albedo decrease (Malmros et al., 2018; Shaw et al., 2021), to understand the impact that these particles induce in snow cover duration and accumulation open possibilities of mitigation of these consequences on the Andean cryosphere. Surveys have reported different magnitudes of LAPs concentration onto snow, where the most contaminated areas have been found in the Central Andes, near the most populated cities of Chile, with significant amounts of BC particles on snow (Cordero, Sepúlveda, Feron, Wang, et al., 2022; Rowe et al., 2019). At Portillo, BC concentration on snow surface has been linked to vehicle soot emissions due to the intense traffic of buses and heavy trucks (Cereceda-Balic et al., 2018; González-Correa et al., 2023). Simultaneously, suspended MD particles from mining blasting and tailings have been found deposited on glaciers located at the Olivares river basin (Cereceda-Balic et al., 2022), with specific minerals related to copper mining operations (Barandun et al., 2022). Aside from snow sampling survey campaigns to quantify BC and MD concentrations, their impact over time in Central Andean hydrology is still uncertain.

The following study aims to analyze the impacts con BC and MD deposition onto the snow surface, regarding the snowpack albedo and snowpack duration. For this, the physical-based snow model Utha Energy Balance (UEB) was coupled with OptiPar radiative transfer model to simulate the snow accumulation a depletion, and at the same time consider specific particle characteristics, on a time scale basis. In this study, the model was calibrated only in a specific location in the basin (Portillo Weather Station), with the purpose of an extended application to the entire basin in the future, once the deposition rates BC and MD, or directly concentrations of BC and MD onto snow surface, can be spatially estimated. The paper is organized as follows: Section 3.3 describes details of the study area; Section 3.4 describes the models used and the empirical approach used to couple both, radiative transfer and snow energy balance models; Section 3.5 presents results and discussion regarding the model calibration and the effects of LAPs onto the snow cover; to end with conclusions presented in section 3.6.

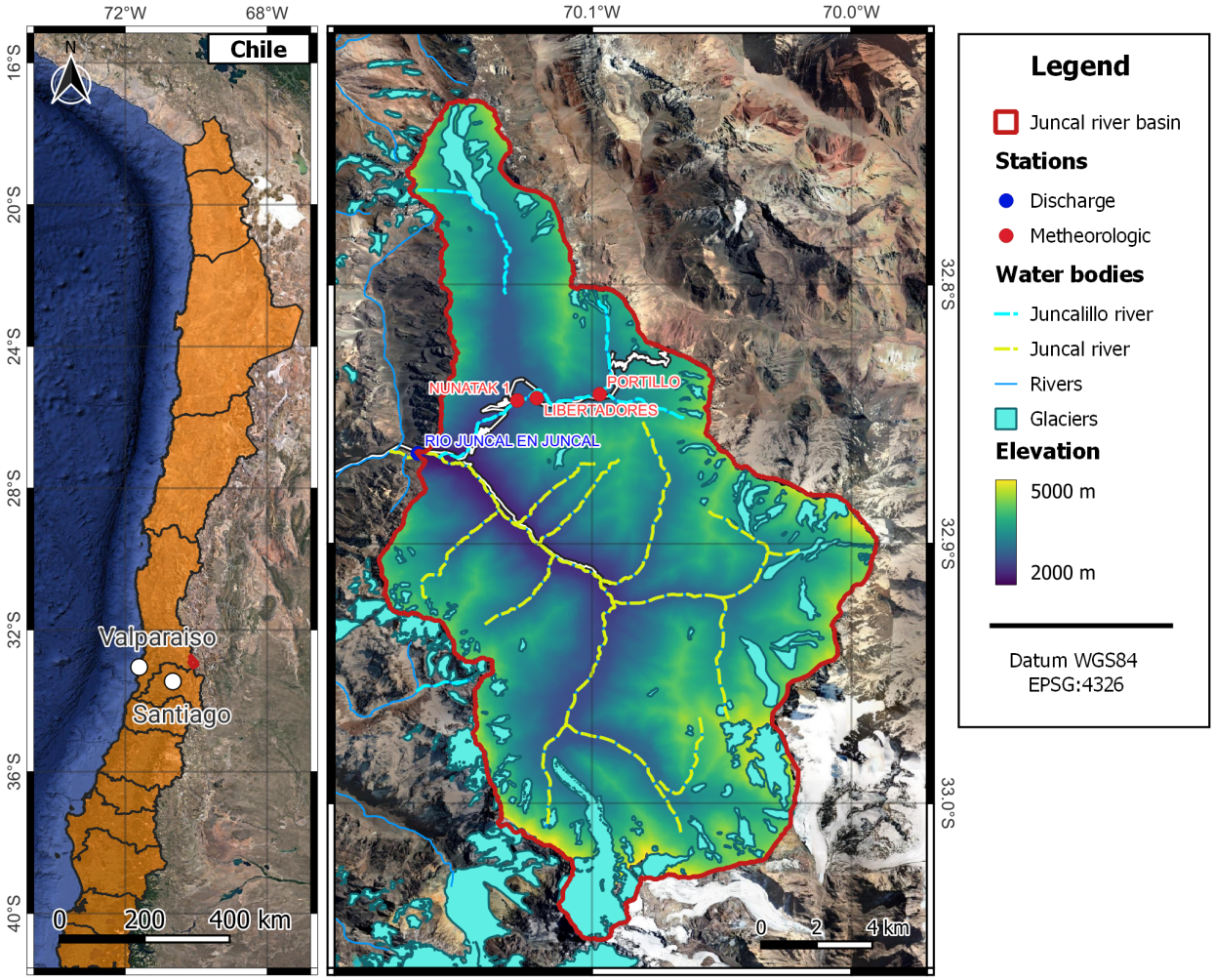

Figure 3-1: Study Area. Overview of the Juncal River Basin located in Valparaiso Region, Chile.

3.3 Study area

The Juncal river basin is approximately located at 32.9°S and 70.2°W in the Central Andes, less that 100 km away from Santiago, capital of Chile. The basin is part of the Aconcagua Basin, which is particularly important for human water supply, agricultural and industrial activities of the Valparaiso region (Webb et al., 2020). It covers an area of 341 km^2 and comprises a wide altitude range from 2200 to nearly 6000 m.a.s.l. This region is characterized by a cool-summer Mediterranean climate with strong seasonality, where winter precipitations are dominated by cold fronts of synoptic scale originated at mid-latitudes storms over the Pacific Ocean and passing through Chile. The high altitude and complex topography of the Andes influence cold fronts, intensifying precipitations while air masses reach the foot of the hills (Falvey et al., 2007), and facilitating snow accumulation over the mountains during cold winters.

Three weather stations are located inside the basin (Figure 3-1). While Portillo and Juncal en rio Juncal weather stations are managed by the *Dirección General de Aguas de Chile* (DGA), Los Libertadores weather station is managed by *Dirección Meteorológica de Chile*, and together

provide hourly meteorological information of the basin, such as temperature and relative humidity data. Additionally, Portillo station also collects snow-related data (snow depth and snow water equivalent, SWE), and Juncal en rio Juncal station provides water discharge information. Finally, a laboratory refuge named NUNATAK-1 is located nearby Portillo. The Laboratory is property of the *CETAM - UTFSM*, and measures atmospheric variables such as incident and reflected radiation (shortwave and longwave), air quality, and meteorology.

3.4 Methodology

3.4.1 Description

To study the impacts of LAPs deposition onto the snow cover, the Utha Energy Balance (UEB) was coupled to the radiative transfer model OptiPar. Details of the particular model set-up are given below. Briefly, since UEB does not simulate the snow microstructure and LAPs accumulation through the snowpack layers, an empirical representation of the snow stratigraphy is used to estimate essential properties for the radiative transfer model such as grain size variation and LAPs concentration. Across the simulation, OptiPar takes the snow properties of the superficial layers at each time step to calculate the snow surface spectral albedo.

3.4.2 Snow Model

The Utha Energy Balance (UEB) is a physical-based snow model, that solves the energy and mass balance of a snowpack using a single-layer configuration for the snowpack (Tarboton et al., 1994). This model has been previously applied in snow-controlled basins in the USA (Tarboton et al., 1994; You et al., 2014), Morocco (Schulz et al., 2004), among others. The model simulates the accumulation and melting of a snowpack characterized by two state variables: the snow water equivalent (SWE) and the energy content (U). Figure 3-2 shows a scheme of energy fluxes represented by the model. Here, the internal energy variation ($\frac{dU_i}{dt}$) depends on the radiation and heat exchange with the surface and the ground:

$$\frac{dU_i}{dt} = Q_{nr} + Q_e + Q_h + Q_r + Q_g - Q_m \tag{3.1}$$

where, Q_{nr} is the Net Radiation Flux, which is the sum of Incident ($Kins$) and outgoing ($Kotu$) solar radiation, and Incident ($Lins$) and outgoing ($Lotu$) thermal radiation, all in $[\mathrm{kJ} \cdot \mathrm{g}^{-2} \cdot \mathrm{h}^{-1}]$, Q_e and Q_h are the turbulent fluxes of latent and sensible heat in $[\mathrm{kJ} \cdot \mathrm{g}^{-2} \cdot \mathrm{h}^{-1}]$, Q_r and Q_g is the heat provided by precipitations and ground heat conduction in $[\mathrm{kJ} \cdot \mathrm{g}^{-2} \cdot \mathrm{h}^{-1}]$, and, Q_m advective heat flux due to snowmelt in $[\mathrm{kJ} \cdot \mathrm{g}^{-2} \cdot \mathrm{h}^{-1}]$. The internal energy U is defined relative to the freezing point of water, and therefore, it corresponds to the cold content of snow (DeWalle et al., 2008). Fixed and calibrated parameters are shown in Tables B.1 and B.2, respectively.

In the case of snow water equivalent variation ($\frac{dSWE_i}{dt}$) this is expressed as:

$$\frac{dSWE_i}{dt} = P_r + P_s - M_r - E \tag{3.2}$$

where, P_r and P_s are the liquid and solid precipitation rates in [m] respectively, M_r is the melting rate of the snowpack in [m], and E is the evaposublimation or condensation rate of the snowpack in [m].

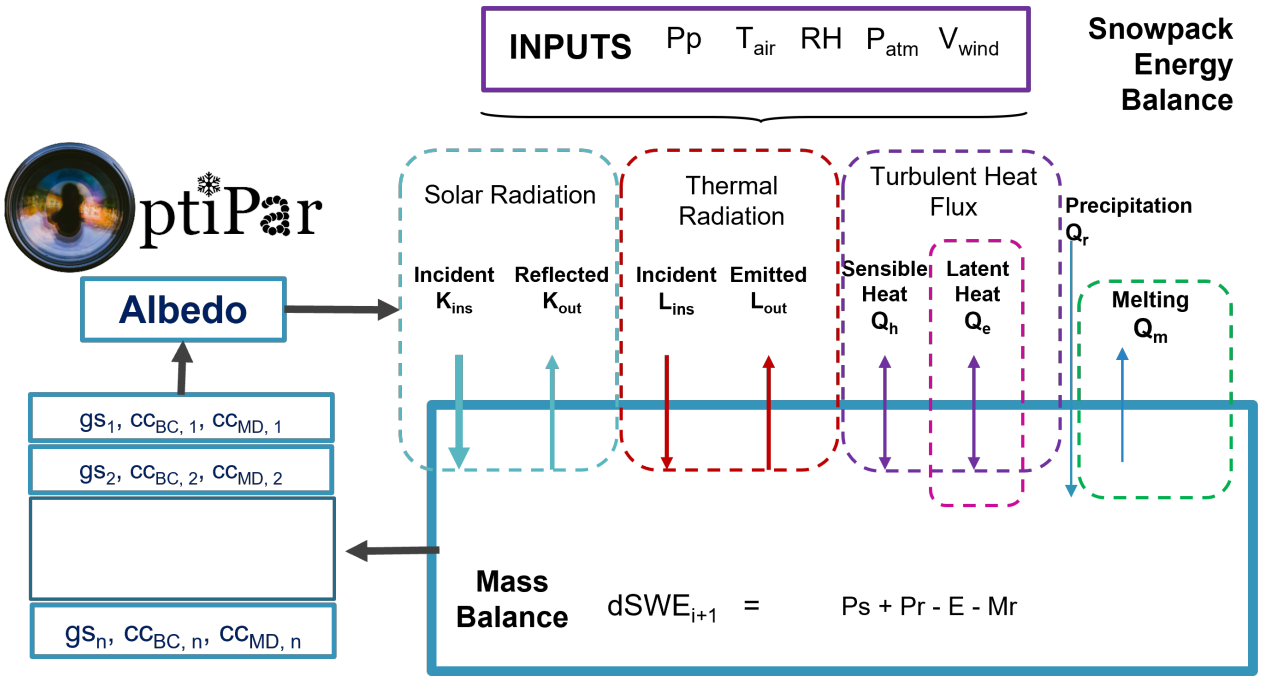

Figure 3-2: Utha Energy Balance (UEB) and OptiPar radiative transfer models coupling scheme.

3.4.3 Snowpack stratigraphy

An empirical approach is followed to simulate the snowpack stratigraphy considering metamorphism, and LAPs accumulation (Black Carbon and Mineral Dust). When a snowfall occurs, a new snow layer is created with a height depending on the accumulated snow ($\frac{dSWE_i}{dt}$) at the current time step and snow density of the model. Then, grain size and BC and MD concentration onto each snow layer (gs_i, $cc_{BC,i}$, and $cc_{MD,i}$, respectively in Figure **??**) is stored in different variables, and then updated independently each time step. Worth noting that this stratigraphy representation is not directly involved in the energy balance, but it stores important variables for the simulation of the surface albedo, such as snow grain size and LAPs concentration.

Initially, each new layer is simulated with a grain size of 100 μm, representative of the ice crystal size of fresh snow. According to laws of snow metamorphism proposed by Brun et al. (1992), the mechanism depends on the temperature, temperature gradient, and the liquid water content on the specific layer. Since the temperature gradient through the snow depth is not simulated by the UEB model, a simplified approach has been used to simulate the metamorphism of ice crystals. Here, the snow aging is simulated as a grain size increase at a constant rate that depends on the thermal state of the snowpack and the snow depth. Following Skiles and Painter (2017) results, when the snowpack transitions to an isothermal, the average rate of grain growth through the snowpack increases. Grain size increase rates used are shown in Table B.3 (Appendix B).

In the case of LAPs accumulation, it is simulated through dry and wet deposition processes. After a snowfall, BC and MD mass is accumulated from the snowpack surface depending on a specific wet deposition rate, and it will be uniformly distributed over the new snow layer. For the case of dry deposition is also simulated with a LAP dependent rate, but it is uniformly distributed over the first 5 mm according to Clifton et al. (2008) results. They show that wind-pumping onto snow affects between 1 and 10 mm from the snowpack surface, and therefore such distance will be

enough to represent the LAPs penetration onto the snowpack. Additionally, when melting occurs small particles are prone to scavenge towards deeper layers, depending on their affinity with water and their size (Conway et al., 1996). Here, we consider that if melting occurs from the snowpack surface, scavenging will be dependent on the amount of melted snow and a scavenging coefficient. For BC particles, a 5% scavenging coefficient since because recently emitted soot particles are mainly hydrophobic (Flanner et al., 2007; Tuzet et al., 2017). On the contrary, the scavenging coefficient for MD particles was set to 0% since they are considered too big to scavenge (Tuzet et al., 2017).

3.4.4 Radiative Transfer Model coupling

The original UEB model relies on Dickinson et al. (1993) model to estimate broadband albedo. The formulation has a dimensionless variable that represents the snow surface age, which is calculated each time step depending on the meteorological conditions. Nonetheless, this method does not account for an explicit representation of LAPS onto the snow surface. For this purpose, is necessary to couple the model with a more complex model that considers the specific optical properties of each type of particle contamination. Here, OptiPar radiative transfer model has been chosen to model snowpack spectral albedo. OptiPar is a two-stream radiative transfer model developed at the University of Castilla-La Mancha (Lapuerta et al., 2022), which has been mainly used for the determination of optical properties of soot agglomerates, ice particles and LAPs contaminated surfaces.

Ice crystals were simulated as isolated spherical ice particles and Mie solution was employed, considering the Warren et al. (2008) complex refractive index. Macke et al. (1996) asymmetry parameter was uses, corrected with the Delta-Eddington approximation (Joseph et al., 1976) to account for multiple scattering among snow grains. The snowpack was considered to be optically semi-infinite, and properties like snow density and zenith angle were taken directly from the UEB model.

LAPs characteristics were simulated considering their specific characteristics. Soot agglomerates were considered as Rayleigh scatters due to their size and the complex refractive index proposed by Chang et al. (1990) together with the Rayleigh-Debye-Gans approximation was considered, allowing to include their morphology into the model. Morphological soot agglomerates characteristics were taken from Lapuerta et al. (2009), neglecting their variability, and thus were simulated as agglomerates composed by 80 primary particles with a 12.5 nm of monomer radius, and a 1.85 of fractal dimension. In the case of MD particles, Mie solution for spherical particles was employed, with a complex refractive index estimated using an effective medium approximation proposed by Bruggeman (1937) This approximation considers the volumetric fractions of each mineral that constitutes the MD (see Chapter 2). A particle size (radius) of 11 μm was employed for optical properties calculation, estimated as the average volume-weighted radius calculated from a laboratory particle-size analysis of MD from a snow sample.

Finally, to calculate the broadband albedo, the integration of the spectral albedo across the solar radiation wavelength range (300 to 2500) was performed considering a solar irradiance spectrum obtained using Bird et al. (1986) approach. To speed up computation time, a spectral look-up table of solar irradiance spectra was built depending on the zenith angle and considering normal atmospheric conditions for winter time. Once estimated, if the snow depth was sufficiently low (< 10 cm), Dickinson et al. (1993) approach was used to weigh the result with underlying surface albedo.

3.4.5 Calibration and analysis

The coupled model was calibrated using the Shuffle Complex Evolution Method (SCE-AU) (Duan et al., 1993), which has been widely use to evaluate performance of hydrological models. Briefly, the method searches for global optimal solutions through a random parameter selection, a competitive complex evolution using a unique objective function, and a selection of the best set of parameters using a SIMPLEX method. Kling-Gupta efficiency statistic, KGE (Gupta et al., 2009; Kling et al., 2012), was used as the objective function to evaluate the calibrated of the model, comparing simulated and measured Snow Water Equivalent (SWE) daily series, measured at Portillo weather station. Additional evaluation metrics used are shown in Table 3.1.

Table 3.1: Evaluation metrics.

Parameter	Description
KGE	$1 - \sqrt{(r-1)^2 + (\beta-1)^2 + (\gamma-1)^2}$
r	$\frac{\sum_{i=1}^{n}(O_i-\bar{O})(S_i-\bar{S})}{\sqrt{\sum_{i=1}^{n}(O_i-\bar{O})^2 \sum_{i=1}^{n}(S_i-\bar{S})^2}}$
β	$\frac{\bar{S}}{\bar{O}}$
γ	$\frac{\sigma_S}{\sigma_O}$
NSE	$1 - \frac{\sum_{i=1}^{n}(O_i-S_i)^2}{\sum_{i=1}^{n}(O_i-\bar{O})^2}$

where O_i and S_i are the observed and simulated values, respectively; $\bar{O}$ y $\bar{S}$ are the average of the observed and simulated values, respectively; and σ_S y σ_O correspond to the standard deviation of the observed and simulated values, respectively.

The model was calibrated at the Portillo station location for the period 2014 to 2019, employing a leave-one-out cross-validation strategy, which means that each year is used once for validation. Specifically, the data for that year is excluded during the model's calibration phase. After the model is calibrated using the remaining data, it is then evaluated using the excluded information. By applying this method, six distinct sets of optimal parameters can be obtained. Finally, a model optimal was estimated as the average value per parameter, from the optimal parameters set previously calculated.

Once calibrated, the albedo simulation was compared to Nunatak's data. The laboratory collects radiation data using a radiometer Kipp & Zonen CNR4. In this case, to obtain the snow surface albedo, the down-welling and up-welling radiation is measured using pyranometer's data (with sensitivity from 10 to 20 $\mu\mathrm{V} \cdot \mathrm{W}^{-1} \cdot \mathrm{m}^{-2}$ and maximum uncertainty of 5% at 95% confidence level), which covers a solar spectral range from 300 to 2800 nm. Broadband albedo measurements from Nunatak are available since 2017. Before to compared, data needed to be filtered in order to account for: 1) Different locations, and 2) external issues. First, while the simulation was set up using data from Portillo weather station located at 3000 m.a.s.l., the radiometer placed Nunatak laboratory at 2810 m.a.s.l and approximately 3 km to the west, and therefore, a lower accumulation is expected at Nunatak location. Second, when snow is shallow the laboratory structure can influence the snow, accelerating the snow melt around the laboratory, and therefore, influencing the radiometric data. In order to ensure that the measurements were performed on snow and not on bare ground, snow depth measured at Nunatak and Portillo stations were compared. After analysis, a 50 cm threshold was chosen, i.e. observational albedo values were considered only when snow depth at Portillo was

higher than 50 cm.

Different contamination scenarios were run to analyze the influence of increasing deposition rates. First, a clean snow scenario was run (e.i. no deposition rates) and considered as base line to compare with the contaminated snowpack. Then, BC and MD deposition rates were varied between 0 to 3 times the calibrated values. Results were analyzed in terms of maximum accumulation reduction (SWE_{max}), snow cover duration, albedo decrease, and induce radiative forcing, by comparing the clean snow scenario with and contaminated simulations. With the exception of snow cover duration, impacts of LAPs on the snowpack were analyzed for simulated snow depth greater that 0.1 m, to avoid comparison in shallow snowpacks where the underground surface influences the surface albedo.

3.4.6 Forcing variables

The model uses as input variables air temperature (T_{air}), relative humidity (RH), Precipitation (Pp), atmospheric pressure (P_{atm}), and wind speed (V_{wind}) (See Figure 3-2). It was calibrated using data from Portillo weather station, whenever it was available. Therefore, only T_{air} and RH were obtained from Portillo weather station. Missing T_{air} information was filled using monthly average temperature gradients, hourly estimated considering Portillo, Los Libertadores, and Juncal en Juncal stations. The same methodology was used to fill RH data gaps but through the dew-point temperature estimation using Clasius-Clapeyron equation. After filling the dew-point temperature time series, RH was calculated.

In the case of Pp, V_{wind}, and P_{atm}, no station nearby has collected a full series of such variables for the simulation period, and therefore other sources were considered. Daily Pp data was obtained from the CR2MET gridded products (Alvarez-Garreton et al., 2018), and hourly distributed. V_{wind} was estimated using statistical approach of Sanllehi (2023), derived from hourly data of the "*Explorador de Energía Eólica*" project (Muñoz et al., 2018). Finally, P_{atm} was extrapolated from measured at Quinta Normal, located in Santiago, using monthly temperature gradients obtained from daily temperature data (Sanllehi, 2023).

3.5 Results and discussion

3.5.1 Calibration and Validation

Evaluation metrics of the calibration results and cross-validation process are shown in Table 3.2, and Figure 3-3. For the calibration years, the model has shown a satisfactory performance. Specifically, the KGE values consistently show good results in all cases, with KGE values ranging between 0.932 and 0.955, and NSE values between 0.864 and 0.909. In the case of validation years, the model showed an acceptable performance for 2014, 2016, and 2019 ($KGE > 0.7$). However, this is not the case when considering years 2015, 2017, and 2018 for validation, showing issues to simulate the mean accumulation. For 2015, the KGE value drops to 0.284, with a significant discrepancy during observed in the β value, increasing up to 1.71. This means that the model is overestimating the mean accumulation by 71% when considering 2015 as the validation year. Is worth noting that this was the year with the highest maximum accumulation (SWE_{max}) measured. On the contrary, when considering 2017 or 2018, KGE values also drop to 0.534 and 0.642, respectively, but with a decrease in β values to 0.536 and 0.644, respectively. Lastly, concerning the parameters correlation (r) and variability (γ) coefficients, there doesn't seem to be significant variation, independent of the validation year considered.

Table 3.2: Cross validation metrics.

	2014 cal - val	2015 cal - val	2016 cal - val	2017 cal - val	2018 cal - val	2019 cal - val
KGE	0.951 - 0.707	0.951 - 0.284	0.932 - 0.707	0.955 - 0.534	0.943 - 0.642	0.943 - 0.722
r	0.952 - 0.950	0.951 - 0.942	0.933 - 0.914	0.955 - 0.983	0.943 - 0.987	0.944 - 0.878
β	0.996 - 0.757	0.996 - 1.710	0.997 - 1.196	1.000 - 0.536	0.997 - 0.644	0.994 - 0.761
γ	1.008 - 0.845	0.998 - 0.926	1.012 - 0.799	1.003 - 0.956	1.007 - 1.040	1.005 - 0.928
NSE	0.904 - 0.779	0.902 - 0.234	0.864 - 0.817	0.909 - 0.667	0.886 - 0.831	0.887 - 0.730

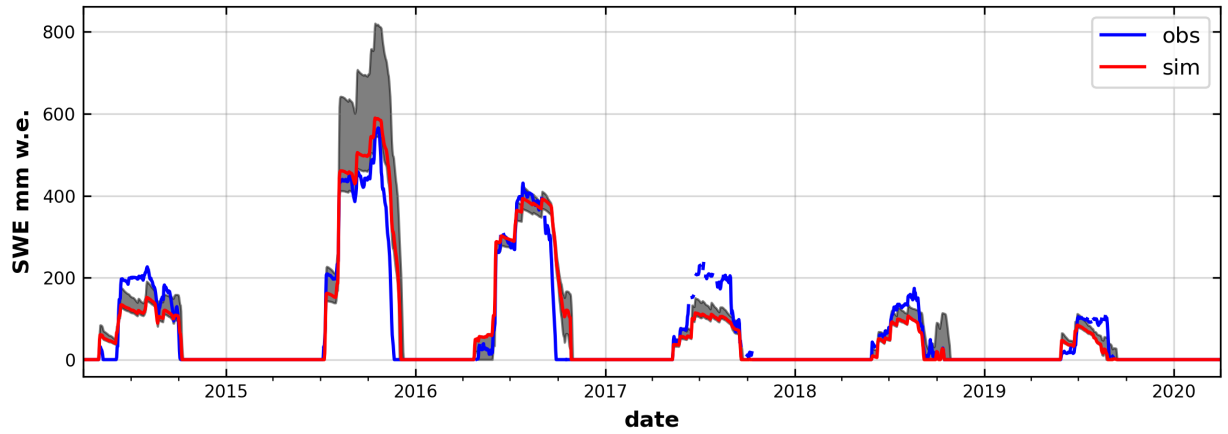

Figure 3-3: SWE measured values (blue) and simulated values (red) considering a set of parameters comprised by the wise-mean of each cross-validation procedure. Shaded area represents a range of simulations considering the optimal parameters of each validation step.

These outcomes show that the selection of the calibration and validation period can influence the model performance, thus, the snow accumulation simulated. When analyzing the model's behavior based on the year's snow accumulation, certain patterns can be distinct. When considering years with a high annual accumulation, such as 2015 or 2016, for the validation process, the model tends to overestimate, with a β value greater than 1.2. Conversely, when considering years with lower annual accumulations, the model tends to underestimate ($\beta < 0.85$). Such behavior is also seen when examining simulated (SWE_{max}) values. In general, it can be observed that higher SWE_{max} values are reached when considering years with higher snow accumulation for validation, particularly 2015.

When analyzing the parameters calibration results (Figures B-1 and B-2), the model shows that the most sensitive parameter is the precipitation scaling factor (F_{MO}). As discussed by Alvarez-Garreton et al. (2018), CR2MET products tend to systematically underestimate the magnitude of the precipitation, due to a limitation of satellite-derived precipitation when results in complex topography of headwater catchments are analyzed. Ayala et al. (2020) observed the same behavior while implementing a glacio-hydrological model, and a 50% correction factor was estimated to match the simulated and measured accumulation, Here, optimal values estimated through the cross-validation procedure, are in agreement with the correction factor estimated by Ayala et al. (2020). However, when considering 2015 as the validation year, F_{MO} rises up to a value of 2.3. Since 2015 was the year with the highest accumulation among the simulated, and all other years show significantly less

snow accumulation, ignoring 2015 for calibration seems to produce higher F_{MO} values because the model does not have this upper bound that limits results.

Similar behavior was observed for other parameters less sensitive, such as the surface aerodynamic roughness (z_0), Surface Conductance (K_s), and snow density ρ_{snow}. Optimal values tend to a similar optimal region, with the exception of the validation considering the year 2015. Additionally, the model showed less sensitivity while analyzing BC and MD dry deposition rates ($D_{BC,dry}$ and $D_{MD,wet}$ respectively), and therefore a wide range of optimal values were estimated. However, this do not imply that the impacts of BC and MD deposition onto snow surface are less important, but their impacts can not be evaluated from the model's general performance. These impacts are discussed in the following sections.

3.5.2 LAPs impacts

3.5.2.1 Concentration

Figure 3-4 shows the daily evolution of the BC and MD concentration onto snow surface simulated by the model, considering optimal parameters. Hereinafter, when referring to optimal parameters it means a set of parameters comprised by the wise-mean of each cross-validation procedure. Initially, is possible to observe that the model was capable to simulate the accumulation of LAPs on the surface. Simultaneously, shows the emergence of dirty layers embedded deeper when snowmelt occurs, which is consistent with a progressive LAPs accumulation (Skiles et al., 2019).

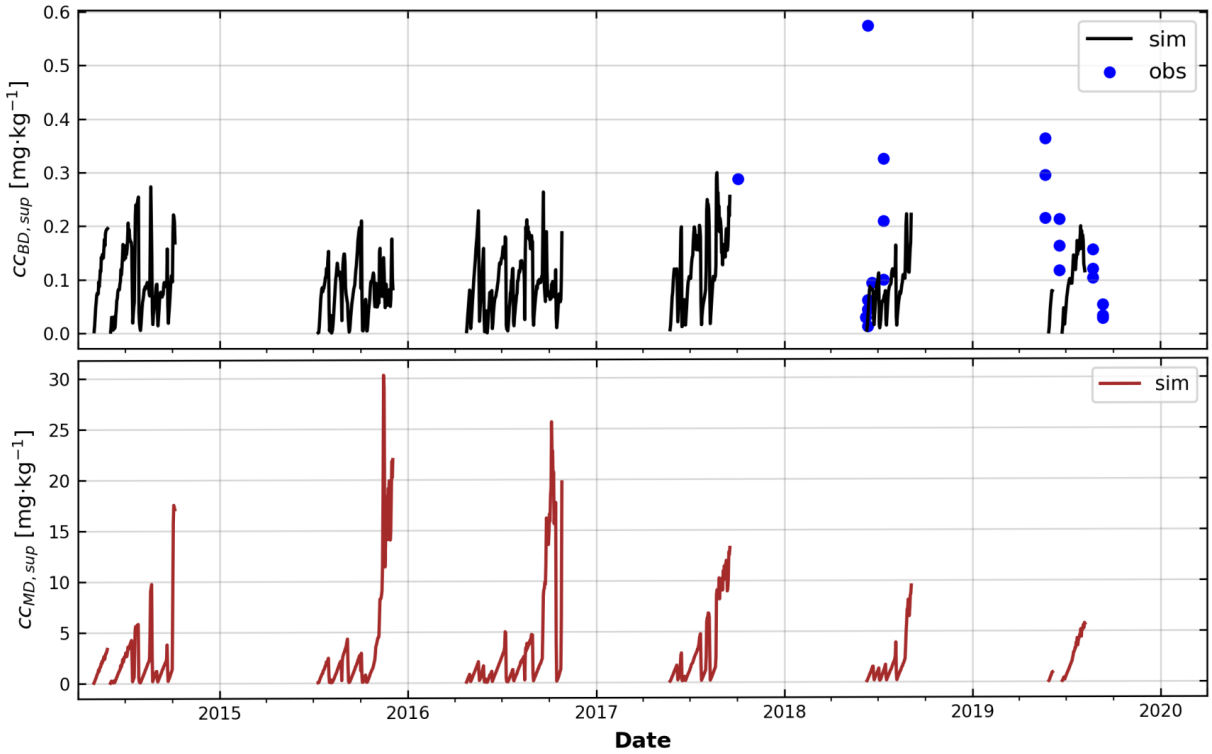

Figure 3-4: Superficial BC (top) and MD (bottom) concentration onto snow. Blue dots indicate measured BC concentration from surface snow samples collected near Nunatak station. Details of the sampling and analysis procedures are given by Cereceda-Balic et al. (2019).

Simulated daily BC concentrations onto snow surface ranged between nearly 0 to 0.30 $mg \cdot kg^{-1}$, with an average concentration of 0.10 $mg \cdot kg^{-1}$. These concentration values onto snow are within the magnitude order of the samples collected around Nunatak station, approximately 200 m away from the route. At this proximity deposition particle deposition onto snow can be directly influenced by advection, but also the diffusion of particle matter emitted from the route (González-Correa et al., 2023). It is worth mentioning that our simulated average results are one order of magnitude higher than the findings of Cordero, Sepúlveda, Feron, Wang, et al. (2022) and Rowe et al. (2019) at Portillo (but at a less exposed site) (between 0.003 and 0.02$mg \cdot kg^{-1}$), but agrees with the upper bound of BC concentration onto snow found in La Parva and Valle Nevado ski resorts in those studies (> 0.1 $mg \cdot kg^{-1}$).

Regarding MD concentration simulated values onto snow surface, they ranged between 0 and 30.3 $mg \cdot kg^{-1}$ with a mean MD concentration of 3.1 $mg \cdot kg^{-1}$. Even when no MD concentration measurements are available for the analyzed period, it is possible that the model is underestimating MD concentrations. Results are lower than MD concentrations found by Cereceda-Balic et al. (2022) at Olivares Alpha glacier and natural snow measurements from El Yeso dam showed in Chapter 2.

3.5.2.2 Albedo, RF, and Snow Water Equivalent

Figure 3-5 shows the comparison between measured and simulated broadband albedo values. A good correlation between simulated and measured albedo values ($r = 0.688$) was observed. And, on the contrary, it underestimates the variability ($\gamma = 0.45$) and the range values of the snow surface albedo. When examining both the measured and simulated values concurrently, the average albedo was slightly overestimated with a β of 1.04.

To assess the impacts of LAPs on the snowpack dynamics, a simulation free of LAPs was performed, e.i. BC and MD dry and wet deposition rates are set to zero. Results show that albedo difference due LAPs incorporation into the model varies depending on the year, with yearly mean values of daily albedo reduction ranging between 0.011 in 2018, and 0.023 in 2017 (Figure 3-6). Maximum differences were observed at the end of the season, with albedo reduction higher than 0.1 were observed in 2016. This albedo reduction is on average 2.1% lower than the clean scenario, with maximum values over 15% at the end of the season Induces mean daily values of instantaneous radiative forcing that can rise up to between 8.9 to 26.2 $W \cdot m^{-2}$, at the end of the snow seasons 2018 and 2016, respectively. On average instantaneous radiative forcing varies between 1.4 and 3.1 $W \cdot m^{-2}$ depending on the year. Both, albedo reduction and radiative forcing increase at the end of the season are consistent with a snowpack surface that has suffered a longer exposure time to the atmosphere.

Differences in maximum accumulation (SWE_{max}) and snowpack duration (SD) were observed while comparing clean and contaminated simulations. Small differences were observed in SWE_{max} values, with a maximum of 5.7 mmw.e, and a maximum shortening of up to 3 days in the SD. Is worth noting that these small differences in SWE_{max} are not directly related to the SD. For example, the maximum value of ΔSWE_{max} was observed in 2015, but for the same year nearly no difference was observed in SD. Additionally, model results show that the particle deposition is affecting melting rates.

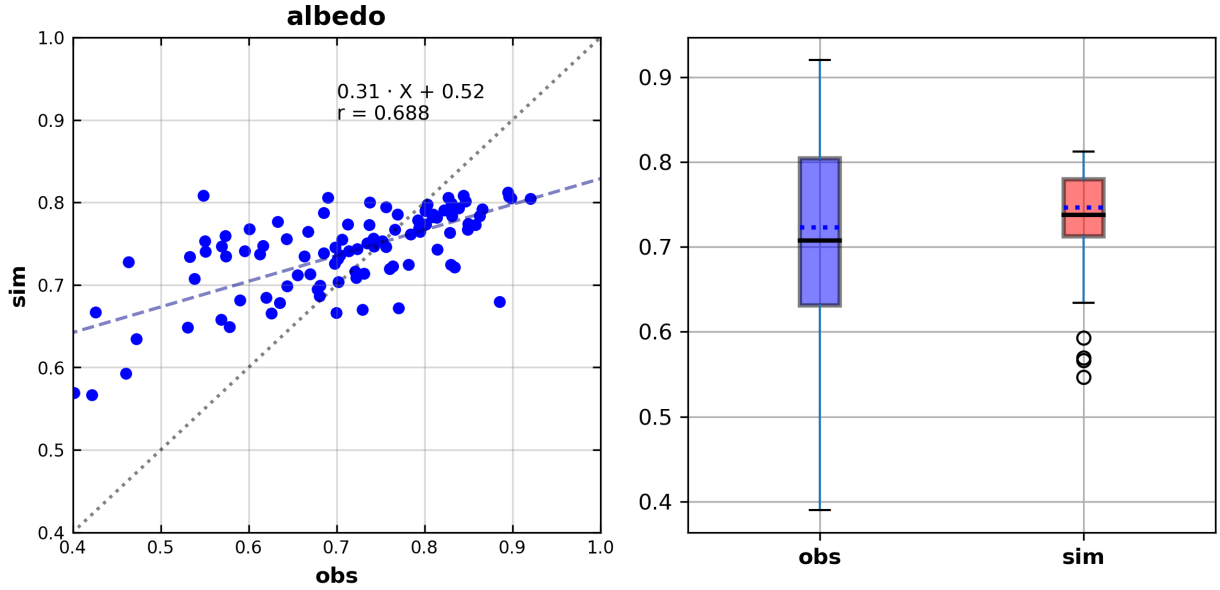

Figure 3-5: Comparative scatter plot (left) and boxplot (right) of measured (obs) and simulated (sim) broadband albedo.

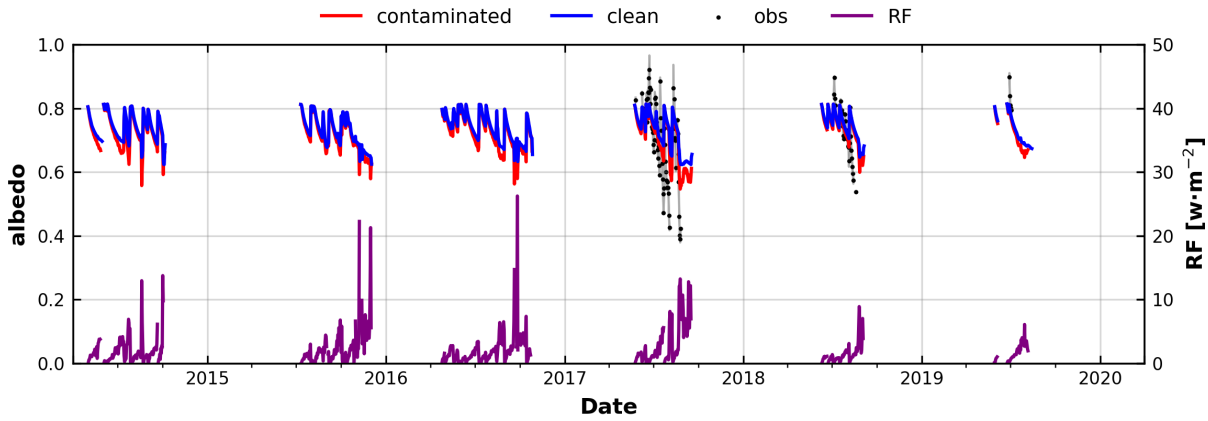

Figure 3-6: Time series of measured and simulated broadband albedo, and modeled radiative forcing. Red line represents calibrated model named "contaminated" and the blue line represents free of LAPs model named "clean".

Table 3.3: Difference in maximum accumulation and snowpack duration between clean and contaminated scenario.

year	ΔSWE_{max} mmw.e	ΔSD day
2014	3.1	0
2015	5.7	0
2016	2.0	1
2017	0.3	3
2018	1.9	3
2019	0.4	1

In terms of albedo decrease and radiative forcing, yearly average results seem to agree with estimations from experimental surveys in La Parva and Valle Nevado at the Central Andes (Cordero, Sepúlveda, Feron, Wang, et al., 2022; Rowe et al., 2019). However, our estimations show a wider variability with maximum values of daily average radiative forcing more than 2 times to those determined by such studies, which is basically explained by the large decreases in surface albedo observed at the of the season. Those previous studies had collected snow samples at the beginning of the snowmelt season, while ours considers the whole period. Nevertheless, results show that the radiative forcing induced by BC and MD onto the seasonal snowpack is far lower from those reported at heavily polluted areas around Central Asia (between 117 and 196 $\mathrm{W \cdot m^{-2}}$) (Li et al., 2020), but agree with estimations from the Northern Xinjiang, China (between 0.7 and 28.6 $\mathrm{W \cdot m^{-2}}$) (Zhong et al., 2019).

3.5.2.3 Case analysis

To analyze the sensitivity of the model to changes in the average deposition rates, cases with different contamination scenarios were run, varying calibrated BC dry and wet deposition rates ($7.7\text{x}10^{-10}$ and $1\text{x}10^{-9}$ $\mathrm{g \cdot m^{-2} \cdot s^{-1}}$, respectively), and MD deposition rates ($5.7\text{x}10^{-9}$ and $1\text{x}10^{-8}$ $\mathrm{g \cdot m^{-2} \cdot s^{-1}}$, respectively), between 0 and up to 3 times the calibrated values (see Table 3.4). Additionally, each case was run considering BC or MD deposition to estimate the impact of both types of particles separately.

Table 3.4: Cases for analysis.

year	$D_{BC,dry}$ and $D_{BC,wet}$	$D_{MD,dry}$ and $D_{MD,wet}$
1	x0	x0
2	x0.5	x0.5
3	x1	x1
4	x2	x2
5	x3	x3

Figures 3-7 and B-3 summarize the results of the simulations performed in for the case analysis. In general, results show that the MD concentrations accumulated onto snow surface are low to produce a significant impact on the seasonal snowpack, and the impacts are considerably low against BC's. Even when MD concentrations can be up to 2 magnitude orders higher than BC concentrations, MD particles have a low absorbance capacity compared to BC particles (González-Correa, Lapuerta, et

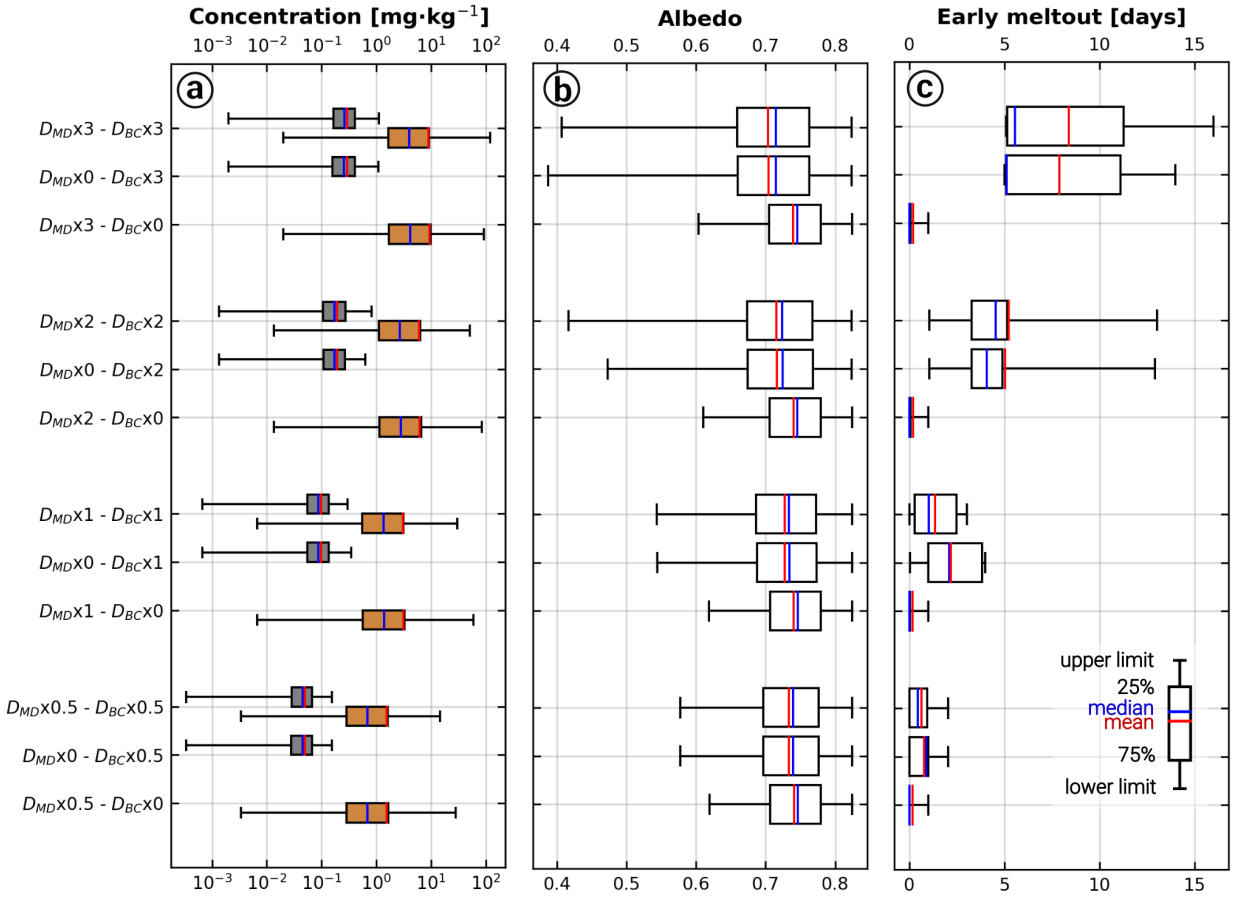

Figure 3-7: (a) Daily mean BC and MD concentrations onto snow surface according to the deposition rate, and their effects on (b) broadband albedo reduction, and (c) Days of early meltout. Gray and brown boxes indicate BC and MD concentrations.

al., 2022), and therefore, their impact is less significant. For all cases, the model showed MD particles can only reduce the snow duration in no more than 1 day, with a maximum albedo decrease of 0.001 for case 5 and, and an average decrease of less than 1 mmw.e. of the SWE_{max}. On the contrary, only BC simulations show that snow duration can reduce on average 7 days the snowpack duration in most contaminated cases, with a maximum albedo decrease of 0.038, and an average decrease up to 20 mmw.e. of the SWE_{max}. Simultaneously, only MD simulations showed a mean induced radiative forcing of less than 0.16 $\mathrm{W \cdot m^{-2}}$, with a maximum of 3.2 $\mathrm{W \cdot m^{-2}}$ for most contaminated cases, while in only MD simulations mean radiative forcing can reach up to 5.6 $\mathrm{W \cdot m^{-2}}$ with maximums of 47 $\mathrm{W \cdot m^{-2}}$ This means that, on average, BC particles induce an additional energy input of 35 times higher than BC.

These results agree with previous studies that have concluded that BC particles deposited onto snow should play a significant role in albedo reduction Central Andes (Cereceda-Balic et al., 2018), even more than MD particles (Rowe et al., 2019). It is worth mentioning that studies that have reported a significant impact of MD, have also measured maximum MD concentrations higher than 10^3 $\mathrm{g \cdot kgm^{-1}}$. For example, Skiles et al. (2019) estimated a 30 days early meltout in Senator Beck Basin Study Area, San Juan Mountains, USA, with measured MD concentrations over 6000

$g \cdot kgm^{-1}$. In the same line, Réveillet et al. (2022) estimated that the combined effect of BC and MD particles led to a reduction in snowpack duration of up to 17 and 16 days in the French Alps and Pyrenees, respectively. However, comparing the results of Chapters 1 and 2 absorption of Haze from Saharan outbreak in Europe with Andean MD, respectively, the latter has a Mass-specific Absorption Cross-section (MAC) of more than one order lower compared to haze. This implies that the effects of andean MD over the snowpack dynamics are lower too.

For detailed analysis, daily broadband albedo and SWE for the year 2017 are shown in Figure 3-8. Results show that increasing the LAPs deposition rates induces an albedo reduction across the whole season, which is more noticeable after a longer period of the surface. After each snowfall, albedo values reach a maximum > 0.8, but when snowmelt occurs, the model shows that more contaminated underlying layers were exposed to the atmosphere provoking drastic reductions of the albedo. This is what happened during the first and third week of August. In the latter period, albedo reduction can vary between 0.05 and 0.2, for cases 2 and 6, respectively. On the other hand, SWE time series shows that even when albedo variations are noticeable since the beginning of the season, the effect on snow accumulation is significant only at the end of the season. This is explained because this period is when shortwave radiation flux is higher, and melting becomes

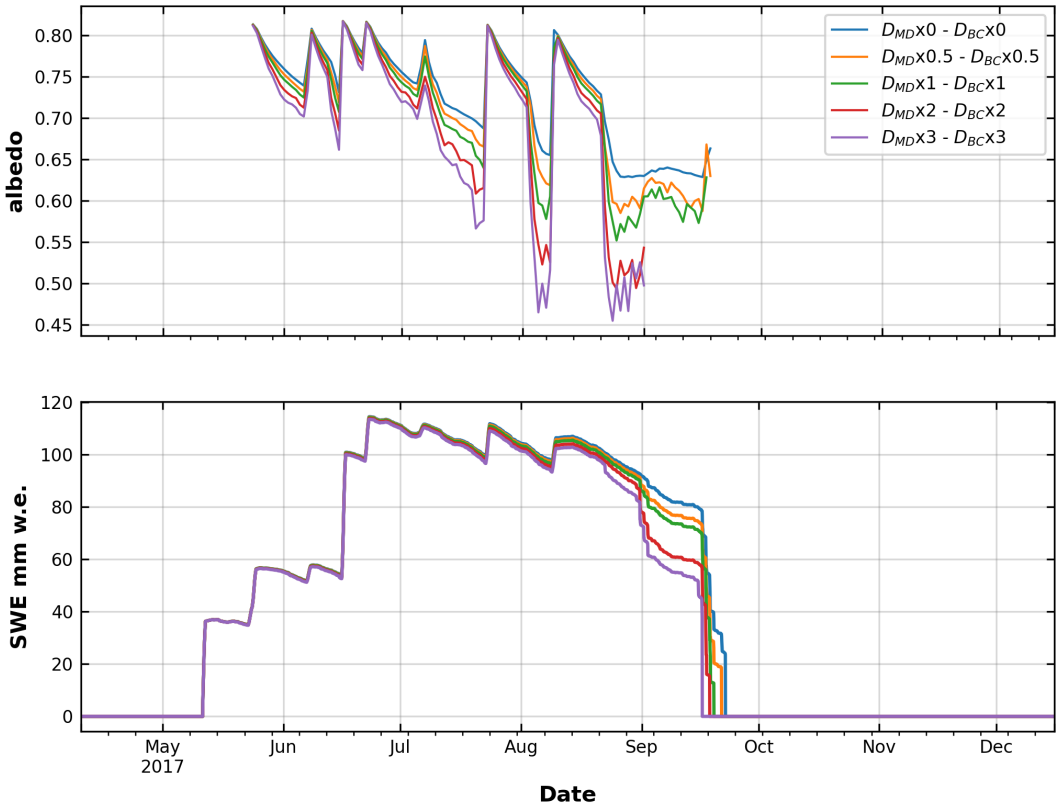

Figure 3-8: Time series of simulated broadband albedo and SWE for the year 2017 depending on the BC deposition rate case.

the most significant ablation process for the snowpack. This directly impacts the SD, inducing an early meltout of 1 day for the lowest BC contaminated case (2), and can reach up to 6 days when considering the most contaminated (case 5). It is worth mentioning that albedo simulated values for most contaminated at the end of the season are not shown, since an unusual increase was observed due to the layers handling method.

This behavior is similar in all years of simulation. In Tables B.4 and B.5 show a summary of the yearly snowpack duration (SD) shortening and the yearly average of daily albedo reduction depending on the deposition rate. Results show that snow melt-out can be generally reached up to 6 days earlier compared to a case with no BC accumulation onto snow surface. Is worth noting that in some most contaminated cases of 2016 and 2019, a maximum shortening of more than 13 days was reached. However, they need to be carefully analyzed, since they represent very high shortening that must be also related to the energy state of the model. Since an early melt-out was reached, the model simulates higher temperatures at the surface, and therefore, was not capable to simulate the accumulation of snow after the last snowfall of the year.

Even when simulation shows acceptable evaluation metrics, and the range of possible values chosen is based upon the observed and modeled values of deposition rate (Barrett et al., 2019; Cerqueira et al., 2010; Dumont et al., 2020; Ménégoz et al., 2014; Rowe et al., 2019), is arguable if the inclusion of a constant deposition rate can represent the LAPs accumulation behavior on a long time scale, or even further to represent a general behavior of the basin. LAP's deposition depends on the meteorological condition that drives the transport, such as wind speed and direction, as well as the emission load (Cereceda-Balic et al., 2018). The latter is particularly important for the case of Portillo, where the BC emissions are mostly related to vehicular traffic, and therefore intensity can vary depending on the route conditions (Cereceda-Balic et al., 2018). However, the inclusion of average LAPs deposition rates, with an empirical formulation to simulate their accumulation, seems to be an acceptable solution in order to test the ability of both models, UEB snow model and OptiPar radiative transfer model, to simulate LAPs impacts onto snow cover. Further development should include variability on deposition rates based, for example, on satellite imagery or directly measured data.

Additionally, there is uncertainty in the results of the simulated grain size evolution. Here, an empirical approach was applied using measured grain size growth rates to represent the snow metamorphism onto snow cover (Skiles & Painter, 2017). This enables the model to simulate a progressive increment on the snow grain size, avoiding assuming a constant value depending on the time since the last snowfall (Li et al., 2020; Rowe et al., 2019) An example of the near-surface grain size of year 2015 is shown in Figure B-4, An increasing trend is observed through the season, dropping to minimum values of 100 μm when a snowfall occurs, and reaching up to over 1200 μm of grain size at the end of the season. Nonetheless, this approach simplifies the metamorphism process, and it does not simulate important sub-processes, such as vapor diffusion, melt-refreeze cycles, and pressure, which are essential to understand the morphology evolution of grains (DeWalle et al., 2008), and thus, the effects onto snow surface albedo (Dang et al., 2016).

3.6 Conclusions

The coupled model showed a good performance in calibration stages and an acceptable performance for validation periods. However, analysis of the calibration strategy showed that the selection of the calibration-validation period can influence the optimal parameters. Here, when considering years with the highest measured SWE for the validation process, evaluation showed that the model tends to overestimate the mean accumulation, and on the contrary, tends to underestimate when considering years with low accumulation for validation. Parameter analysis shows that this behavior must be partially controlled by the inclusion of the precipitation scaling factors, which can reach up to higher values (> 2) when years with higher accumulation are used for cross-validation, and therefore the model does not have this upper bound that limits results. Finally, albedo simulation shows a good agreement with Nunatak's data in terms of correlation, but it neglects variability.

From the results of the present work, it is possible to conclude that small concentrations of LAPs, BC and MD, onto snow surface can alter the seasonal snowpack of Portillo. The model showed that broadband albedo reductions and instantaneous radiative forcing due to LAPs inclusion increase across the season. With the mean daily superficial concentration of BC and MD of 0.1 and 2.9 $\mathrm{mg} \cdot \mathrm{kg}^{-1}$, respectively, average reductions of daily broadband albedo varied between 0.011 and 0.023 depending on the year. This accounts for a mean albedo reduction of 2.1% relative to the clean scenario, with maximum values over 15% at the end of the season. Simultaneously, mean instantaneous radiative forcing varies between 1.4 and 3.1 $\mathrm{W} \cdot \mathrm{m}^{-2}$depending on the year, for the same concentrations.

Results show that the potential impact of BC and MD particles onto the snowpack not only affects snow optical properties, but also the water resources supply. The maximum accumulation of snow can be reduced by up to 5.7 mm, with a maximum of 3 days in reduction of the snowpack duration. Furthermore, increasing deposition rates up to 3 times the calibrated parameter can accelerate snowpack melt-out in average up to 7 days. Such results are mostly attributable to BC concentration onto snow surface, since the relatively higher absorption capacity compared to MD, and the low MD concentration simulated. This modeling study shows the significant effects of BC and MD emissions near snow covered areas. Consequently, regulation focused on reducing emissions around natural snowy areas would have a positive impact on the conservation of water resources.

Chapter 4

Final Remarks

The previous research offer insights into the complexities of Light Absorbing Particles (LAPs) and their impacts on snow surfaces Using an experimental and modeling approach this work delve into the LAPs impacts onto seasonal snow, and particularly in the context of snow albedo reduction, and consequentially, the snowpack duration.

The first and second studies show the importance of the particle composition on their impacts onto snow surface albedo, throughout different experiments of artificial contamination of snow. Not all particles equally affect the snow surface albedo. For instance, soot agglomerates has the most pronounced influence in reducing the albedo in the UV-VIS spectrum, while, sand's influence was observed to be compensated, i.e. reducing the albedo in the UV-VIS range but increasing it in the NIR wavelength range. With this in mind, we studied the mineral dust (MD) contamination in context of the Central Andes. Results show that high MD concentrations onto snow surface are require to provoke significant reductions in the snow albedo, and they primarily manifest in the UV and VIS spectrum, with a non-linear behavior that limit the broadband albedo decrease with increasing MD concentration. Although simulations performed with OptiPar radiative transfer model closely agree with experimental results, some discrepancies existed. These could be attributed to experimental factors, such as non-uniform distribution of concentration in snow, but also to LAPs optical properties estimation, and particularly the complex refractive index.

Furthermore, MD particles optical properties are highly variable because, in one side minerals can change with the emission source, and on the other, emission and deposition processes are diverse. Although effective medium models can provide good estimation of LAPs properties, extensive characterization of the particular minerals that comprise MD aerosls is needed. For example, this study we delve into one possible type of MD, encountering variations with in their volumetric composition, and no estimation of the complex refractive index of some of the constituent minerals, like amphibole, and chlorites. Focusing on the specific context of the Central Andes this is particularly important, due to the unique geological characteristics and the industrial activities that take place in high mountains near to snow or glaciers, like open pit mining. In the case of glaciers surrounding copper mines, they can be directly impacted by the emissions from excavations. Within them, specific minerals can be found, such as mentioned in the study by Barandun et al. (2022) in the Olivares glaciers. Therefore, further work is possible into the characterization of this constituent mineral to better estimate their impacts.

In the final study, the previous characterization of BC and MD particles were used as input to

run OptiPar radiative transfer model coupled with the Utha Energy Balance snow model, and to simulate snowpack accumulation and melting from 2014-2019 in the Juncal River Basin, Chile. The methodology used made possible to asses the significant impacts that small LAP concentrations can induce in broadband albedo and radiative forcing. Here, BC particles deposited onto snow surface exhibite a more significant compared to MD particles. But the impacts are not just optical; they also affect water resource supply, since increasing LAP concentrations onto snow can accelerate the melt-out of snowpacks by days. Such results highlight the critical implications of human-induced emissions, particularly BC, on snow-covered regions.

Nevertheless, certain aspects of the snow modeling approach require further development. While the UEB is a parsimonious model, meaning it minimize parameterization, it lacks of a simulation of the temperature gradient in depth, because the UEB does not operate on a multi-layered resolution scheme but rather on a single layer. This aspect is crucial, and if included it can allow for a better representation of snow crystal metamorphism processes, or the LAPs accumulation on the snow layers. On the other hand, the model was setup to run for a specific location within the basin, which doesn't necessarily extrapolate to a generalized behavior at basin scale. However, addressing this limitation requires more than a direct model application. Among other things, it requires for adequate simulation, whether of particle deposition or concentration on the snow surface. Such data can be provided by satellite product, but in most cases spatial resolution can be coarse relative to the the complex topography of the region, or LAPs concentrations too low for precise quantification. Consequently, there remains significant scope for for further development this topic.

In summary, the studies collectively highlight the effects of interactions between LAPs and snow. It becomes evident that while LAPs like BC and MD may differ in their optical characteristics, their cumulative effect on snow albedo and consequential hydrological implications cannot be understated. The complex interactions between anthropogenic factors, particle characteristics, and environmental conditions, requires not only to delve deeper into these dynamics but also elaborate strategies for the conservation of vital ecosystems, like the andean chryosphere.

Bibliography

Ajalloeian, R., Yu, H. S., & Allman, M. A. (1996). Physical and Mechanical Properties of Stockton Beach Sand. *7th Australia - New Zealand Conference on Geomechanics*, (July), 1–5.

Alvarez-Garreton, C., Mendoza, P. A., Pablo Boisier, J., Addor, N., Galleguillos, M., Zambrano-Bigiarini, M., Lara, A., Puelma, C., Cortes, G., Garreaud, R., McPhee, J., & Ayala, A. (2018). The CAMELS-CL dataset: Catchment attributes and meteorology for large sample studies-Chile dataset. *Hydrology and Earth System Sciences*, *22*(11). https://doi.org/10.5194/hess-22-5817-2018

Ayala, Á., Farías-Barahona, D., Huss, M., Pellicciotti, F., McPhee, J., & Farinotti, D. (2020). Glacier runoff variations since 1955 in the Maipo River Basin, semiarid Andes of central Chile. *The Cryosphere Discussions*, 1–39. https://doi.org/10.5194/tc-2019-233

Balkanski, Y., Schulz, M., Claquin, T., & Guibert, S. (2007). Reevaluation of Mineral aerosol radiative forcings suggests a better agreement with satellite and AERONET data. *Atmospheric Chemistry and Physics*, (2001), 81–95. https://doi.org/https://doi.org/10.5194/acp-7-81-2007

Ball, J. G. C., Reed, B. E., Grainger, R. G., Peters, D. M., Mather, T. A., & Pyle, D. M. (2015). Measurements of the complex refractive index of volcanic ash at 450 , 546 . 7 , and 650 nm. *Journal of Geophysical Research: Atmospheres*, *120*, 7747–7757. https://doi.org/10.1002/2015JD023521.Received

Barandun, M., Bravo, C., Grobety, B., Jenk, T., Fang, L., Naegeli, K., Rivera, A., Cisternas, S., Münster, T., & Schwikowski, M. (2022). Anthropogenic influence on surface changes at the Olivares glaciers; Central Chile. *Science of the Total Environment*, *833*(April). https://doi.org/10.1016/j.scitotenv.2022.155068

Barrett, T. E., Ponette-González, A. G., Rindy, J. E., & Weathers, K. C. (2019). *Wet deposition of black carbon: A synthesis* (Vol. 213). Elsevier Ltd. https://doi.org/10.1016/j.atmosenv.2019.06.033

Basart, S., Nickovic, S., Terradellas, E., Cuevas, E., García-pando, C. P., Werner, E., & Benincasa, F. (2019). The WMO SDS-WAS Regional Center for Northern Africa , Middle East and Europe. *E3S Web Conf.*, *99*, 1–4. https://doi.org/10.1051/e3sconf/20199904008

Belenkov, E. A. (2001). Formation of Graphite Structure in Carbon Crystallites. *Inorganic Materials*, *37*(9), 928–934.

Beres, N. D., & Moosmüller, H. (2018). Apparatus for dry deposition of aerosols on snow. *Atmospheric Measurement Techniques*, *11*(12), 6803–6813. https://doi.org/10.5194/amt-11-6803-2018

Beres, N. D., Sengupta, D., Samburova, V., Khlystov, A. Y., & Moosmüller, H. (2020). Deposition of brown carbon onto snow: Changes in snow optical and radiative properties. *Atmospheric Chemistry and Physics*, *20*, 6095–6114. https://doi.org/10.5194/acp-20-6095-2020

Bertalmío, M., Bertozzi, A. L., & Sapiro, G. (2001). Navier-Stokes, fluid dynamics, and image and video inpainting. *Proceedings of the IEEE Computer Society Conference on Computer Vision and Pattern Recognition*, *1*. https://doi.org/10.1109/cvpr.2001.990497

Bird, R. E., & Riordan, C. (1986). Simple Solar Spectral Model for Direct and Diffuse Irradiance on Horizontal and Tilted Planes at the Earth's Surface for Cloudless Atmospheres. *Journal of Applied Meteorology and Climatology*, *25*(1), 87–97. https://doi.org/https://doi.org/10.1175/1520-0450(1986)025<0087:SSSMFD>2.0.CO;2

Bond, T. C., Doherty, S. J., Fahey, D. W., Forster, P. M., Berntsen, T., Deangelo, B. J., Flanner, M. G., Ghan, S., Kärcher, B., Koch, D., Kinne, S., Kondo, Y., Quinn, P. K., Sarofim, M. C., Schultz, M. G., Schulz, M., Venkataraman, C., Zhang, H., Zhang, S., ... Zender, C. S. (2013). Bounding the role of black carbon in the climate system: A scientific assessment. *Journal of Geophysical Research Atmospheres*, *118*(11), 5380–5552. https://doi.org/10.1002/jgrd.50171

Bruggeman, D. A. G. (1937). Berechnung verschiedener physikalischer Konstanten von heterogenen Substanzen. III. Die elastischen Konstanten der quasiisotropen Mischkörper aus isotropen Substanzen. *Annalen der Physik*, *421*(2), 160–178. https://doi.org/https://doi.org/10.1002/andp.19374210205

Brun, E., David, P., Sudul, M., & Brunot, G. (1992). A numerical model to simulate snow-cover stratigraphy for operational avalanche forecasting. *Journal of Glaciology*, *38*(128), 13–22. https://doi.org/10.3189/s0022143000009552

Calingaert, G., Heron, S., & Stair, R. (1936). Sapphire and other new combustion-chamber window materials. *SAE Transactions*, 448–450.

Cereceda-Balic, F., Palomo-Marín, M. R., Bernalte, E., Vidal, V., Christie, J., Fadic, X., Guevara, J. L., Miro, C., & Pinilla Gil, E. (2012). Impact of Santiago de Chile urban atmospheric pollution on anthropogenic trace elements enrichment in snow precipitation at Cerro Colorado, Central Andes. *Atmospheric Environment*, *47*. https://doi.org/10.1016/j.atmosenv.2011.11.045

Cereceda-Balic, F., Gorena, T., Soto, C., Vidal, V., Lapuerta, M., & Moosmüller, H. (2019). Optical determination of black carbon mass concentrations in snow samples: A new analytical method. *Science of the Total Environment*, *697*, 133934. https://doi.org/10.1016/j.scitotenv.2019.133934

Cereceda-Balic, F., Ruggeri, M. F., Vidal, V., Ruiz, L., & Fu, J. S. (2022). Understanding the role of anthropogenic emissions in glaciers retreat in the central Andes of Chile. *Environmental Research*, *214*(P1), 113756. https://doi.org/10.1016/j.envres.2022.113756

Cereceda-Balic, F., Vidal, V., Moosmüller, H., & Lapuerta, M. (2018). Reduction of snow albedo from vehicle emissions at Portillo, Chile. *Cold Regions Science and Technology*, *146*(November 2017), 43–52. https://doi.org/10.1016/j.coldregions.2017.11.008

Cereceda-Balic, F., Vidal, V., Ruggeri, M. F., & González, H. E. (2020). Black carbon pollution in snow and its impact on albedo near the Chilean stations on the Antarctic peninsula: First results. *Science of the Total Environment*, *743*. https://doi.org/10.1016/j.scitotenv.2020.140801

Cerqueira, M., Pio, C., Legrand, M., Puxbaum, H., Kasper-Giebl, A., Afonso, J., Preunkert, S., Gelencsér, A., & Fialho, P. (2010). Particulate carbon in precipitation at European background sites. *Journal of Aerosol Science*, *41*(1), 51–61. https://doi.org/10.1016/j.jaerosci.2009.08.002

Chang, H., & Charalampopoulos, T. (1990). Determination of the wavelength dependence of refractive indices of flame soot. *Proceedings of the Royal Society of London. Series A: Mathematical and Physical Sciences*, *430*(1880), 577–591. https://doi.org/10.1098/rspa.1990.0107

Chen, A., Li, W., Li, W., & Liu, X. (2014). An observational study of snow aging and the seasonal variation of snow albedo by using data from Col de Porte, France. *Chinese Science Bulletin*, *59*(34), 4881–4889. https://doi.org/10.1007/s11434-014-0429-9

Clarke, A. D., & Noone, K. J. (1985). SOOT IN THE ARCTIC SNOWPACK : A CAUSE FOR PERTURBATIONS IN RADIATIVE TRANSFER. *Atmospheric Environment*, *19*(12), 2045–2053. https://doi.org/https://doi.org/10.1016/0004-6981(85)90113-1

Classic gems [Accessed on 8 October 2022]. (2022). http://www.classicgems.net/refractiveindex.htm#top

Clifton, A., Manes, C., Michele, J.-d. R., & Michael, G. (2008). On Shear-Driven Ventilation of Snow, 249–261. https://doi.org/10.1007/s10546-007-9235-0

Cogley, J., Hock, R., Rasmussen, L., Arendt, A., Bauder, A., Braithwaite, R., Jansson, P., Kaser, G., Möller, M., Nicholson, L., & Zemp, M. (2011). Glossary of glacier mass balance and related terms. https://doi.org/10.5167/uzh-53475

Constantin, J. G., Ruiz, L., Villarosa, G., Outes, V., Bajano, F. N., He, C., Bajano, H., & Dawidowski, L. (2020). Measurements and modeling of snow albedo at Alerce Glacier, Argentina: Effects of volcanic ash, snow grain size, and cloudiness. *Cryosphere*, *14*(12), 4581–4601. https://doi.org/10.5194/tc-14-4581-2020

Conway, H., Gades, A., & Raymond, C. F. (1996). Albedo of dirty snow during conditions of melt. *Water Resources Research*, *32*, 1713–1718. https://doi.org/10.1029/96WR00712

Copernicus Atmosphere Monitoring Service. (2022). Cams monitors transport of so2 from la palma volcano [Accessed on 7 October 2022]. https://atmosphere.copernicus.eu/cams-monitors-transport-so2-la-palma-volcano

Cordero, R. R., Sepúlveda, E., Feron, S., Damiani, A., Fernandoy, F., Neshyba, S., Rowe, P. M., Asencio, V., Carrasco, J., Alfonso, J. A., Llanillo, P., Wachter, P., Seckmeyer, G., Stepanova, M., Carrera, J. M., Jorquera, J., Wang, C., Malhotra, A., Dana, J., ... Casassa, G. (2022). Black carbon footprint of human presence in Antarctica. *Nature Communications*, *13*(1), 1–11. https://doi.org/10.1038/s41467-022-28560-w

Cordero, R. R., Sepúlveda, E., Feron, S., Wang, C., Damiani, A., Fernandoy, F., Neshyba, S., Rowe, P. M., Asencio, V., Carrasco, J., Alfonso, J. A., MacDonell, S., Seckmeyer, G., Carrera, J. M., Jorquera, J., Llanillo, P., Dana, J., Khan, A. L., & Casassa, G. (2022). Black carbon in the southern andean snowpack. *Environmental Research Letters*, *17*. https://doi.org/10.1088/1748-9326/ac5df0

Corripio, J. G. (2004). Snow surface albedo estimation using terrestrial photography. *International Journal of Remote Sensing*, *25*(24), 5705–5729. https://doi.org/10.1080/01431160410001709002

Dang, C., Brandt, R. E., & Warren, S. G. (2015). Parameterizations for narrowband and broadband albedo of pure snow and snow containing mineral dust and black carbon. *Cheng Dang, Richard E. Brandt, Stephen G. Warren*, *120*(11), 5446–5468. https://doi.org/10.1002/2014JD022646

Dang, C., Fu, Q., & Warren, S. G. (2016). Effect of snow grain shape on snow albedo. *Journal of the Atmospheric Sciences*, *73*(9), 3573–3583. https://doi.org/10.1175/JAS-D-15-0276.1

Deguine, A., Petitprez, D., Clarisse, L., Guđmundsson, S., Outes, V., Villarosa, G., & Herbin, H. (2020). Complex refractive index of volcanic ash aerosol in the infrared, visible, and ultraviolet. *Appl. Opt.*, *59*(4), 884–895. https://doi.org/10.1364/AO.59.000884

DeWalle, D. R., & Rango, A. (2008). *Principles of Snow Hydrology*.

Di Biagio, C., Boucher, H., Caquineau, S., Chevaillier, S., Cuesta, J., & Formenti, P. (2014). Variability of the infrared complex refractive index of African mineral dust: Experimental estimation

and implications for radiative transfer and satellite remote sensing. *Atmospheric Chemistry and Physics*, *14*(20), 11093–11116. https://doi.org/10.5194/acp-14-11093-2014

Dickinson, E., Henderson-Sellers, A., & Kennedy, J. (1993). Biosphere-atmosphere Transfer Scheme (BATS) Version 1e as Coupled to the NCAR Community Climate Model. *NCAR Tech. Rep. NCAR/TN-3871STR, 72*, (August), 77. https://opensky.ucar.edu/islandora/object/technotes%3A154/

Dozier, J., & Painter, T. H. (2004). Multispectral and hyperspectral remote sensing of alpine snow properties. *Annual Review of Earth and Planetary Sciences*, *32*, 465–494. https://doi.org/10.1146/annurev.earth.32.101802.120404

Duan, Q. Y., Gupta, V. K., & Sorooshian, S. (1993). Shuffled complex evolution approach for effective and efficient global minimization. *Journal of Optimization Theory and Applications*, *76*(3), 501–521. https://doi.org/10.1007/BF00939380

Dumont, M., Tuzet, F., Gascoin, S., Picard, G., Kutuzov, S., Lafaysse, M., Cluzet, B., Nheili, R., & Painter, T. H. (2020). Accelerated Snow Melt in the Russian Caucasus Mountains After the Saharan Dust Outbreak in March 2018. *Journal of Geophysical Research: Earth Surface*, *125*(9), 1–13. https://doi.org/10.1029/2020JF005641

Dumont, M., Arnaud, L., Picard, G., Libois, Q., Lejeune, Y., Nabat, P., Voisin, D., & Morin, S. (2017). In situ continuous visible and near-infrared spectroscopy of an alpine snowpack. *Cryosphere*, *11*(3), 1091–1110. https://doi.org/10.5194/tc-11-1091-2017

Dussaillant, I., Berthier, E., Brun, F., Masiokas, M. H., Hugonnet, R., Favier, V., Rabatel, A., Pitte, P., & Ruiz, L. (2019). Two decades of glacier mass loss along the Andes. *Nature Geoscience*, *12*(10), 802–808. https://doi.org/10.1038/s41561-019-0432-5

Egan, W. G., & Hilgeman, T. W. (1979). *Optical Properties of Inhomogeneous Materials: Applications to Geology, Astronomy, Chemistry, and Engineering*. Academic Press.

Fabian, D., Henning, T., Jäger, C., Mutschke, H., Dorschner, J., & Wehrhan, O. (2001). Steps toward interstellar silicate mineralogy. VI. Dependence of crystalline olivine IR spectra on iron content and particle shape., *378*, 228–238. https://doi.org/10.1051/0004-6361:20011196

Falvey, M., & Garreaud, R. D. (2007). Wintertime Precipitation Episodes in Central Chile: Associated Meteorological Conditions and Orographic Influences. *172 JOURNAL OF HYDROMETEOROLOGY*, *8*(1991), 171–193. https://doi.org/10.1175/JHM562.1

Fierz, C. (2009). *The International Classification for Seasonal Snow on the Ground.* (tech. rep. No. 83). UNESCO-IHP. Paris.

Flanner, M. G., Arnheim, J. B., Cook, J. M., Dang, C., He, C., Huang, X., Singh, D., Skiles, S. M. K., Whicker, C. A., & Zender, C. S. (2021). SNICAR-ADv3: A community tool for modeling spectral snow albedo. *Geoscientific Model Development*, *14*(12), 7673–7704. https://doi.org/10.5194/gmd-14-7673-2021

Flanner, M. G., Zender, C. S., Randerson, J. T., & Rasch, P. J. (2007). Present-day climate forcing and response from black carbon in snow. *Journal of Geophysical Research Atmospheres*, *112*(11), 1–17. https://doi.org/10.1029/2006JD008003

Formenti, P., Schutz, L., Balkanski, Y., Desboeufs, K., Ebert, M., Kandler, K., Petzold, A., Scheuvens, D., Weinbruch, S., & Zhang, D. (2011). Recent progress in understanding physical and chemical properties of African and Asian mineral dust. *Atmospheric Chemistry and Physics*, *11*, 8231–8256. https://doi.org/10.5194/acp-11-8231-2011

Garreaud, R. D., Alvarez-Garreton, C., Barichivich, J., Pablo Boisier, J., Christie, D., Galleguillos, M., LeQuesne, C., McPhee, J., & Zambrano-Bigiarini, M. (2017). The 2010-2015 megadrought in central Chile: Impacts on regional hydroclimate and vegetation. *Hydrology and Earth System Sciences*, *21*(12), 6307–6327. https://doi.org/10.5194/hess-21-6307-2017

Garreaud, R. D., Boisier, J. P., Rondanelli, R., Montecinos, A., & Veloso-aguila, H. H. S. D. (2020). The Central Chile Mega Drought (2010 – 2018): A climate dynamics perspective. (January 2019), 421–439. https://doi.org/10.1002/joc.6219

Ginot, P., Dumont, M., Lim, S., Patris, N., Taupin, J. D., Wagnon, P., Gilbert, A., Arnaud, Y., Marinoni, A., Bonasoni, P., & Laj, P. (2014). A 10 year record of black carbon and dust from a Mera Peak ice core (Nepal): Variability and potential impact on melting of Himalayan glaciers. *Cryosphere*, *8*(4), 1479–1496. https://doi.org/10.5194/tc-8-1479-2014

González-Correa, S., Gómez-Doménech, D., Ballesteros, R., Lapuerta, M., Pacheco-Ferrada, D., Flores, R. P., Castro, L., Fadic-Ruiz, X., & Cereceda-Balic, F. (2022). Impact of vehicle soot agglomerates on snow albedo. *Atmosphere*, *13(5)*, 1–12. https://doi.org/10.3390/atmos13050801

González-Correa, S., Lapuerta, M., Ballesteros, R., Pacheco-Ferrada, D., Castro, L., & Cereceda-Balic, F. (2022). Impacts of soot, ash, sand, and haze on snow albedo in sierra. *Atmosphere*, *13*, 1–15. https://doi.org/doi.org/10.3390/atmos13111903

González-Correa, S., Lapuerta, M., Pacheco-Ferrada, D., Castro, L., Ruggeri, M. F., & Cereceda-Balic, F. (2023). Field study on the diffusion and advection effects of vehicle-emitted soot aerosols on snow albedo in the chilean andes. *Atmospheric Environment*, 120136. https://doi.org/https://doi.org/10.1016/j.atmosenv.2023.120136

Gramsch, E., Muñoz, A., Langner, J., Morales, L., Soto, C., Pérez, P., & Rubio, M. A. (2020). Black carbon transport between Santiago de Chile and glaciers in the Andes Mountains. *Atmospheric Environment*, *232*(December 2019). https://doi.org/10.1016/j.atmosenv.2020.117546

Gupta, H. V., Kling, H., Yilmaz, K. K., & Martinez, G. F. (2009). Decomposition of the mean squared error and NSE performance criteria: Implications for improving hydrological modelling. *Journal of Hydrology*, *377*(1-2), 80–91. https://doi.org/10.1016/j.jhydrol.2009.08.003

Hadley, O. L., & Kirchstetter, T. W. (2012). Black-carbon reduction of snow albedo. *Nature Climate Change*, *2*(6), 437–440. https://doi.org/10.1038/nclimate1433

Instituto de Investigaciones Geológicas, I. (1980). *Carta geológica de chile. escala 1:250.000: Geología de la hoja santiago. región metropolitana*. Instituto de Investigaciones Geológicas.

Jacobi, H. W., Lim, S., Ménégoz, M., Ginot, P., Laj, P., Bonasoni, P., Stocchi, P., Marinoni, A., & Arnaud, Y. (2015). Black carbon in snow in the upper Himalayan Khumbu Valley, Nepal: Observations and modeling of the impact on snow albedo, melting, and radiative forcing. *Cryosphere*, *9*(4). https://doi.org/10.5194/tc-9-1685-2015

Jaenicke, R. (1980). Atmospheric aerosols and global climate. *Journal of Aerosol Science*, *11*(5), 577–588. https://doi.org/https://doi.org/10.1016/0021-8502(80)90131-7

Joseph, J. H., Wiscombe, W. J., & Weinman, J. A. (1976). The Delta-Eddington Approximation for Radiative Flux Transfer. *Journal of Atmospheric Sciences*, *33*(12), 2452–2459. https://doi.org/https://doi.org/10.1175/1520-0469(1976)033<2452:TDEAFR>2.0.CO;2

Kelesidis, G. A., Bruun, C. A., & Pratsinis, S. E. (2021). The impact of organic carbon on soot light absorption. *Carbon*, *172*, 742–749. https://doi.org/10.1016/j.carbon.2020.10.032

Kling, H., Fuchs, M., & Paulin, M. (2012). Runoff conditions in the upper Danube basin under an ensemble of climate change scenarios. *Journal of Hydrology*, *424-425*, 264–277. https://doi.org/10.1016/j.jhydrol.2012.01.011

Koepke, P., Hess, M., Schult, I., & Shettle, E. (1997). *Global aerosol data set* (Report No. 243). Max-Planck-Institut für Meteorologie. Hamburg.

Kok, J. F., Parteli, E. J. R., Michaels, T. I., & Karam, D. B. (2012). The physics of wind-blown sand and dust. https://doi.org/10.1088/0034-4885/75/10/106901

Kokhanovsky, A. A. (2021). Light penetration in snow layers. *Journal of Quantitative Spectroscopy and Radiative Transfer*, *278*, 108040. https://doi.org/10.1016/j.jqsrt.2021.108040

Kokhanovsky, A. A., & Zege, E. P. (2004). Scattering optics of snow. *Appl. Opt.*, *43*(7), 1589–1602. https://doi.org/10.1364/AO.43.001589

La Tribuna de Ciudad Real. (2022). La calima seguirá sobre ciudad real durante la semana [Accessed on 7 October 2022]. https://www.latribunadeciudadreal.es/Noticia/Z86ECDF15-CCF7-762A-ED3027336030186D/202203/La-calima-seguira-sobre-Ciudad-Real-durante-la-semana

Langlois, A., Royer, A., Montpetit, B., Roy, A., & Durocher, M. (2020). Presenting Snow Grain Size and Shape Distributions in Northern Canada Using a New Photographic Device Allowing 2D and 3D Representation of Snow Grains. *Frontiers in Earth Science*, *7*(January), 1–19. https://doi.org/10.3389/feart.2019.00347

Lapuerta, M., Ballesteros, R., & Martos, F. (2009). The effect of diesel engine conditions on the size and morphology of soot particles. *International Journal of Vehicle Design*, *50*(1-4), 91–106. https://doi.org/10.1504/IJVD.2009.024972

Lapuerta, M., Ballesteros, R., & Martos, F. J. (2006). A method to determine the fractal dimension of diesel soot agglomerates. *Journal of Colloid and Interface Science*, *303*, 149–158. https://doi.org/10.1016/j.jcis.2006.07.066

Lapuerta, M., González-Correa, S., Ballesteros, R., Moosmüller, H., & Cereceda-Balic, F. (2022). Albedo reduction for snow surfaces contaminated with soot aerosols: Comparison of experimental results and models. *Aerosol Science and Technology*. https://doi.org/10.1080/02786826.2022.2091975

Lapuerta, M., Oliva, F., Agudelo, J. R., & Boehman, A. L. (2012). Effect of fuel on the soot nanostructure and consequences on loading and regeneration of diesel particulate filters. *Combustion and Flame*, *159*, 844–853. https://doi.org/10.1016/j.combustflame.2011.09.003

Lawrence, C. R., Painter, T. H., Landry, C. C., & Neff, J. C. (2010). Contemporary geochemical composition and flux of aeolian dust to the San Juan Mountains , Colorado , United States. *115*, 1–15. https://doi.org/10.1029/2009JG001077

Le Bas, M., & Streckeisen, A. L. (1991). The iugs systematics of igneous rocks. *Journal of the Geological Society*, *148*(5), 825–833.

Li, X., Kang, S., Sprenger, M., Zhang, Y., He, X., Zhang, G., Tripathee, L., Li, C., & Cao, J. (2020). Black carbon and mineral dust on two glaciers on the central Tibetan Plateau: Sources and implications. *Journal of Glaciology*, *66*(256), 248–258. https://doi.org/10.1017/jog.2019.100

Linke, C., Möhler, O., Veres, A., Mohácsi, Á., Bozóki, Z., Szabó, G., & Schnaiter, M. (2006). Optical properties and mineralogical composition of different Saharan mineral dust samples: A laboratory study. *Atmospheric Chemistry and Physics*, *6*(11), 3315–3323. https://doi.org/10.5194/acp-6-3315-2006

Liu, F., Yon, J., & Bescond, A. (2016). On the radiative properties of soot aggregates – Part 2: Effects of coating. *Journal of Quantitative Spectroscopy and Radiative Transfer*, *172*, 134–145. https://doi.org/10.1016/j.jqsrt.2015.08.005

Longtin, D. R., Shettle, E. P., Hummel, J. R., & Pryce, J. D. (1988). A Wind Dependent Desert Aerosol Model: Radiative Properties. *United States air Force: Bedford, MA, USA*.

Macke, A., Mueller, J., & Raschke, E. (1996). Single Scattering Properties of Atmospheric Ice Crystals. *Journal of Atmospheric Sciences*, *53*(19), 2813–2825. https://doi.org/https://doi.org/10.1175/1520-0469(1996)053<2813:SSPOAI>2.0.CO;2

Malmros, J. K., Mernild, S. H., Wilson, R., Tagesson, T., & Fensholt, R. (2018). Snow cover and snow albedo changes in the central Andes of Chile and Argentina from daily MODIS observations

(2000–2016). *Remote Sensing of Environment*, *209*(February 2017), 240–252. https://doi.org/10.1016/j.rse.2018.02.072

Manninen, T., Anttila, K., Jääskeläinen, E., Riihelä, A., Peltoniemi, J., Räisänen, P., Lahtinen, P., Siljamo, N., Thölix, L., Meinander, O., Kontu, A., Suokanerva, H., Pirazzini, R., Suomalainen, J., Hakala, T., Kaasalainen, S., Kaartinen, H., Kukko, A., Hautecoeur, O., & Roujean, J. L. (2021). Effect of small-scale snow surface roughness on snow albedo and reflectance. *Cryosphere*, *15*(2), 793–820. https://doi.org/10.5194/tc-15-793-2021

Manninen, T., Anttila, K., Karjalainen, T., & Lahtinen, P. (2012). Automatic snow surface roughness estimation using digital photos. *Journal of Glaciology*, *58*(211), 993–1007. https://doi.org/10.3189/2012JoG11J144

Marcos, L. V. R.-d., Larruquert, J. I., Méndez, J. A., & Aznárez, J. A. (2016). Self-consistent optical constants of sio2 and ta2o5 films. *Opt. Mater. Express*, *6*(11), 3622–3637. https://doi.org/10.1364/OME.6.003622

Matzl, M., & Schneebeli, M. (2006). Measuring specific surface area of snow by near-infrared photography. *Journal of Glaciology*, *52*(179), 558–564. https://doi.org/10.3189/172756506781828412

Ménégoz, M., Krinner, G., Balkanski, Y., Boucher, O., Cozic, A., Lim, S., Ginot, P., Laj, P., Gallée, H., Wagnon, P., Marinoni, A., & Jacobi, H. W. (2014). Snow cover sensitivity to black carbon deposition in the Himalayas: From atmospheric and ice core measurements to regional climate simulations. *Atmospheric Chemistry and Physics*, *14*(8), 4237–4249. https://doi.org/10.5194/acp-14-4237-2014

Meteoblue. (2022). Archivo meteorológico estación de esquí de sierra nevada [Accessed on 8 October 2022]. https://www.meteoblue.com/es/tiempo/historyclimate/weatherarchive/estaci%C3%B3n-de-esqu%C3%AD-de-sierra-nevada_espa%C3%B1a_7602397

Migliavacca, F., Confortola, G., Soncini, A., Senese, A., Diolaiuti, G. A., Smiraglia, C., Barcaza, G., & Bocchiola, D. (2015). Hydrology and potential climate changes in the Rio Maipo (Chile). *Geografia Fisica e Dinamica Quaternaria*, *38*(2), 155–168. https://doi.org/10.4461/GFDQ.2015.38.14

Mohnen, V., Jaenicke, R., Delany, A. C., Zoller, W., & Rahn, K. (1983). The Atmospheric Aerosol System: An Overview. *21*(7), 1607–1629. https://doi.org/0034-6853/83/003R-0361$15.00

Moosmüller, H., Chakrabarty, R. K., & Arnott, W. P. (2009). Aerosol light absorption and its measurement: A review. *Journal of Quantitative Spectroscopy and Radiative Transfer*, *110*(11), 844–878. https://doi.org/10.1016/j.jqsrt.2009.02.035

Mountain, R. D., & Mulholland, G. W. (1988). Light Scattering from Simulated Smoke Agglomerates. (4), 1321–1326.

Muñoz, R. C., Falvey, M. J., Arancibia, M., Astudillo, V. I., Elgueta, J., Ibarra, M., Santana, C., & Vásquez, C. (2018). OVER THE ATACAMA DESERT A Numerical Model – Guided Observational Program. *Bulletin of the American Meteorological Society*, *99*(10), 2079–2092. https://doi.org/10.1175/BAMS-D-17-0019.1

Myhre, G., Shindell, D., Bréon, F.-M., Collins, W., Fuglestvedt, J., Huang, J., Koch, D., Lamarque, J.-F., Lee, D., Mendoza, B., Nakajima, T., Robock, A., Stephens, G., Takemura, T., & Zhang, H. (2013). Anthropogenic and natural radiative forcing. In T. Stocker, D. Qin, G.-K. Plattner, M. Tignor, S. Allen, J. Boschung, A. Nauels, Y. Xia, V. Bex, & P. Midgley (Eds.), *Climate change 2013: The physical science basis. contribution of working group i to the fifth assessment report of the intergovernmental panel on climate change* (p. 659). Cambridge University Press.

Niu, H., Kang, S., Shi, X., Paudyal, R., He, Y., Li, G., & Wang, S. (2017). Science of the Total Environment In-situ measurements of light-absorbing impurities in snow of glacier on Mt .

Yulong and implications for radiative forcing estimates. *Science of the Total Environment*, *581-582*, 848–856. https://doi.org/10.1016/j.scitotenv.2017.01.032

Nolin, A. W., & Dozier, J. (2000). A hyperspectral method for remotely sensing the grain size of snow. *Remote Sensing of Environment*, *74*(2), 207–216. https://doi.org/10.1016/S0034-4257(00)00111-5

Painter, T. H., Bryant, A. C., & Skiles, M. (2012). Radiative forcing by light absorbing impurities in snow from MODIS surface reflectance data. *Geophysical Research Letters*, *39*(17), 1–7. https://doi.org/10.1029/2012GL052457

Painter, T. H., Deems, J. S., Belnap, J., Hamlet, A. F., Landry, C. C., & Udall, B. (2010). Response of Colorado river runoff to dust radiative forcing in snow. *Proceedings of the National Academy of Sciences of the United States of America*, *107*(40), 17125–17130. https://doi.org/10.1073/pnas.0913139107

Painter, T. H., Skiles, S. M. K., Deems, J. S., Bryant, A. C., & Landry, C. C. (2012). Dust radiative forcing in snow of the Upper Colorado River Basin: 1. A 6 year record of energy balance, radiation, and dust concentrations. *Water Resources Research*, *48*(7), 1–14. https://doi.org/10.1029/2012WR011985

Patterson, E. M., Gillette, D. A., & Stockton, B. H. (1977). Complex Index of Refraction Between 300 and 700 nm for Saharan Aerosols. *Journal of Geophysical Research*, *82*(2). https://doi.org/http://dx.doi.org/10.1029/JC082i021p03153

Pawlyta, M., & Hercman, H. (2016). Transmission electron microscopy (TEM) as a tool for identification of combustion products: application to black layers in speleothems. *Annales Societatis Geologorum Poloniae*, *86*, 237–248. https://doi.org/http://dx.doi.org/10.14241/asgp.2016.004

Peltoniemi, J. I., Gritsevich, M., Hakala, T., Dagsson-Waldhauserová, P., Arnalds, Anttila, K., Hannula, H. R., Kivekäs, N., Lihavainen, H., Meinander, O., Svensson, J., Virkkula, A., & De Leeuw, G. (2015). Soot on Snow experiment: Bidirectional reflectance factor measurements of contaminated snow. *Cryosphere*, *9*(6), 2323–2337. https://doi.org/10.5194/tc-9-2323-2015

Piontek, D., Hornby, A. J., Voigt, C., Bugliaro, L., & Gasteiger, J. (2021). Determination of complex refractive indices and optical properties of volcanic ashes in the thermal infrared based on generic petrological compositions. *Journal of Volcanology and Geothermal Research*, *411*, 107174. https://doi.org/10.1016/j.jvolgeores.2021.107174

Polyanskiy, M. (2022). Refractive index database [Accessed on 8 October 2022]. https://refractiveindex.info

Posch, M., & Kurz, D. (2007). A2M — A program to compute all possible mineral modes from geochemical analyses. *Computers Geosciences*, *33*, 563–572. https://doi.org/10.1016/j.cageo.2006.08.007

Querry, M. R. (1987). *Optical Constants of Minerals and Other Materials from the Millimeter to the Ultraviolet* (tech. rep.). University of Missouri-Kansas. Kansas City, MO, USA.

Reed, B. E., Peters, D. M., Mcpheat, R., & Grainger, R. G. (2018). The Complex Refractive Index of Volcanic Ash Aerosol Retrieved From Spectral Mass Extinction. *Journal of Geophysical Research: Atmospheres RESEARCH*, *123*, 1339–1350. https://doi.org/10.1002/2017JD027362

Rémy, S., Kipling, Z., Flemming, J., Boucher, O., Nabat, P., Michou, M., Bozzo, A., Ades, M., Huijnen, V., Benedetti, A., Engelen, R., & Peuch, V.-h. (2019). Description and evaluation of the tropospheric aerosol scheme in the European Centre for Medium-Range Weather Forecasts (ECMWF) Integrated Forecasting System (IFS-AER , cycle 45R1). *Geoscientific Model Development*, *12*, 4627–4659. https://doi.org/https://doi.org/10.5194/gmd-12-4627-2019

Réveillet, M., Dumont, M., Gascoin, S., Lafaysse, M., Nabat, P., Ribes, A., Nheili, R., Tuzet, F., Ménégoz, M., Morin, S., Picard, G., & Ginoux, P. (2022). Black carbon and dust alter the response of mountain snow cover under climate change. *Nature Communications*, *13*(1), 1–12. https://doi.org/10.1038/s41467-022-32501-y

Rowe, P. M., Cordero, R. R., Warren, S. G., Stewart, E., Doherty, S. J., Pankow, A., Schrempf, M., Casassa, G., Carrasco, J., Pizarro, J., MacDonell, S., Damiani, A., Lambert, F., Rondanelli, R., Huneeus, N., Fernandoy, F., & Neshyba, S. (2019). Black carbon and other light-absorbing impurities in snow in the Chilean Andes. *Scientific Reports*, *9*(1), 1–16. https://doi.org/10.1038/s41598-019-39312-0

Saffaripour, M., Tay, L.-l., Thomson, K. A., Smallwood, G. J., Brem, B. T., Durdina, L., Johnson, M., Saffaripour, M., Tay, L.-l., Thomson, K. A., & Smallwood, G. J. (2017). Raman spectroscopy and TEM characterization of solid particulate matter emitted from soot generators and aircraft turbine engines. *Aerosol Science and Technology*, *51*(4), 518–531. https://doi.org/10.1080/02786826.2016.1274368

Sanllehi, A. (2023). *Integración y evaluación de modelo de derretimiento y acumulación de nieve y hielo glaciar a modelo hidrológico USM* (Doctoral dissertation). Universidad Técnica Federico Santa María.

Santra, S., Verma, S., Fujita, K., Chakraborty, I., Boucher, O., Takemura, T., Burkhart, J. F., Matt, F., & Sharma, M. (2019). Simulations of black carbon (BC) aerosol impact over Hindu Kush Himalayan sites: Validation, sources, and implications on glacier runoff. *Atmospheric Chemistry and Physics*, *19*(4). https://doi.org/10.5194/acp-19-2441-2019

Scanza, R. A., Mahowald, N., Ghan, S., Zender, C. S., Kok, J. F., Liu, X., Zhang, Y., & Albani, S. (2015). Modeling dust as component minerals in the Community Atmosphere Model: Development of framework and impact on radiative forcing. *Atmospheric Chemistry and Physics*, *15*(1), 537–561. https://doi.org/10.5194/acp-15-537-2015

Schmale, J., Flanner, M., Kang, S., Sprenger, M., Zhang, Q., Guo, J., Li, Y., Schwikowski, M., & Farinotti, D. (2017). Modulation of snow reflectance and snowmelt from Central Asian glaciers by anthropogenic black carbon. *Scientific Reports*, *7*(October 2016), 1–10. https://doi.org/10.1038/srep40501

Schneider, C. A., Rasband, W. S., & Eliceiri, K. W. (2012). NIH Image to ImageJ: 25 years of image analysis. *Nature Methods*, *9*(7), 671–675. https://doi.org/10.1038/nmeth.2089

Schulz, O., & de Jong, C. (2004). Snowmelt and sublimation: Field experiments and modelling in the High Atlas Mountains of Morocco. *Hydrology and Earth System Sciences*, *8*(6), 1076–1089. https://doi.org/10.5194/hess-8-1076-2004

Shaw, T. E., Ulloa, G., Farías-Barahona, D., Fernandez, R., Lattus, J. M., & McPhee, J. (2021). Glacier albedo reduction and drought effects in the extratropical Andes, 1986-2020. *Journal of Glaciology*, *67*(261), 158–169. https://doi.org/10.1017/jog.2020.102

Sihvola, A. (2000). Mixing Rules with Complex Dielectric Coefficients. *Subsurface Sensing Technologies and Applications*, *1*(4), 393–415. https://doi.org/https://doi.org/10.1023/A:1026511515005

Skiles, M., Flanner, M., Cook, J. M., Dumont, M., & Painter, T. H. (2018). Radiative forcing by light-absorbing particles in snow. *Nature Climate Change*, *8*(11), 964–971. https://doi.org/10.1038/s41558-018-0296-5

Skiles, M., Painter, T., & Okin, G. S. (2017). A method to retrieve the spectral complex refractive index and single scattering optical properties of dust deposited in mountain snow. *Journal of Glaciology*, *63*(237), 133–147. https://doi.org/10.1017/jog.2016.126

Skiles, M., & Painter, T. H. (2017). Daily evolution in dust and black carbon content, snow grain size, and snow albedo during snowmelt, Rocky Mountains, Colorado. *Journal of Glaciology*, *63*(237), 118–132. https://doi.org/10.1017/jog.2016.125

Skiles, M., & Painter, T. H. (2019). Toward Understanding Direct Absorption and Grain Size Feedbacks by Dust Radiative Forcing in Snow With Coupled Snow Physical and Radiative Transfer Modeling. *Water Resources Research*, *55*(8), 7362–7378. https://doi.org/10.1029/2018WR024573

Smithsonian. (2022). Report on la palma vulcano [Accessed: 7 October 2022]. https://volcano.si.edu/volcano.cfm?vn=383010

Sokolik, I. N., & Toon, O. B. (1999). Incorporation of mineralogical composition into models of the radiative properties of mineral aerosol from UV to IR wavelengths. *Journal of Geophysical Research*, *104*, 9423–9444.

Sterle, K. M., McConnell, J. R., Dozier, J., Edwards, R., & Flanner, M. G. (2013). Retention and radiative forcing of black carbon in eastern Sierra Nevada snow. *Cryosphere*, *7*(1), 365–374. https://doi.org/10.5194/tc-7-365-2013

Takemura, T., Nakajima, T., Dubovik, O., Holben, B. N., & Kinne, S. (2002). Single-Scattering Albedo and Radiative Forcing of Various Aerosol Species with a Global Three-Dimensional Model. *Journal of Climate*, *15*(4), 333–352. https://doi.org/https://doi.org/10.1175/1520-0442(2002)015<0333:SSAARF>2.0.CO;2

Tarboton, D. G., Chowdhury, T. G., & Jackson, T. H. (1994). A Spatially Distributed Energy Balance Snowmelt Model Proceedings of Symposium on Biogeochemistry of Seasonally Snow. *Reports*, (January), Paper 60.

Tuzet, F., Dumont, M., Lafaysse, M., Picard, G., Arnaud, L., Voisin, D., Lejeune, Y., Charrois, L., Nabat, P., & Morin, S. (2017). A multilayer physically based snowpack model simulating direct and indirect radiative impacts of light-absorbing impurities in snow. *Cryosphere*, *11*(6), 2633–2653. https://doi.org/10.5194/tc-11-2633-2017

Valsaraj, K. T., & Melvin, E. M. (2018). *Principles of environmental thermodynamics and kinetics, fourth edition*. https://doi.org/10.1201/9780429491832

Volz, F. E. (1972). Infrared Absorption by Atmospheric Aerosol Substances. *Journal of Geophysical Research*, *77*(6), 1017–1031. https://doi.org/https://doi.org/10.1029/JC077i006p01017

Warren, S. G., & Wiscombe, W. J. (1980). A model for the spectral albedo of snow. II: snow containing atmospheric aerosols. *Journal of the Atmospheric Sciences*, *37*, 12. https://doi.org/10.1175/1520-0469(1980)037<2734:AMFTSA>2.0.CO;2

Warren, S. G., & Brandt, R. E. (2008). Optical constants of ice from the ultraviolet to the microwave: A revised compilation. *Journal of Geophysical Research Atmospheres*, *113*(14), 1–10. https://doi.org/10.1029/2007JD009744

Webb, M. J., Winter, J. M., Spera, S. A., Jonathan, W., Osterberg, E. C., Webb, M. J., Winter, J. M., Spera, S. A., & Jonathan, W. (2020). Water , agriculture , and climate dynamics in central Chile ' s Aconcagua River Basin ABSTRACT. *Physical Geography*, *00*(00), 1–21. https://doi.org/10.1080/02723646.2020.1790719

Wiscombe, W. J., & Warren, S. G. (1980). A Model for the Spectral Albedo of Snow. I: Pure Snow. *Journal of Atmospheric Sciences*, *37*(12), 2712–2733. https://doi.org/https://doi.org/10.1175/1520-0469(1980)037<2712:AMFTSA>2.0.CO;2

WMO Barcelona Dust Regional Center. (2022). Daily dust products [Accessed on 7 October 2022]. https://dust.aemet.es/products/daily-dust-products

You, J., Tarboton, D. G., & Luce, C. H. (2014). Modeling the snow surface temperature with a one-layer energy balance snowmelt model. *Hydrology and Earth System Sciences*, *18*(12), 5061–5076. https://doi.org/10.5194/hess-18-5061-2014

Zhong, X., Kang, S., Zhang, W., Yang, J., Li, X., Zhang, Y., Liu, Y., & Chen, P. (2019). Light-Absorbing impurities in snow cover across Northern Xinjiang, China. *Journal of Glaciology*, *65*(254), 940–956. https://doi.org/10.1017/jog.2019.69

Zhou, X., Li, S., & Stamnes, K. (2003). Effects of vertical inhomogeneity on snow spectral albedo and its implication for optical remote sensing of snow. *Journal of Geophysical Research: Atmospheres*, *108*(23), 1–15. https://doi.org/10.1029/2003jd003859

Appendix A

Supplementary Information of Chapter 2

A.1 Grain Size

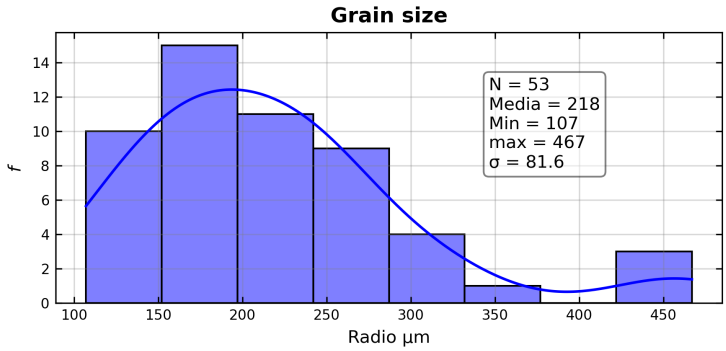

Figure A-1: Grain size distribution.

Examples of grain size photographies:

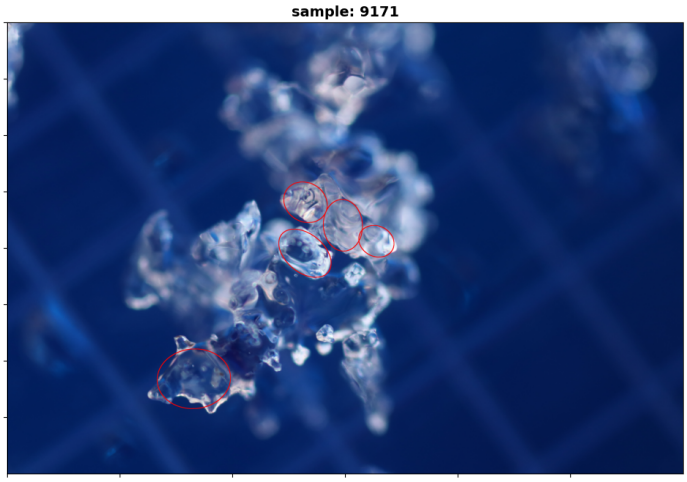

Figure A-2: Grin size sample ID 9171.

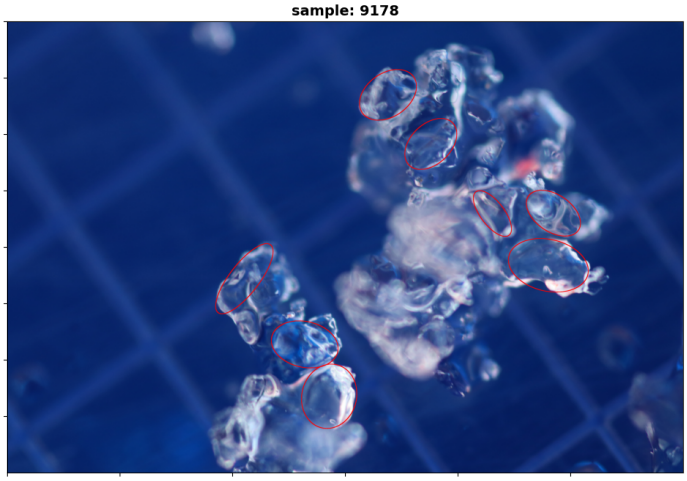

Figure A-3: Grin size sample ID 9178.

A.2 Artificially contaminated plots

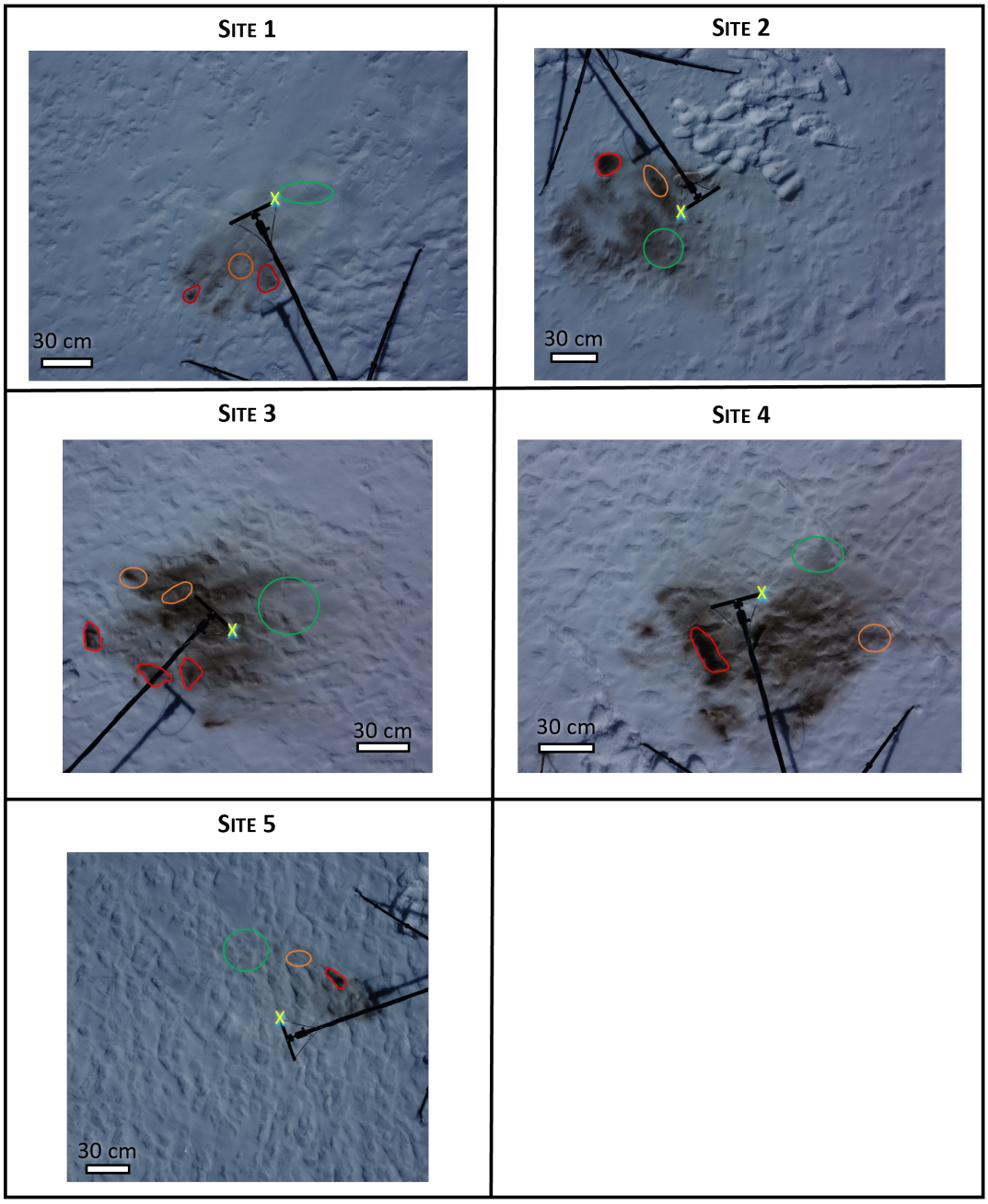

Figure A-4: Aerial photography of artificially contaminated plots, captured with Marvin Mini 2 drone. For each site snow sample areas are shown as: red for Sample A; orange for sample B; and green for sample C. "X" indicates the radiance sensor axis.

Table A.2: MD Mineralogical composition of additional soil samples. X-Ray Diffraction analysis results. f_m indicates the mass fraction, while f_v indicates the normalized volumetric fraction

Sample	Feldspar (Plagioclase + Alkali) f_m / f_v	Quartz f_m / f_v	Illite f_m / f_v	Hematites f_m / f_v	Amphibole f_m / f_v	Chlorites f_m / f_v
1	0.573 / 0.623	0.265 / 0.278	0.075 / 0.076	0.045 / 0.024	0.036 / -	0.007 / -
2	0.536 / 0.560	0.389 / 0.391	0.042 / 0.041	0.017 / 0.009	0.010 / -	0.006 / -
3	0.617 / 0.669	0.250 / 0.261	0.070 / 0.070	0.000 / 0.000	0.055 / -	0.009 / -
4	0.398 / 0.443	0.435 / 0.466	0.038 / 0.040	0.095 / 0.051	0.025 / -	0.010 / -
5	0.781 / 0.812	0.165 / 0.165	0.019 / 0.018	0.010 / 0.005	0.021 / -	0.005 / -
6	0.749 / 0.784	0.168 / 0.169	0.035 / 0.034	0.026 / 0.013	0.010 / -	0.012 / -
7	0.618 / 0.638	0.325 / 0.323	0.032 / 0.031	0.016 / 0.008	0.000 / -	0.009 / -
8	0.646 / 0.694	0.247 / 0.256	0.040 / 0.040	0.020 / 0.010	0.041 / -	0.006 / -
9	0.722 / 0.739	0.250 / 0.247	0.012 / 0.012	0.006 / 0.003	0.008 / -	0.002 / -

A.3 XRD and Elemental analysis

Table A.1: Elemental analysis.

	%
Si	26.02
O	42.10
Al	9.51
Fe	9.14
Mg	2.15
Na	2.68
K	2.39
H	-
Ca	2.88
Ti	0.87
Mn	0.46
Cr	-
Ni	-
Zn	-
Cu	-
C	1.80
Pb	-
S	0.00
P	0.00
Zr	0.00
Mo	0.00
In	0.00

A.4 Equivalent dust concentration

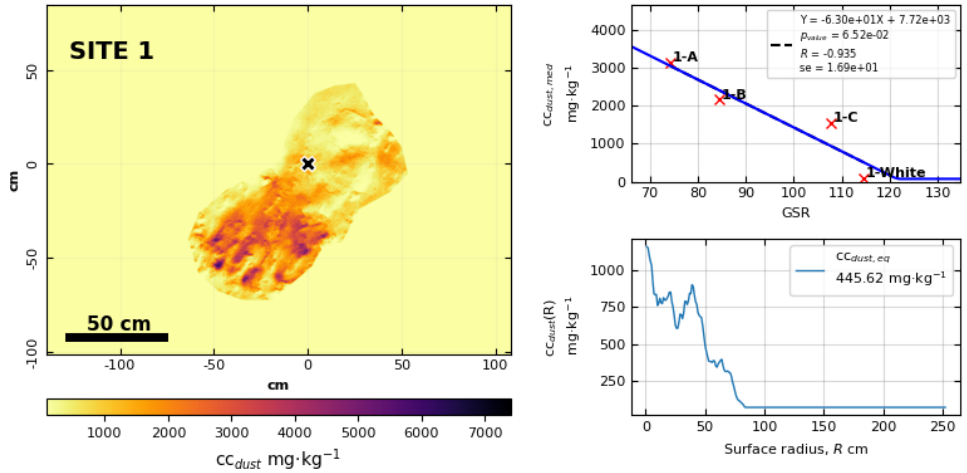

Figure A-5: Equivalent dust concentration in mg $\cdot$ kg^{-1} at site 1. (Left) Spatial extrapolation; (right-top) Grayscale and dust concentration linear regression; and, (left-bottom) dust concentration as a function of the surface radius (R).

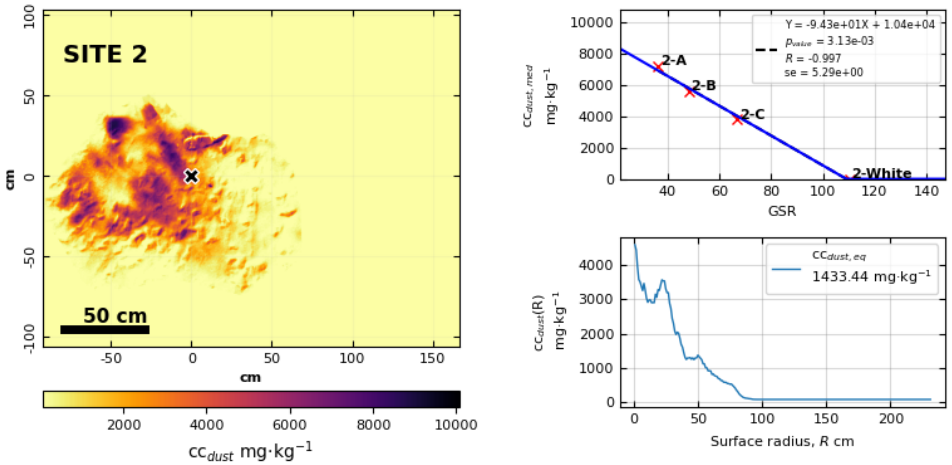

Figure A-6: Equivalent dust concentration in mg $\cdot$ kg^{-1} at site 2. (Left) Spatial extrapolation; (right-top) Grayscale and dust concentration linear regression; and, (left-bottom) dust concentration as a function of the surface radius (R).

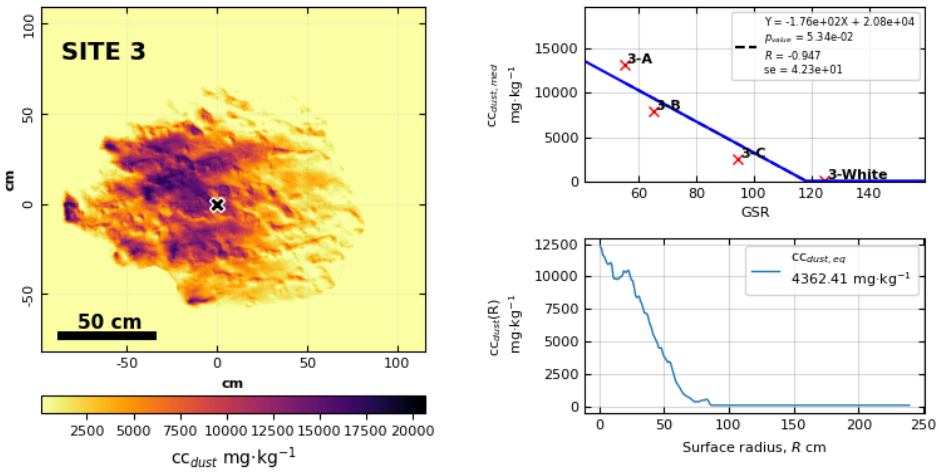

Figure A-7: Equivalent dust concentration in $\text{mg} \cdot \text{kg}^{-1}$ at site 3. (Left) Spatial extrapolation; (right-top) Grayscale and dust concentration linear regression; and, (left-bottom) dust concentration as a function of the surface radius (R).

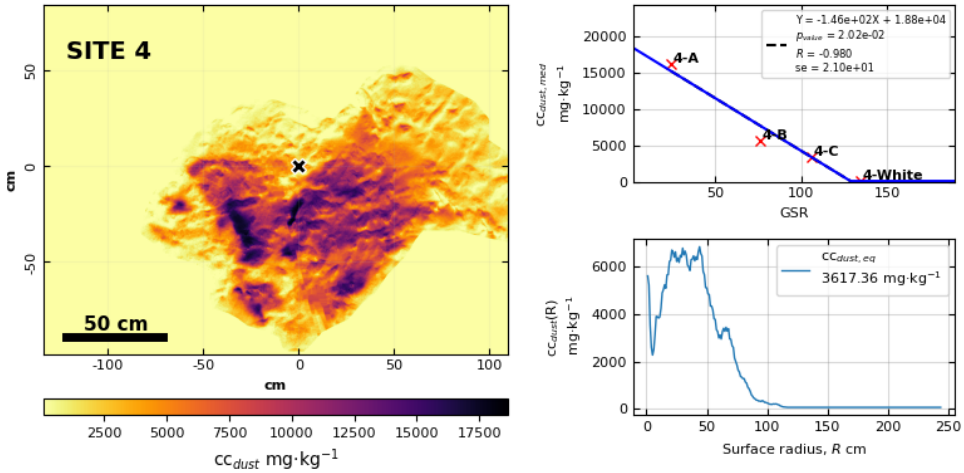

Figure A-8: Equivalent dust concentration in $\text{mg} \cdot \text{kg}^{-1}$ at site 4. (Left) Spatial extrapolation; (right-top) Grayscale and dust concentration linear regression; and, (left-bottom) dust concentration as a function of the surface radius (R).

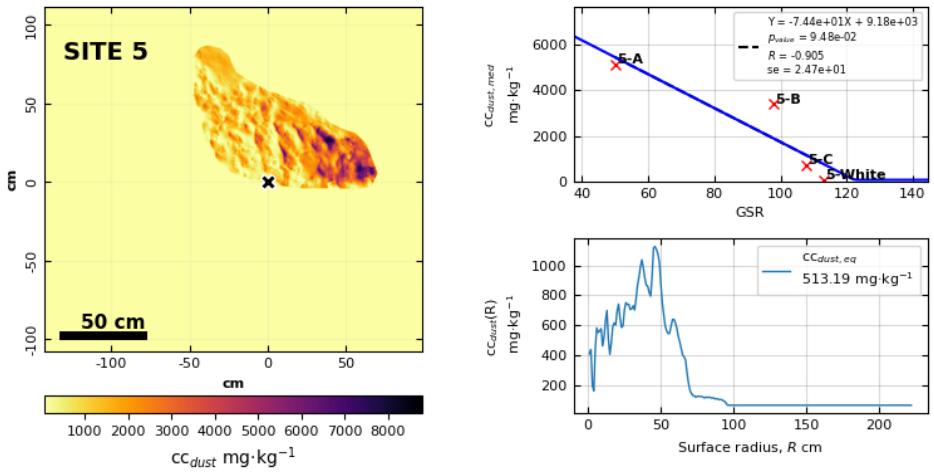

Figure A-9: Equivalent dust concentration in $\text{mg} \cdot \text{kg}^{-1}$ at site 5. (Left) Spatial extrapolation; (right-top) Grayscale and dust concentration linear regression; and, (left-bottom) dust concentration as a function of the surface radius (R).

Appendix B

Supplementary Information of Chapter 3

Table B.1: Fixed UEB snow model parameters.

Parameter	Description	Value	unit
K_{sat}	Saturated hydraulic conductivity	200	$\mathrm{m \cdot hr^{-1}}$
C_w	Water heat capacity	4.18	$\mathrm{kJ \cdot kg^{-1} \cdot^o C^{-1}}$
ρ_w	Water density	1000	$\mathrm{kg \cdot m^{-3}}$
C_g	Ground heat capacity	2.09	$\mathrm{kJ \cdot kg^{-1} \cdot^o C^{-1}}$
ρ_g	Density of soil layer	1700	$\mathrm{kg \cdot m^{-3}}$
C_s	Snow heat capacity	2.09	$\mathrm{kJ \cdot kg^{-1} \cdot^o C^{-1}}$
ϵ_s	Emissivity of snow	0.99	-
L_c	Capillary retention fraction	0.02	-
T_r	Temperature above which precipitation is rain	3	^{o}C
T_s	Temperature below which precipitation is snow	-1	^{o}C
z	Wind/air temperature measurement height	1.5	m
D_e	Soil effective depth	0.1	-
$\alpha_b g$	Bare ground albedo	0.1	-

Table B.2: Calibrated UEB snow model parameters.

Parameter	Description	unit	Calibration range	Optimal range	Optimal value
K_s	Surface Conductance	$\mathrm{m \cdot hr^{-1}}$	0.01 - 0.2	0.044 - 0.067	0.051
z_o	Surface aerodynamic roughness	m	0.0001 - 0.1	0.0003 - 0.0063	0.0019
ρ_{snow}	Snow density	$\mathrm{kg \cdot m^{-3}}$	100 - 500	341.8 - 447.4	422.2
F_{MO}	Precipitation scaling factor	-	1 - 3	1.45 - 2.32	1.65
$D_{BC,dry}$	dry BC deposition rate	$\mathrm{g \cdot m^{-2} \cdot s^{-1}}$	$1x10^{-12}$ - $1x10^{-9}$	2.7e-10 - 9.9e-10	7.7e-10
$D_{MD,dry}$	dry MD deposition rate	$\mathrm{g \cdot m^{-2} \cdot s^{-1}}$	$1x10^{-10}$ - $1x10^{-8}$	2.6e-09 - 9.1e-09	5.7e-09
$D_{BC,wet}$	wet BC deposition rate	$\mathrm{g \cdot m^{-2} \cdot s^{-1}}$	$1x10^{-9}$		
$D_{MD,wet}$	wet MD deposition rate	$\mathrm{g \cdot m^{-2} \cdot s^{-1}}$	$1x10^{-8}$		

Table B.3: Grain size increasing rates in $\mu\text{m} \cdot \text{day}^{-1}$ depending on the snow temperature and snow depth.

h_{snow} cm	T_{msnow} < 0 °C	0 °C
0 - 4	19	27
4 - 10	27	17
> 10	1	10

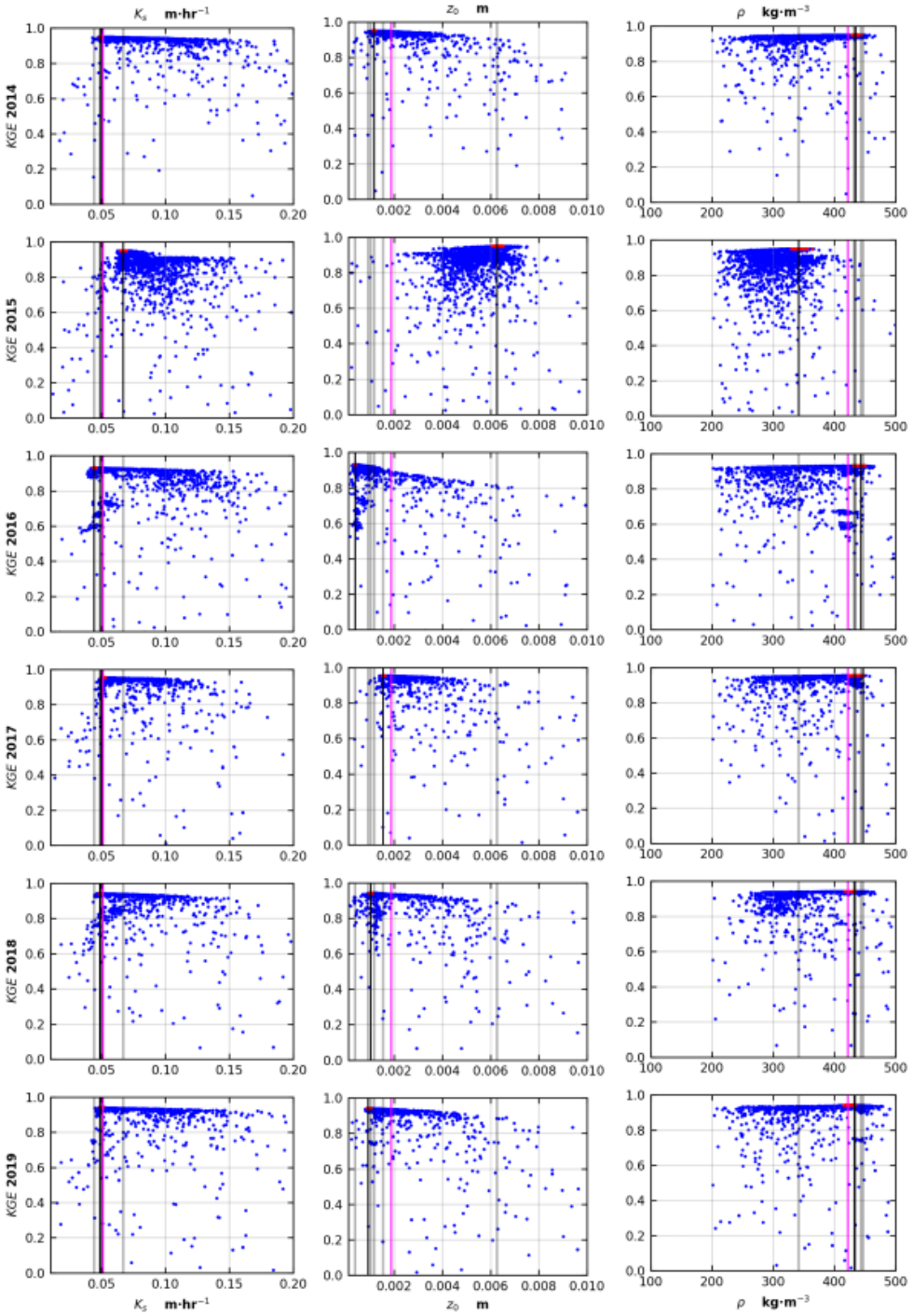

Figure B-1: Scatter plot showing the model performance (KGE) model performance depending on the surface Conductance (K_s), surface aerodynamic roughness (z_o), and snow density (ρ_{snow}). Red dots show the performance of the 10% of simulations with best behavior, and blue dots show the rest of the simulations. Vertical lines show, in gray all the optimal parameter for each cross-validation, in black the optimal parameter of the particular cross-validation, and in magenta the average of all the optimal parameters from each cross-validation.

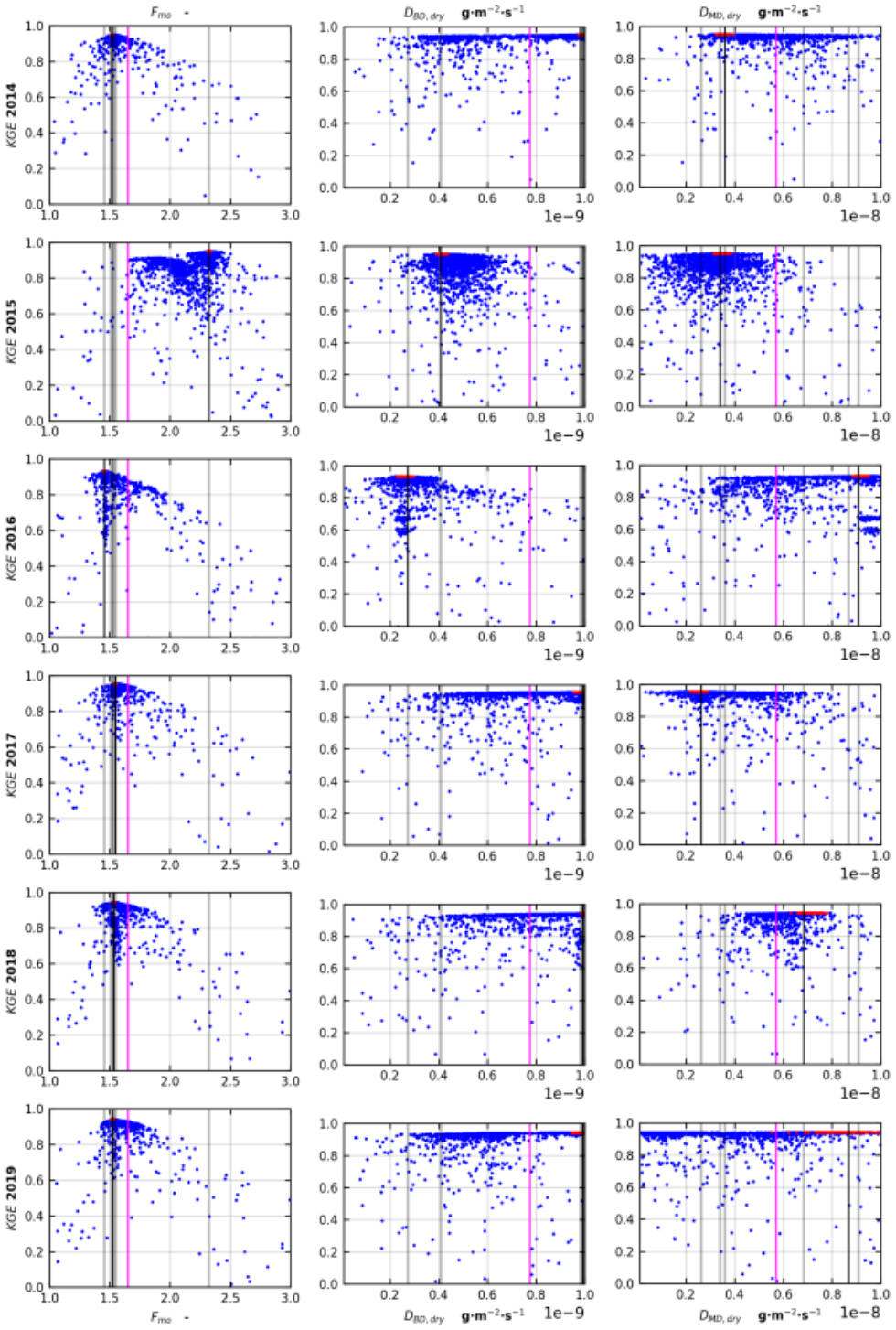

Figure B-2: Scatter plot showing the model performance (KGE) model performance depending on the precipitation scaling factor (F_{MO}), dry BC deposition rate ($D_{BC,dry}$), and dry MD deposition rat ($D_{MD,dry}$). Red dots show the performance of the 10% of simulations with best behavior, and blue dots show the rest of the simulations. Vertical lines show, in gray all the optimal parameter for each cross-validation, in black the optimal parameter of the particular cross-validation, and in magenta the average of all the optimal parameters from each cross-validation.

Table B.4: Yearly snowpack duration (SD) shortening in days depending on the deposition rate.

year	case 2 D_{MD}x0.5-D_{BC}x0.5	case 3 D_{MD}x1-D_{BC}x1	case 4 D_{MD}x2-D_{BC}x2	case 5 D_{MD}x3-D_{BC}x3
2014	0	0	5	5
2015	0	0	3	5
2016	0	1	1	16
2017	1	3	4	6
2018	2	3	5	5
2019	1	1	13	13

Table B.5: Yearly-average of daily albedo reduction depending on the deposition rate.

year	case 2 D_{MD}x0.5-D_{BC}x0.5	case 3 D_{MD}x1-D_{BC}x1	case 4 D_{MD}x2-D_{BC}x2	case 5 D_{MD}x3-D_{BC}x3
2014	0.007	0.014	0.026	0.038
2015	0.006	0.012	0.022	0.035
2016	0.006	0.013	0.028	0.039
2017	0.013	0.023	0.039	0.060
2018	0.005	0.011	0.021	0.030
2019	0.008	0.014	0.030	0.041

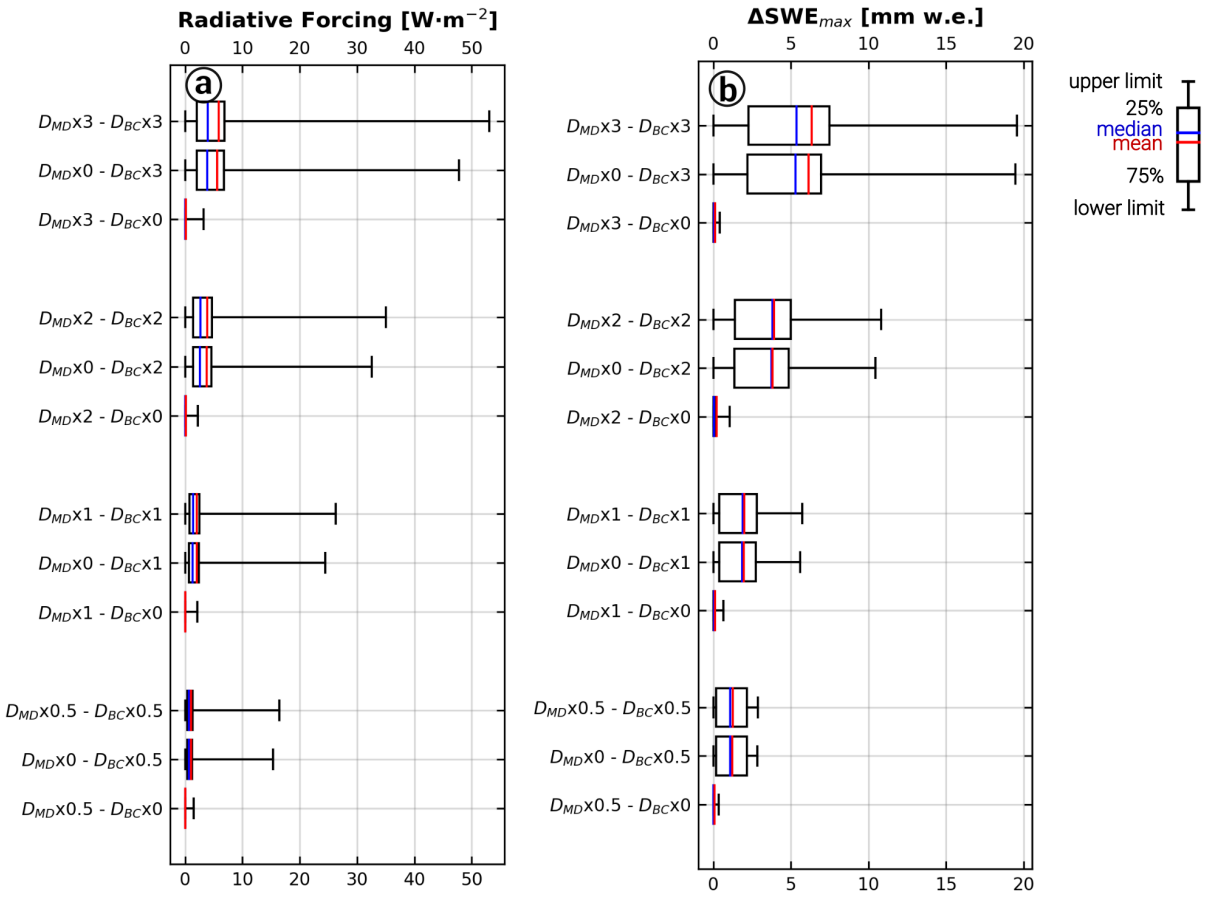

Figure B-3: (a) Daily mean RF and ΔSWE_{max} onto snow surface according to the deposition rate.

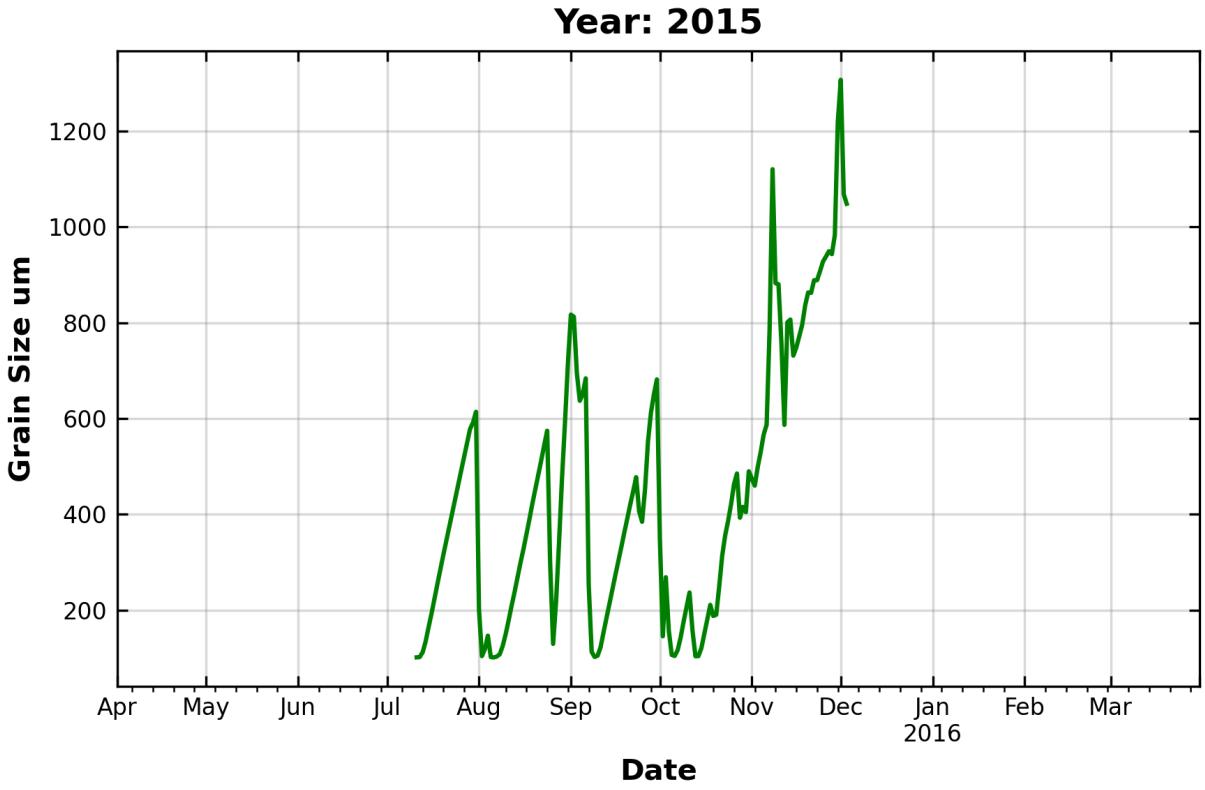

Figure B-4: Time series of simulated grain size considering optimal parameters.